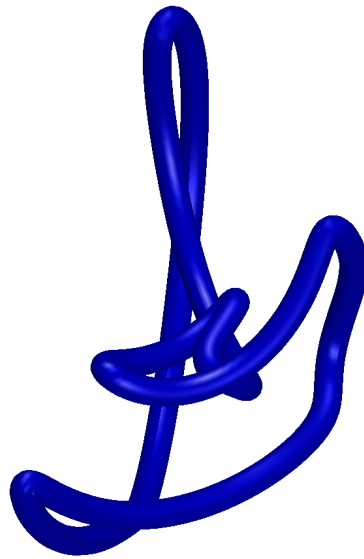


# Quantum Information Processing in Rare-Earth-Ion Doped Crystals



Janus Halleløv Wesenberg

QUANTOP  
Department of Physics and Astronomy  
University of Aarhus, Denmark

Ph.D. Thesis  
July 2004

This thesis is submitted to the Faculty of Science at the University of Aarhus, Denmark, in order to fulfill the requirements for obtaining the Ph.D. degree in Physics.

The studies have been carried out under the supervision of Prof. Klaus Mølmer at the Department of Physics and Astronomy, University of Aarhus, from January 2001 to July 2004.

Electronic versions of this thesis and associated code will be available at <http://www.halwe.dk/janus/research/> for as long as possible.

# Contents

<b>List of Publications</b>	<b>vii</b>
<b>Preface</b>	<b>ix</b>
<b>Abstract</b>	<b>xi</b>
<b>1 Introduction to the Thesis</b>	<b>1</b>
1.1 Outline of the Thesis . . . . .	1
<b>2 Introduction to Quantum Computing</b>	<b>3</b>
2.1 Bits and Qubits . . . . .	3
2.1.1 Entanglement . . . . .	4
2.2 Quantum Circuits . . . . .	4
2.2.1 Universal Gates . . . . .	5
2.2.2 Reading Quantum Circuit Diagrams . . . . .	6
2.3 Quantum Algorithms . . . . .	6
2.3.1 Grover's Search Algorithm . . . . .	7
2.3.2 Shor's Factoring Algorithm . . . . .	9
2.4 Building a Quantum Computer . . . . .	9
2.4.1 Quantum Error Correction . . . . .	9
2.4.2 The DiVincenzo Criteria . . . . .	10
2.5 Summary . . . . .	11
<b>3 Rare-Earth-Ion-Doped Inorganic Crystals</b>	<b>13</b>
3.1 Chemical Properties . . . . .	14
3.2 Optical Properties . . . . .	15
3.2.1 Typical Level Structure . . . . .	15
3.2.2 Hyperfine Structure . . . . .	17
3.2.3 Inhomogeneous Broadening . . . . .	18
3.3 Ion Interactions . . . . .	18
3.3.1 Rare-Earth-Ion Dipole Moments . . . . .	18
3.3.2 Dipole Interaction . . . . .	19
3.3.3 Model Interaction Hamiltonian . . . . .	20
3.4 Summary . . . . .	21

<b>4</b>	<b>Introduction to REQC</b>	<b>23</b>
4.1	Digging Channels . . . . .	24
4.2	Initialization . . . . .	26
4.2.1	Bus Architecture . . . . .	28
4.3	A CNOT-Gate . . . . .	29
4.4	Read-Out and Ensemble Algorithms . . . . .	30
4.4.1	Quantum Database Search . . . . .	30
4.4.2	Other Quantum Algorithms . . . . .	34
4.5	Other Proposals . . . . .	34
4.6	Summary . . . . .	34
<b>5</b>	<b>Single Qubit Gates</b>	<b>37</b>
5.1	Ion-Field Interaction . . . . .	37
5.1.1	Single Field Evolution . . . . .	38
5.2	Population Swapping . . . . .	39
5.2.1	Single Pulse . . . . .	39
5.2.2	Composite Pulses . . . . .	40
5.2.3	Smooth Fields . . . . .	41
5.3	Coherent Operations . . . . .	43
5.3.1	Sequential Pulses . . . . .	43
5.3.2	Parallel Fields . . . . .	44
5.4	Phase Shift Operations . . . . .	45
5.4.1	Phase Shift by Population Swapping . . . . .	46
5.4.2	Phase Compensating Pulses . . . . .	46
5.4.3	Direct Phase Shift Operations . . . . .	48
5.4.4	Other Gate Implementations . . . . .	49
5.5	Summary . . . . .	50
<b>6</b>	<b>Automated Design of Robust Gate Implementations</b>	<b>51</b>
6.1	Introduction to Optimal Control Theory . . . . .	52
6.1.1	The Objective Functional . . . . .	52
6.1.2	Optimal Control Software . . . . .	53
6.1.3	Optimal Control as a Constrained Optimization Problem . . . . .	53
6.1.4	Overview of the Chapter. . . . .	54
6.2	Calculating the Objective Gradient . . . . .	54
6.2.1	Real State Vector . . . . .	54
6.2.2	Complex State Vector . . . . .	55
6.3	Direct Minimization Methods . . . . .	57
6.4	Application to Single State Quantum Dynamics . . . . .	57
6.4.1	Control Parametrization for Quantum Optics . . . . .	58
6.4.2	Optimized Adjoint State Boundary Condition . . . . .	59
6.5	Application to Multi State Quantum Dynamics . . . . .	60
6.5.1	Fidelity of Quantum Evolution . . . . .	61
6.6	Summary . . . . .	63

<b>7</b>	<b>Optimized Gate Implementations for REQC</b>	<b>65</b>
7.1	Numerical Implementation . . . . .	66
7.1.1	State Propagation . . . . .	66
7.1.2	Minimax Algorithm . . . . .	67
7.1.3	Performance . . . . .	68
7.2	Examples of Optimized Pulses . . . . .	69
7.2.1	Time Based Field Parametrization . . . . .	69
7.2.2	Fourier Based Field Parametrization . . . . .	71
7.3	Approximate Evolution of Off-Resonant Ions . . . . .	72
7.3.1	Dyson Expansion . . . . .	73
7.3.2	Magnus Expansion . . . . .	74
7.4	Conclusions . . . . .	75
<b>8</b>	<b>Two-Qubit Gate Operations</b>	<b>77</b>
8.1	Dipole Blockade Gates . . . . .	78
8.1.1	A Simple Controlled-Phase Gate . . . . .	79
8.1.2	Twelve-Pulse Phase-Compensated Gate . . . . .	80
8.1.3	Seven-Pulse Phase-Compensated Gate . . . . .	81
8.2	The Comb Gate . . . . .	84
8.2.1	Adaptation of the Comb Gate for the REQC-System . . . . .	86
8.3	Entangling Power . . . . .	86
8.3.1	General Theory . . . . .	87
8.3.2	Entangling Power of the Dipole Coupling . . . . .	88
8.4	Conclusion . . . . .	89
8.4.1	Comparison of Multi Qubit Gates . . . . .	89
8.4.2	Prolonged Excitation of the Control Qubit . . . . .	90
8.4.3	Implementability . . . . .	90
<b>9</b>	<b>Statistical Properties of the Dipole Coupling</b>	<b>91</b>
9.1	A Spherical Distribution of Dipoles . . . . .	92
9.1.1	One Dipole in a Sphere . . . . .	92
9.1.2	Two Important Examples . . . . .	94
9.1.3	Multiple Dipoles in a Sphere . . . . .	95
9.1.4	The Limit of $N \rightarrow \infty$ . . . . .	96
9.2	Local Field Theory . . . . .	98
9.3	An Excluded Volume . . . . .	99
9.3.1	An Alternative Derivation of $P_\infty(\epsilon, g)$ . . . . .	101
9.4	Summary and Discussion . . . . .	102
9.4.1	Implications for REQC . . . . .	104
<b>10</b>	<b>Meeting the DiVincenzo Criteria</b>	<b>107</b>
10.1	Scalability . . . . .	107
10.1.1	Available Channels . . . . .	107
10.1.2	Available Instances . . . . .	108
10.1.3	Asymmetrical Bus . . . . .	108

10.1.4 Structured Doping . . . . .	109
10.2 Initialization . . . . .	110
10.3 Long Qubit Decoherence Time . . . . .	111
10.4 Universal Gates . . . . .	111
10.5 Read Out . . . . .	112
<b>11 Summary and Outlook</b>	<b>113</b>

# List of Publications

- I. Janus Wesenberg and Klaus Mølmer. *Mixed collective states of many spins*. Phys. Rev. A **6**, 062304 (2002).
- II. Janus Wesenberg and Klaus Mølmer. *Robust quantum gates and a bus architecture for quantum computing with rare-earth-ion doped crystals*. Phys. Rev. A **68**, 012320 (2003).
- III. Janus Halleløv Wesenberg. *Designing robust gate implementations for quantum information processing*. Phys. Rev. A **69**, 042323 (2004).
- IV. Janus Halleløv Wesenberg and Klaus Mølmer. *The field inside a random distribution of parallel dipoles*. Phys. Rev. Lett. **93**, 143903 (2004).



# Preface

This thesis presents the work I have done under the supervision of Prof. Klaus Mølmer since joining the Rare Earth Quantum Computing project in the beginning of 2002.

During this period I have had the privilege of working in many different areas, from numerical implementation of optimal control theory over quantum gate alchemy and statistical physics to quantum information theory.

## Acknowledgments

First of all, I would like to thank my supervisor Klaus Mølmer. Although sometimes frustrating, it has been a luxury to always have someone to turn to who could catch up with your last two weeks of work in a matter of minutes, and then offer a number of insights of the deeper meaning of the results before giving excellent advice on how it would be wise to proceed.

The members of the group of Prof. Stefan Kröll, who constitute the Swedish part of the REQC (and later ESQUIRE) networks, have also been very close collaborators. In particular I am grateful for their unending patience in explaining the workings of rare-earth-ion doped crystals to a poor theoretician.

I would also like to thank the group of Prof. Gerard Milburn at the Centre for Quantum Computer Technology at the University of Queensland, Australia, for their hospitality during my visit to their group in the first half of 2003.

My friends and colleagues at the University of Aarhus have made the almost eight years I have spend here thoroughly enjoyable. I would like to thank each one of you personally, but will resist the urge for fear of running out of paper or accidentally forgetting someone.

Finally, my warmest thanks go to my friends and family outside the yellow brick world for being patient with me when I have devoted too much time to physics. In particular, I would like to thank my wife Sara for her love and support.

Janus Halleløv Wesenberg  
July, 2004



# Abstract

**Dansk resumé.** Denne afhandling beskæftiger sig med en foreslået kvante-computer baseret på optisk aktive urenheder i krystaller. Kvantecomputeren var for 20 år siden kun en teoretisk kuriositet, men er i dag godt på vej til at blive virkelighed. Denne udvikling tog for alvor fart da det i slutningen af 1980'erne blev klart at kvantecomputere ville kunne løse opgaver der i praksis er umulige på klassiske computere, såsom at bryde visse koder. Afhandlingen beskriver løsninger til en række centrale problemer i forbindelse med den foreslåede kvantecomputer, og fjerner dermed de fleste fundamentale forhindringer i forhold til at bygge den. Specielt udvikles en række metoder til at implementere logiske operationer på en måde der ikke påvirkes af støj.

Since the discovery of the threshold theorem of quantum computing, which asserts that quantum computing is possible even with imperfect implementations, the successful operation of a scalable quantum computer seems entirely feasible. Quantum computers are able to solve a large class of problems, known as hidden subgroup problems, exponentially faster than the best known classical algorithms. The hidden subgroup problems include the factoring of large integers, a problem of great interest in cryptography.

The thesis work has focused on various aspects of rare earth quantum computing (REQC), a proposal for an ensemble quantum computer based on rare-earth ions embedded in cryogenic inorganic crystals. The central idea of the REQC proposal is to use ground state hyperfine levels of the dopant ions for quantum registers. These levels have decoherence times of several tens of milliseconds and lifetimes of hours, making them suitable for storage of quantum information. The ions can be manipulated by coherent optical fields, and interact through the dipole coupling between static dipole moments induced by the anisotropy of the host crystal. As the strength of the dipole interaction, as well as several other parameters, vary between dipole pairs, robust gate operations, *i.e.* gate operations that perform well for a range of parameters, are a central requirement of the REQC proposal. The design of such robust gate operations is a central theme of the thesis. Another central theme is the scaling properties of the REQC proposal: as the proposal relies on dopant ions by chance being placed close enough that their dipole interaction allow gate operations, the scaling properties are highly sensitive to the requirements put on interaction strength by the gate operations.

With respect to gate design, we have developed a method of phase compensating pulses that makes it possible to implement any one-qubit gate operation in terms of sequential population swapping operations applied in parallel to multiple optical transitions. This is useful, since several robust population swapping operations are known. In addition, we have shown that by means of phase compensating operations, sequential population swapping operations can be used to implement a robust two-qubit gate operation, thus extending the set of one-qubit gate operations to a universal set of quantum gate operations.

The phase compensation scheme leads to prolonged excitations of the excited states of the ions with an associated risk of decay. To avoid this problem, we have implemented a numerical method for optimizing gate implementations by means of a sample-based description of the performance of a given implementation. This numerical method is capable of producing highly robust high-performance gate operations of relatively short duration. It appears, however, that the sample-based optimization is not well suited to ensure that far detuned spectator ions are not disturbed. We propose several potential solutions to this problem.

As a more general result of the work on gate operations for the REQC system, we have derived a general bound on the entangling power of any qubit interaction. In the case of the REQC system, this bound implies that any powerful two-qubit gate requires the excitation of an ion for a time inversely proportional to the coupling strength, thus establishing a relation between excited state life-time, coupling strength requirements, and obtainable gate error rate.

The scaling properties of the REQC proposal are hampered by the fact that it relies on ions by chance being within interaction distance. We have described an asymmetrical bus architecture that could potentially remedy this shortcoming, but no physical system for implementing this architecture has yet been found.

In the course of studying the statistics of the dipole coupling in the REQC system, we have discovered a shift of the Lorentzian probability distribution describing the electric field at the center of a spherical distribution of parallel dipoles. This shift, which appears to be previously unnoticed, could have implications for a range of models describing dipole fields in terms of a mean field approximation.

In total, the thesis work has established a number of key results necessary for the successful operation of an REQC system, so that there are today no fundamental obstacles for implementing small scale quantum computing in the REQC system.

# CHAPTER 1

## Introduction to the Thesis

The guiding theme of this thesis is the REQC proposal for quantum computing in rare-earth-ion doped crystals. This proposal has been investigated under the REQC and ESQUIRE projects as a part of the IST-FET programme of the European Union by a broad European network, of which the Århus branch has been the only purely theoretical group.

While we<sup>1</sup> have investigated many areas of the REQC proposal, our focus has been on the design of robust gate operations for the system, as should be clear from the outline given below. In the interest of making this thesis useful for the REQC network, we will, nevertheless, make some efforts toward presenting a coherent picture of the complete REQC system.

### 1.1 Outline of the Thesis

The structure of the thesis is perhaps most easily described by considering the questions we try to answer in each chapter:

**What is a quantum computer – and why would you want to build one?** As we will see in chapter 2, a quantum computer is a system capable of doing computations on quantum bits. Since quantum bits are very different from classical bits, this allows us to do some calculations, such as breaking codes, that seem to be virtually impossible on classical computers.

**So, what are these crystals you want to use?** It is actually not as much the crystal as the dopant rare-earth ions that interest us. In chapter 3 we will see that these ions behave much like a frozen gas which we can manipulate via laser fields. Furthermore, the ions have a controllable interaction via static dipole moments induced by the crystal.

**How would you build a quantum computer from that?** First of all, we can address subsets of the ions by the inhomogeneous shift of an optical transition. As the ions of these frequency channels are interspersed throughout the crystal,

---

<sup>1</sup> In this thesis “we” will sometimes refer to the reader and author and sometimes to the author and co-workers. This will always be suitable, as per the traditions of written physics.

the key idea of the REQC proposal is that by applying a clever initialization procedure, we can deactivate all ion that are not part of an independent quantum computer. In this way, we obtain an ensemble of independent quantum computers, operating in parallel, spread out over the crystal.

**Can you even design a decent one-qubit gate for this system?** As we will see in chapter 5, it is actually possible to perform single-qubit gate operations in a way that all the different quantum computers end up doing the same thing. The methods for making such robust gate implementations have been used for many years, for example in relation to MR scanners, but they include a lot of heuristics, and they are not well suited for designing smooth fields which we would prefer to use.

**Would it not be possible to leave the gate design to a computer?** Certainly. This has also been done in the MR community for a number of years. In chapter 6 we describe a numerical method suitable for deriving gate implementations that perform well for all the independent quantum computers in a crystal.

**Does the numerical approach work?** Yes, it does. Although the performance of the optimized gate implementations outperform the “manually designed” implementations in some respects, we will see in chapter 7 that there is still room for improvements.

**What about two-qubit gates then?** By various tricks, it is actually possible to construct two qubit gates from one-qubit gates using the interaction between the static dipole moments induced in the ions by the field of the host crystal. One of the more general results of the thesis, which we will prove in chapter 9, is that in order to perform such a gate operation, we must necessarily populate a decay-prone excited state of the ions for an extended period. This of course imposes a fundamental limitation on the performance of the system.

**You need strongly interacting ions. How many of those do you expect to find in a crystal?** The answer to this question, as presented in chapter 8, turned out to be so interesting that we consider a number of implications not strictly related to REQC. From the point of view of REQC, the answer is simple: too few.

**So, is REQC feasible?** Yes and no. In chapter 10 we compare the properties of the REQC system with DiVincenzo’s checklist for quantum computing, and find that the only strictly critical aspect is the scaling properties which are hampered by the fact that there are so few strongly interacting ions in a crystal. There are several proposals for how this problem could be remedied, but none of these have yet been studied in detail.

## CHAPTER 2

# Introduction to Quantum Computing

Until Benioff [1], Feynman [2], and Peres [3] in the early 1980's arrived at the subject from very different directions, no comprehensive study of the computational capabilities of quantum systems had been performed. Today, just 20 years later, after the discovery of powerful quantum algorithms [4–6] and the realization that error correction can be applied to quantum information processing [7, 8], quantum computing is close to becoming reality: small scale quantum computing has been experimentally demonstrated [9–11], and the construction of large scale quantum computing systems seems only to be a question of “when” and “how”.

The aim of this chapter is to give a brief introduction to the central concepts of quantum computing. We will assume some knowledge of quantum theory. For an introduction to quantum computing that make no such assumptions, we refer to the very comprehensive book by Nielsen and Chuang [12], which should also be accessible to the non-physicist, or the excellent lecture notes by John Preskill [13] which are available on the Internet.

### 2.1 Bits and Qubits

A *bit* is the fundamental unit of information in classical information theory. In a system for processing classical information, a bit is physically stored in a one bit *register*: part of the system with two clearly distinguishable states, traditionally labeled 0 and 1, such as a switch being in the on or off position, or the potential difference across a capacitor being 0 or 5 V.

In contrast, a quantum bit, or *qubit*, is what information can be stored in a register with two *quantum* states  $|0\rangle$  and  $|1\rangle$ . The difference between a quantum register and the classical counterpart is that the quantum register can exist in *superposition* states, such as  $|\psi\rangle = c_0|0\rangle + c_1|1\rangle$  that have no classical counterparts. By the most pragmatic interpretation of quantum mechanics, measuring

the state of a quantum register initially in state  $|\psi\rangle$ , will give the answer 0 with probability  $|c_0|^2$  and 1 with probability  $|c_1|^2$ , assuming  $|c_0|^2 + |c_1|^2 = 1$ , after which the state of the register *collapses* to a state  $|\psi'\rangle$  consistent with the measurement.

By combining  $n$  classical one bit registers, we obtain a register with  $2^n$  distinct states, which we will label by considering the constituent bits to be *Binary digits*: If  $x_i$  is the state of the  $i$ .th one bit register, we label the combined register state by the number

$$x = \sum_{i=1}^n x_i 2^i. \quad (2.1)$$

Similarly, we use  $|x\rangle$  to refer to the state

$$|x\rangle = |x_1\rangle_1 |x_2\rangle_2 \dots |x_n\rangle_n, \quad (2.2)$$

of the  $n$  qubit quantum register.

### 2.1.1 Entanglement

Already at this point, where we have only considered registers, quantum effects begin to be visible: Consider for instance the case of two qubits, initially both in the state  $(|0\rangle + |1\rangle)/\sqrt{2}$ . Measuring the state of any of the qubits will yield  $|0\rangle$  or  $|1\rangle$  with equal probability. The collapse of the state ensures that subsequent measurements will agree with the first.

If we now combine the two qubits to form a two qubit quantum register in the state  $|\Psi_-\rangle = (|0\rangle|1\rangle - |1\rangle|0\rangle)/\sqrt{2}$ , things at first look similar: if we measure the state of any of the qubits, we obtain  $|0\rangle$  or  $|1\rangle$  with equal probability, and subsequent measurements are consistent with the first. The difference appears when we measure one qubit after the other: In this case, we find that the two measurements are always opposite. This *entanglement* of the two qubits described by the initial state, is emerging as a physical resource on line with classical information, and has been the center of much attention over recent years.

## 2.2 Quantum Circuits

Quantum computing must necessarily involve some manipulation of the quantum registers. As a model for this manipulation, we again turn to classical computing. A classical logical circuit maps particular values  $x$  of an input register to particular values  $y = f(x)$  of an output register.

The classical logical circuit does not immediately generalize to quantum systems, since the reversibility of quantum dynamics require us to consider only 1:1 mappings. It turns out, that this is no restriction: Any classical circuit  $f$  can be extended to a reversible circuit. If  $f$  is a classical circuit mapping  $n$  bits to  $m$  bits, we can construct a reversible circuit  $f_r$ , operating on  $n + m$  bits by letting  $f_r(x, y) = (x, y \oplus f(x))$ , where  $\oplus$  is the exclusive or, *i.e.* bitwise addition

modulo 1. We will denote the corresponding unitary operation by  $U_f$ , so that  $U_f |x\rangle |y\rangle = |x\rangle |y \oplus f(x)\rangle$  (Fig. 2.1). Since  $(a \oplus b) \oplus b = a$  for any  $a, b$ , we see that  $U_f^2 = \mathbf{1}$ , so that  $U_f$  is clearly reversible.

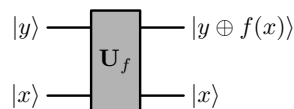


**Figure 2.1:** The general form of the reversible quantum circuit  $U_f$  corresponding to a classical logical circuit  $f$ .

### 2.2.1 Universal Gates

The family of classical operations on a single bit has only four members as there are only two possible input states and two output states. In contrast, the one qubit gate operations are all the members of the continuous group of unitary  $2 \times 2$  complex matrices,  $U(2)$ . Some of the ones we will encounter most frequently are the Hadamard gate  $\mathbf{H}$ , the NOT-gate  $\mathbf{X}$ , and the  $\mathbf{Z}$  gate, which in the canonical basis  $\{|0\rangle, |1\rangle\}$  have matrix representations

$$\mathbf{H} = \frac{1}{\sqrt{2}} \begin{pmatrix} 1 & 1 \\ 1 & -1 \end{pmatrix}, \quad \mathbf{X} = \begin{pmatrix} 0 & 1 \\ 1 & 0 \end{pmatrix}, \quad \text{and} \quad \mathbf{Z} = \begin{pmatrix} 1 & 0 \\ 0 & -1 \end{pmatrix}. \quad (2.3)$$

These are just three members of an infinite family of *idempotent* one qubit gates, *i.e.* gates which are a square root of the identity. In comparison, the only (non-trivial) idempotent classical one bit gate is the NOT-gate.

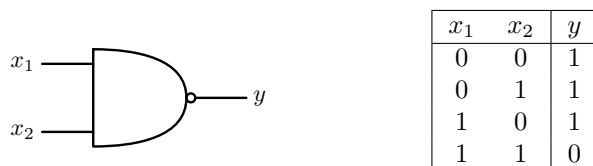


**Figure 2.2:** Symbol and truth table for the logical NAND-gate, which constitutes a universal set of gates for classical logical circuits.

If we consider classical logical circuits, it is relatively straight forward to see that all circuit can be constructed solely from NAND-gates (Fig. 2.2), *i.e.* the NAND-gate constitutes a *universal gate* for classical logical circuits. Having seen that the four possible classical one-bit gates turned into a multitude of one-qubit gates, we might expect that a set of universal gates for quantum circuits would be tremendous. It turns out, however, that all we need to obtain a set of universal gates from a set of universal one-qubit gates is one sufficiently powerful two-qubit gate [14, 15]. The typical choice for such a two-qubit gate is the controlled not, or CNOT, gate (Fig. 2.3).

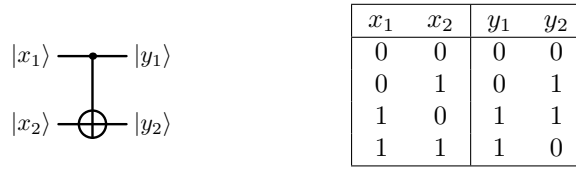


**Figure 2.3:** Symbol and truth table for the CNOT-gate, which together with a universal one qubit gate constitutes a set of universal quantum gates.

## 2.2.2 Reading Quantum Circuit Diagrams

We will, where appropriate, make use of quantum circuit diagrams of the type used in Fig. 2.3 as they are much easier to decipher than evolution matrices such as

$$\mathbf{U}^{(\text{CNOT})} = \begin{pmatrix} 1 & & & \\ & 1 & & \\ & & 0 & 1 \\ & & 1 & 0 \end{pmatrix}, \quad (2.4)$$

which would be the representation of the CNOT-gate in the standard basis  $\{|00\rangle, |01\rangle, |10\rangle, |11\rangle\}$ . In such diagrams, a vertical line is used to denote that an operation on the *target* qubit is conditioned on the state of the *control* qubit being  $|1\rangle$ .

One should be careful not to rely on ideas from classical logic when reading quantum circuit diagrams. As an example, the following relation

$$\begin{array}{c} |x_1\rangle \text{---} \text{---} |y_1\rangle \\ | \\ |x_2\rangle \text{---} \text{---} |y_2\rangle \end{array} = \begin{array}{c} |x_1\rangle \text{---} \text{---} |y_1\rangle \\ | \\ |x_2\rangle \text{---} \text{---} |y_2\rangle \end{array} \quad (2.5)$$

holds for the controlled  $\mathbf{Z}$  gate, as can be seen by direct calculation: The left-most diagram shows  $|x_1\rangle$  and  $|x_2\rangle$  to be the initial state of the control and target qubits, respectively. In terms of operators, the final state is consequently  $|y_1\rangle |y_2\rangle = (|1\rangle \langle 1| \otimes \mathbf{Z} + |0\rangle \langle 0| \otimes \mathbf{1}) |x_1\rangle |x_2\rangle$ , and expanding the operators we find the operation to be given by the expressly symmetrical expression  $\mathbf{1} - 2|1\rangle \langle 1| \otimes |1\rangle \langle 1|$ .

## 2.3 Quantum Algorithms

If we prepare the  $|x_1\rangle$  input register of the quantum circuit  $U_f$  (Fig. 2.1) in an equal superposition of all possible states, as can be done by applying a Hadamard transform to all qubits,

$$|s\rangle = \frac{1}{\sqrt{2^n}} \sum_{x=0}^{2^n-1} |x\rangle = \mathbf{H}^{\otimes n} |0\rangle, \quad (2.6)$$

we find that after applying  $\mathbf{U}_f$ , the output register will be in a superposition of all the different values assumed by  $f$ :

$$\mathbf{U}_f |s\rangle |0\rangle = \frac{1}{\sqrt{2^n}} \sum_{x=0}^{2^n-1} |x\rangle |f(x)\rangle, \quad (2.7)$$

we have, by one application of the circuit implementing  $\mathbf{U}_f$  evaluated  $f$  for all input values. The problem with *quantum parallelism* is getting any useful information out of the register. If we just measure  $y_2$  the answer will be a random output of  $f$ , weighted by the relative frequency of that output value: we could have obtained the same information by evaluating  $f$  for a random input on a classical computer.

A central insight of quantum computing, first arrived at by Deutsch [4], is that if posed just right, some problems do have enough structure that the output of a quantum evaluation is useful. Two key examples of such *quantum algorithms* are Grover's search algorithm [6] and Shor's factorization algorithm [5, 16], which we will now briefly describe.

### 2.3.1 Grover's Search Algorithm

Grover's search algorithm addresses the following problem: We are given an *oracle* or *black box* that implements  $\mathbf{U}_f$  for a function  $f$  of the form

$$f(x) = \begin{cases} 1 & \text{if } x = \chi \\ 0 & \text{otherwise,} \end{cases} \quad (2.8)$$

and are challenged to find the one value of  $x$  for which  $f$  is non-zero.

Classically, our best approach would be to simply evaluate  $f$  for different values of the  $n$ -bit input register until arriving at  $\chi$ , after on average on the order of  $N = 2^n$  attempts. With quantum computing, the problem can be solved much faster. Since Grover's algorithm, which performs this feat, is one of the few quantum algorithms that we can understand without heavy formalism, we will now consider in some detail how this is done. Before doing so, we will replace our black box  $\mathbf{U}_f$  with a circuit that flips the sign of the  $|\chi\rangle$  component of the input:

$$\mathbf{U}_\chi = 1 - 2|\chi\rangle\langle\chi|. \quad (2.9)$$

To implement  $\mathbf{U}_\chi$  in terms of  $\mathbf{U}_f$ , we introduce an auxiliary *ancilla* qubit in the state  $|y\rangle = (|0\rangle - |1\rangle)/\sqrt{2}$ . Since  $\mathbf{X}|y\rangle = -|y\rangle$ , we see that operating with  $\mathbf{U}_f$  on  $|x\rangle|y\rangle$  will lead to a sign change exactly if  $x = \chi$ . As the state of the ancilla is unchanged through the procedure, we need not consider it further. To avoid cumbersome notation, we will consider the specific example of an oracle operating on a 3 qubit register, with a preference for the state  $|5\rangle$ .

We start by initializing the register to an equal superposition state (2.6):  $|\psi_1\rangle = |s\rangle$ , which we will depict as

$$|\psi_1\rangle = \begin{array}{c} \begin{array}{cccccccc} \text{bar} & \text{bar} \\ |0\rangle & |1\rangle & |2\rangle & |3\rangle & |4\rangle & |5\rangle & |6\rangle & |7\rangle \end{array} \end{array} \quad (2.10a)$$

where the bars indicate the size and sign of the expansion coefficients on the basis states. Applying the oracle,  $U_\chi$ , will change the sign of the  $|\chi\rangle$  component. We can decompose the resulting state  $|\psi_2\rangle$  in a part proportional to the equal superposition state  $|s\rangle$  and a part orthogonal to  $|s\rangle$ . Since  $\langle s|\psi_2\rangle = 3/4$  we find:

$$|\psi_2\rangle = \frac{3}{4}|s\rangle + |s_\perp\rangle \quad (2.10b)$$

$$= \begin{array}{c} \begin{array}{cccccccc} \text{bar} & \text{bar} \\ |0\rangle & |1\rangle & |2\rangle & |3\rangle & |4\rangle & |5\rangle & |6\rangle & |7\rangle \end{array} \end{array}, \quad (2.10c)$$

where the dashed line indicates the mean, or equivalently the contribution from  $|s\rangle$ . Now comes Grover's trick: if we apply an 'inversion about the mean' defined formally as  $U_s = 2|s\rangle\langle s| - 1$ , we see that all amplitudes are inverted about the mean amplitude, leaving the amplitude of the  $|\chi\rangle = |5\rangle$  state by far the largest:

$$|\psi_3\rangle = \begin{array}{c} \begin{array}{cccccccc} \text{bar} & \text{bar} & \text{bar} & \text{bar} & \text{bar} & \text{tall bar} & \text{bar} & \text{bar} \\ |0\rangle & |1\rangle & |2\rangle & |3\rangle & |4\rangle & |5\rangle & |6\rangle & |7\rangle \end{array} \end{array}. \quad (2.10d)$$

More precisely we find that the  $|5\rangle$  coefficient of  $|\psi_3\rangle = U_s U_\chi |\psi_1\rangle$  is seven times as large as the other coefficients. If we measure the state of the register at this point we will obtain the correct answer,  $|5\rangle$ , with a probability of  $7^2/(7^2 + 7)$  or 87.5%, after having applied the oracle only once.

In general, we must apply the *Grover's iterator*  $U_s U_\chi$  on the order of  $\sqrt{N}$  times for the outcome to be the "good" state with certainty. We will return to a more precise description of the *amplitude amplification* process in chapter 10.

**Applications of Grover's Algorithm.** Grover's algorithm is often described as a "database search" algorithm. While it could certainly be used for searching a quantum database, should one ever be available, a more obvious application would be calculating inverse images under "one way functions". Such functions are much used in cryptology: as an example are computer passwords rarely stored as raw text, but more often in terms of the output from a one way function.

### 2.3.2 Shor's Factoring Algorithm

Even more impressive than the  $\mathcal{O}(N)$  to  $\mathcal{O}(\sqrt{N})$  speedup obtained by Grover's algorithms is the performance of Shor's factoring algorithm [16], which can factor a number exponentially faster than the best classical algorithm, the number field sieve [12]. Shor's algorithm is a representative of the hidden subgroup problem [17], which contain all the examples of exponential speedup in quantum algorithms known at the time of writing.

As for Grover's algorithms, the successful implementation of Shor's algorithm would have dire consequences for cryptography, as the security of many public key cryptosystems, such as RSA<sup>1</sup>, is based on the difficulty of factoring large integers.

## 2.4 Building a Quantum Computer

At first impression, the task of stabilizing quantum information seems impossible as, unlike the discrete states of a classical bit, the qubit states are a continuous family, making it possible for infinitesimal errors to slowly accumulate. As we will now see, it is indeed possible to apply error correction to quantum systems, removing the last theoretical obstacle in the road towards quantum computing.

### 2.4.1 Quantum Error Correction

The central realization of quantum error correction is that we do not need to worry about the full infinity of possible errors: If we can make an error correcting scheme that corrects all single qubit bit-flip errors, described by the operator  $\mathbf{X}$ , phase errors  $\mathbf{Z}$  and combined phase and bit-flip errors  $\mathbf{XZ}$ , the scheme will protect against any single qubit error [7, 18]. Protecting against such a discrete family of errors can be done by error correcting codes [8].

Error correcting codes work by redundantly encoding a single *logical qubit* in several physical qubits. To take a simple example, we can protect against bit-flip errors by using the logical states  $|0_L\rangle = |000\rangle$  and  $|1_L\rangle = |111\rangle$ . It is possible to unitarily calculate *error syndromes* describing if and if so where a bit-flip has

---

<sup>1</sup> The RSA algorithm is named after its inventors: Ronald L. Rivest, Adi Shamir, and Leonard Adleman.

occurred, allowing us to recover from the error by applying an additional bit-flip to that qubit. Many different error correcting codes have been devised: both purely logical as described here, and codes relying on *decoherence free subspaces* of particular quantum computing implementations.

The most important consequence of the discovery of quantum error correction is the *Threshold theorem*, which states that a quantum computer implementation does not need to be perfect: as long as it operates with an error rate below a certain threshold it will be able to recover from errors faster than they occur. We will assume a threshold error rate on the order of  $10^{-4}$ , but the actual value depends critically on the details of the quantum computing system in question.

## 2.4.2 The DiVincenzo Criteria

With the threshold theorem removing the last theoretical objection against quantum computing, a large number of different proposals for quantum computer implementations are being pursued both experimentally and theoretically. This activity has also led to much interest in the closely related field of quantum information theory, and has spurred a renewed interest in the nature of decoherence and the distinction between quantum and classical [19, 20].

QC Approach	DiVincenzo criteria				
	1	2	3	4	5
NMR	–	?	?	+	?
Trapped Ion	?	+	?	+	+
Neutral Atom	?	+	?	?	?
Cavity QED	?	+	?	?	+
Optical	?	?	+	?	?
Solid State	?	?	?	?	?
Superconducting	?	+	?	?	?
REQC	?	+	?	?	+

**Table 2.1:** Meeting the DiVincenzo criteria. An assessment of the promises of some of the central proposed quantum computing platforms, adapted from Ref. [21] - REQC has been added by the author. The legends are: +: a potentially viable approach has achieved sufficient proof of principle. ?: a potentially viable approach has been proposed, but there has not been sufficient proof of principle. –: no viable approach is known.

In Ref. [22], DiVincenzo provides an excellent overview of the practical requirements for a quantum computing system. In particular, the following five point checklist has become a standard against which all proposals are measured:

1. A scalable physical system with well characterized qubits.
2. A method for initializing the system to a known quantum state.
3. The qubit decoherence time must be much longer than the time necessary for gate operations.
4. A universal set of quantum gates.

5. A read-out method.

Table 2.1 shows how the most important proposals measure up against the checklist: we will not discuss this information further, but refer to the QIST Quantum Computing Roadmap [21] for a detailed discussion.

## 2.5 Summary

In summary, quantum computing has over the last twenty years evolved from a theoretical curiosity to a point where the realization of a quantum computer seems to be mainly a matter of time. The key insights that have made this possible and interesting are the discovery of the threshold theorem, and the related techniques for quantum error correction, together with the discovery of quantum algorithms that vastly outperform their classical counterparts.

We have also established a list of criteria, that have to be met by a prospective quantum computing system. The remainder of this thesis will to a large degree be devoted to determining if we can make the REQC-proposal meet these requirements.



## CHAPTER 3

# Rare-Earth-Ion-Doped Inorganic Crystals

In this chapter, we introduce the central features of rare-earth-ion doped crystals from a quantum information processing point of view. The main goal is to establish and motivate the simple model of the system which we will use in the following chapters.

Rare-earth ions, embedded in a variety of solid state host materials, are the central part of many active optical applications, including laser crystals [23] and amplifying waveguides in glasses [24] and polymers [25]. Common to these applications is the fact that the optical properties are very well described by a frozen-gas model, in which the optical properties are ascribed to the individual rare-earth ions, which behave almost as free ions, and are only mildly perturbed by the field of the host material [26].

To motivate the frozen gas model, we will in the first section of this chapter study the electron structure of the rare-earth elements: Inside the chemically active  $6s$  and  $5d$  electrons, the rare-earths have a full  $5s^25p^6$  shell shielding a partially filled  $4f$ -subshell. The rich optical spectrum of the rare-earth ions can be attributed to transitions between different  $4f^n$  states, and the second section discusses how these states are influenced by the crystal field, both with respect to inhomogeneous effects, in particular inhomogeneous broadening, which are constant in time but differ between ions, and with respect to homogeneous effects: line broadening and decoherence mechanisms affecting all ions equally.

Unlike most current applications, where interactions between the individual ions are considered a nuisance, a quantum computing system based on rare-earth-ion doped crystals require strong interactions to mediate multi-qubit gate operations. In the final section of the chapter, we will describe the interaction between the static dipole moments of the dopant ions.

### 3.1 Chemical Properties

The rare-earth elements, also known as the Lanthanides, are characterized by a partially filled  $4f$  subshell inside filled  $5s$  and  $5p$  subshells: During the iterative construction (aufbau) of the periodic table (see Fig. 3.1 for the relevant part), the strong spin-orbit coupling of the  $4f$  electrons makes it energetically favorable to defer the filling of the  $4f$  subshell until the  $6s$ ,  $5s$  and  $5p$  subshells, with lower spin orbit coupling energies, have been filled [27]. As illustrated by Fig. 3.2 the

	39Y			
K	2			
L	2	6		
M	2	6	10	
N	2	6	1	
O	2			

	40Zr			
	2			
	2	6		
	2	6	10	
	2	6	2	
	2			

	57La				58Ce			
K	2				2			
L	2	6			2	6		
M	2	6	10		2	6	10	
N	2	6	10		2	6	10	2
O	2	6	1		2	6		
P	2				2			
	s	p	d	f	s	p	d	f

	70Yt			71Lu			72Hf		
	2			2			2		
	2	6		2	6		2	6	
	2	6	10	2	6	10	2	6	10
	2	6	10	14	2	6	10	14	14
	2	6		2	6	1	2	6	2
	2			2			2		
	s	p	d	f	s	p	d	f	s

**Figure 3.1:** Electron configurations of the Lanthanides (marked with blue background) and surrounding elements. Numbers indicate the number of electrons in a given subshell. The Lanthanides are characterized as having a partially filled  $4f$  subshell inside full  $5s$  and  $5p$  subshells. The  $4f$  shell is filled in close competition with the  $5d$  subshell leading to some disagreement as to which elements should be considered Lanthanides. The figure adheres to what appears to be the most common point of view, that the Lanthanides are the elements between Lanthanum ( $Z = 57$ ) and Ytterbium ( $Z = 70$ ), both included.

$4f$  orbitals are spatially located within the  $5s$  and  $5p$  orbitals, a fact which is vividly illustrated by an effect known as the *Lanthanide contraction*: due to the increased screening of the core as the  $4f$  shell is gradually filled, the diameter of the Lanthanide atoms, which is defined by the filled  $5s, p$  subshells, decreases through the Lanthanide series.

As mentioned in the introduction of the chapter, rare-earth ions are employed in variety of host types, ranging from polymers over glasses to crystals. Here, we will only consider the case of trivalent rare-earth ions embedded in mono-crystalline inorganic crystals, substituting for chemically similar ions such as Yttrium (Fig. 3.1). Typical doping levels will be on the order of 0.1% of the possible substitution sites being populated by rare-earth ions, so that the host crystal structure is only mildly perturbed.

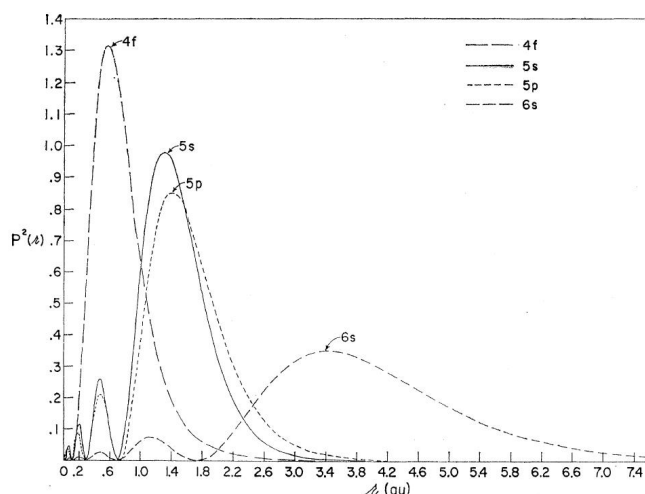


**Figure 3.2:** A theoretical prediction of the radial distribution of the orbitals of a rare-earth ion ( $\text{Gd}^{3+}$ ). The  $4f$  orbital is seen to lie inside the  $5s$  and  $5p$  orbitals. Illustration from Ref. [28].

## 3.2 Optical Properties

The optical properties of trivalent rare-earth ions are dominated by transitions between  $4f^n$  states. The overall level structure of rare-earth ions embedded in a solid host is similar to that of the corresponding free ions, a fact traditionally attributed to the screening effect of the filled  $5s^2 5p^6$  shell surrounding the active  $4f$  electrons, as discussed in the previous section. When the host material is not itself optically active, as is the case for the inorganic crystals considered here, this fact allows us to consider the system to be a *frozen gas* of ions. One important exception to this picture is the presence of *inhomogeneous broadening*: apparent broadening of *homogeneous* spectral features due to random but constant shifts of the individual ions being observed.

### 3.2.1 Typical Level Structure

The most obvious difference between the spectrum of the free ion and that of the crystal-embedded ion is that the induced anisotropy in most cases completely removes the degeneracy of the  $J$  manifolds, splitting each into at most  $2J+1$  levels as illustrated in Fig. 3.3. Typically, this splitting is on the order of 1-10 THz. At liquid helium temperatures, this is well above the thermal phonon spectrum so that the transitions are not broadened by thermal phonons. The levels are, however, susceptible to decay by spontaneous phonon emission, leading to homogeneous broadenings of 1-100 GHz or more. How the  $J$  manifolds are split by the crystal field is mainly determined by the symmetry properties of the

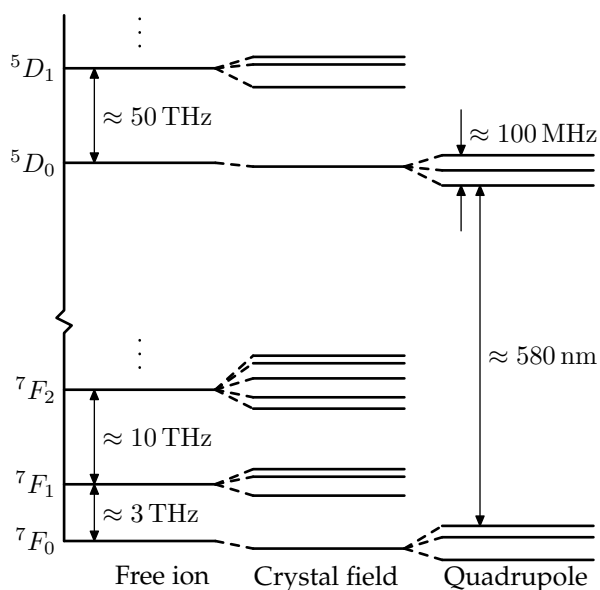


**Figure 3.3:** Sample energy diagram of a trivalent rare-earth ion with typical energy scales. Levels belonging to different  $J$ -values are split by the spin orbit interaction, with typical separations on the order of a few THz. The degeneracy of each  $J$ -manifold is usually completely lifted by the crystal field, also causing the inhomogeneous broadening. The degeneracy of the hyperfine levels is lifted by quadrupole and pseudo-quadrupole interactions. The figure is drawn for  $\text{Eu}^{3+}:\text{Y}_2\text{SiO}_5$ , according to [26, 29]

host crystal, but one finds that the general structure of the level diagram of a given crystal-embedded rare-earth ion is largely independent of the host crystal. An overview of this general level structure for all the trivalent rare-earth ions is presented in a table compiled by Dieke [30], which can be found in an amended version for instance in the book by Kaplyanskii and MacFarlane [26].

The gem of rare-earth spectroscopy are the so-called *lowest-to-lowest transitions*: The splitting between the different  $J$ -manifolds, caused by the spin-orbit interaction, is often larger than the maximal phonon frequency in the crystal, requiring the lowest state of each manifold to decay by multi-phonon decays, leading to life times of up to several ms. In general, the observed linewidths of the lowest to lowest transitions are slightly larger than the limit set by the life time of the excited state. The dominant remaining contributions to the line broadening are spin-fluctuations in the host crystal and ion-ion dipole interactions. [26, 31].

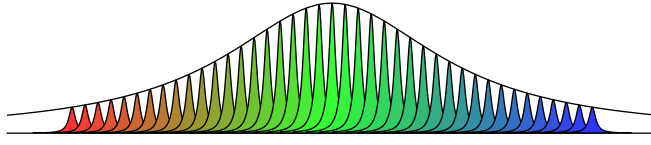


**Figure 3.4:** Inhomogeneous broadening. Due to variations in the crystal field, the optical transitions of the dopant ions will be randomly shifted. As a consequence, spectroscopic experiments simultaneously interacting with an ensemble of ions will observe an *inhomogeneous linewidth*, illustrated by the broad Lorentzian envelope in the figure, which is much wider than the *homogeneous linewidth*: the linewidth of the individual ions, as illustrated by the small Lorentzian peaks. The figure is grossly out of scale: in typical applications, the inhomogeneous width will be tens of GHz, compared to homogeneous linewidths on the order of kHz.

### 3.2.2 Hyperfine Structure

Within each level in the  $J$ -manifolds, any residual degeneracy allowed by the degrees of freedom related to the nuclear spin are usually at least partially lifted by hyperfine interactions. The most important of these are included in the following hyperfine Hamiltonian [26] :

$$H_S = H_{\text{HF}} + H_Q + H_Z + H_z, \quad (3.1)$$

where  $H_{\text{HF}}$  refer to the hyperfine interaction between  $4f$  electrons and the ion nucleus,  $H_Q$  to the nuclear electric quadrupole interaction and  $H_Z$  and  $H_z$  to the nuclear electric quadrupole interaction and the electron and nuclear Zeeman interactions respectively. Although the resulting hyperfine states are usually labeled by the angular momentum quantum numbers of their primary components, there is usually so much mixing that the selection rules for optical transitions do not apply [32], which of course greatly increases the possibilities of coherent manipulation of the ions with optical fields.

Phase coherence times between the hyperfine levels can be very high: for Pr:Y<sub>2</sub>SiO<sub>5</sub>, decoherence times of 500 μs have been observed in an unmodified system [33]. The main factor causing the observed hyperfine decoherence in this system is magnetic interaction with the spins of the host Yttrium nuclei. This interaction can be reduced in two ways: by reducing the fluctuations of the host nuclear spins or by reducing the sensitivity of the rare-earth ions to such fluctuations.

The fluctuations of the host nuclear spins can be reduced by aligning the spins using an external magnetic field. By this method, a line-width of 100 Hz, very close to the limit set by the decay rate, have been reached for the  $^5D_0$ - $^7F_0$  transition of Eu<sup>3+</sup>:Y<sub>2</sub>SiO<sub>5</sub> [34], which has an uncompensated linewidth of 387 Hz [35].

The sensitivity of the rare-earth ions to a fluctuating field can be reduced by introducing an external magnetic field as follows [32]: A second order perturbation analysis of the effect of the spin Hamiltonian  $H_S$  yields the following form

[31]:

$$H_S^{(2)} = \mathbf{B} \cdot \mathbf{M}_{BB} \cdot \mathbf{B} + \mathbf{B} \cdot \mathbf{M}_{BI} \cdot \mathbf{I} + \mathbf{I} \cdot \mathbf{M}_{II} \cdot \mathbf{I}, \quad (3.2)$$

where  $\mathbf{B}$  is the magnetic field vector, and  $\mathbf{I}$  is the nuclear spin operator. From (3.2), we see that applying a static magnetic field  $\mathbf{B}_0$ , at which the first order dependence of  $H_S$  on  $\mathbf{I}$  vanishes, will remove the first order sensitivity of the hyperfine splitting to the fluctuating magnetic field caused by nearby spins. Using this technique, hyperfine coherence times of 82 ms have been experimentally demonstrated for the Pr:Y<sub>2</sub>SiO<sub>5</sub> system by Fraival *et al.* [32].

### 3.2.3 Inhomogeneous Broadening

So far, we have considered only *homogeneous* effects: that is effects which affect all ions equally. What really sets the crystal-embedded ions apart from a gas of free ions (or atoms) is that the ions in a crystal will all have slightly different surroundings due to impurities, defects, or crystal strains caused by the crystal solidifying at finite temperatures. The shifts of the energy levels of the ions caused by these environmental differences are referred to as *inhomogeneous shifts*: they affect each ion in a constant but random way. When we consider the ensemble of ions in a crystal, such random shifts of the optical transition frequencies of the ions will appear as a broadening of the spectral lines (Fig. 3.4).

For the materials considered here, the inhomogeneous broadening of the optical transitions can be as high as several tens of GHz. The hyperfine splittings are much less affected by inhomogeneous effects, and typical inhomogeneous broadenings of the hyperfine transitions are on the order of tens of kHz.

## 3.3 Ion Interactions

So far, we have considered the rare-earth ions in a crystal to be independent. Fortunately, the ions do interact, a fact which is considered an annoyance from the point of view of rare-earth-ion spectroscopy, but will prove to be crucial for quantum information processing in rare-earth-ion doped crystals. We will only consider the dominant electric dipole interactions, and ignore other interaction modes, such as phonon exchange, which are generally much weaker [26].

### 3.3.1 Rare-Earth-Ion Dipole Moments

As the electric dipole moment of the rare-earth ions is defined by the electronic configuration, we will for simplicity ignore the hyperfine structure and related selection rules in this section. This allows us to restrict our attention to two ionic states,  $|e\rangle$  and  $|g\rangle$ , which we assume to be lowest lying members of two different  $J$ -multiplets, connected by an optical transition.

For a free ion, rotational invariance requires the diagonal elements  $\mu_{ee}$  and  $\mu_{gg}$  of the electric dipole operator, to vanish. In the anisotropic setting of a

crystal this requirement is lifted, and large static dipole moments induced by the crystal field are actually observed for the trivalent rare-earth ions in most hosts. In  $\text{YAlO}_3$ , a clever pulse-echo technique can be employed to measure the Stark shift, corresponding to the interaction of  $\Delta\boldsymbol{\mu} = \boldsymbol{\mu}_e - \boldsymbol{\mu}_g$  with a static external electric field. By this method, Stark coefficients of  $33.7 \text{ kHz/V cm}^{-1}$  for  $\text{Eu}^{3+}$  and  $141.7 \text{ kHz/V cm}^{-1}$  for  $\text{Er}^{3+}$  in  $\text{YAlO}_3$  have been measured [36, 37], corresponding to the  $\Delta\mu$  being on the order of  $2\text{-}8 \times 10^{-31} \text{ C m}$  [29].

In order to compare the observed magnitude of the diagonal elements of the dipole operator with that of the off-diagonal elements  $\boldsymbol{\mu}_{eg}$ , we can use that  $\boldsymbol{\mu}_{eg}$  is related to the partial decay rate  $\Gamma$  of the  $|e\rangle\text{-}|g\rangle$  transition by  $\mu_{eg}^2/4\pi\epsilon_0 = \frac{3}{4}\hbar\Gamma\lambda^3$ , where  $\lambda$  is the reduced wavelength  $\lambda/2\pi$ . Since the life time of the excited state  $|e\rangle$  in a lowest to lowest transition is dominated by dipole decay, we can approximate  $\Gamma$  with the total decay rate of  $|e\rangle$ . For optical transitions with linewidths on the order of a kHz, as in the case of  $\text{Eu}^{3+}:\text{YAlO}_3$ , this corresponds to dipole moments on the order of  $10^{-31} \text{ C m}$ , which we note to be of same magnitude as the diagonal elements.

### 3.3.2 Dipole Interaction

The analysis of dipole interactions is greatly simplified when retardation effects can be ignored, that is, when we do not need to take the finite speed of light into account. Retardation effects become important at distances on the order of the reduced wavelength  $\lambda$  of the transition. As we shall see below, the dipole interactions will in the present case be negligible at this distance, and we will consequently not consider retardation effects further. For a review of the retarded interaction in rare-earth-ion doped crystals see for instance Ref. [38].

The non-retarded dipole interaction energy is nothing more than the classical interaction energy between static dipoles: For two dipoles with dipole moments  $\boldsymbol{\mu}_1$  and  $\boldsymbol{\mu}_2$ , this is given by the interaction energy of  $\boldsymbol{\mu}_1$  with the field of  $\boldsymbol{\mu}_2$ , which (ignoring local field effects [29]) has the form:

$$V_{\text{dd}}(\boldsymbol{\mu}_1, \boldsymbol{\mu}_2) = \frac{\mu_1\mu_2}{4\pi\epsilon_0} \frac{1}{r_{12}^3} [\hat{\boldsymbol{\mu}}_1 \cdot \hat{\boldsymbol{\mu}}_2 - 3(\hat{\boldsymbol{r}}_{12} \cdot \hat{\boldsymbol{\mu}}_1)(\hat{\boldsymbol{r}}_{12} \cdot \hat{\boldsymbol{\mu}}_2)], \quad (3.3)$$

where  $\boldsymbol{r}_{12} = \boldsymbol{r}_1 - \boldsymbol{r}_2$  is the relative position vector of the dipoles. The dipole interaction strength can be brought into the more intuitive form

$$V_{\text{dd}} = \hbar\Gamma \left( \frac{\lambda}{r_{12}} \right)^3 \frac{3}{4} \frac{\mu_1\mu_2}{\mu_{eg}^2} d(\hat{\boldsymbol{\mu}}_1, \hat{\boldsymbol{\mu}}_2), \quad (3.4)$$

where  $d(\hat{\boldsymbol{\mu}}_1, \hat{\boldsymbol{\mu}}_2)$  is the dimensionless geometrical factor appearing as the last term of (3.3). As we will prove in section 8.3, an absolute requirement for implementing a quantum gate operation is that the interaction strength is greater than the decay rate. Assuming that  $\mu_i$  are on the order of the transition dipole element  $\mu_{eg}$ , as we have seen to be the case for  $\text{Eu}^{3+} : \text{YAlO}_3$ , this implies by (3.4) that we must require the dipole separation to be significantly smaller than

the reduced wavelength  $\lambda$ , justifying our disregard of retardation effects. For optical transitions,  $\lambda \approx 100$  nm; for comparison, a typical dopant distance in  $\text{YAlO}_3$  at 0.5% doping is 2 nm.

### 3.3.3 Model Interaction Hamiltonian

Rewriting the individual ion dipole moments  $\mu$  as  $\mu = \delta\mu + \mu^{(0)}$ , relative to the ground state diagonal term  $\mu_i^{(0)} = \langle g | \mu_i | g \rangle$ , we find that since the interaction energy is clearly bilinear we have

$$V_{\text{dd}}(\mu_1, \mu_2) = V_{\text{dd}}(\mu_1^{(0)}, \mu_2^{(0)}) + V_{\text{dd}}(\delta\mu_1, \mu_2^{(0)}) + V_{\text{dd}}(\mu_1^{(0)}, \delta\mu_2) + V_{\text{dd}}(\delta\mu_1, \delta\mu_2).$$

The first term is a constant, corresponding to an energy shift of the whole system. The second and third terms describe constant shifts of the excited levels of the individual ions, which are part of the inhomogeneous shifts of those levels. As a consequence, all interaction between the dipole elements can be described in terms of  $V_{\text{dd}}(\delta\mu_1, \delta\mu_2)$ , so that  $\delta\mu_i$  are the effective dipole moments.

In terms of the effective dipole moments  $\delta\mu_i$ , only three matrix elements of the interaction are non-vanishing:

$$\hbar g_{12} = \langle ee | V_{\text{dd}}(\delta\mu_1, \delta\mu_2) | ee \rangle \quad (3.5a)$$

$$\hbar g_{12}^{\text{EE}} = \langle ee | V_{\text{dd}}(\delta\mu_1, \delta\mu_2) | gg \rangle \quad (3.5b)$$

$$\hbar g_{12}^{\text{EH}} = \langle eg | V_{\text{dd}}(\delta\mu_1, \delta\mu_2) | ge \rangle, \quad (3.5c)$$

so that including the free Hamiltonian of the ions,  $H_0 = \sum_i \hbar\omega_i(|e\rangle\langle e|)_i$ , the total Hamiltonian takes the following form in the basis  $\{|ee\rangle, |eg\rangle, |ge\rangle, |gg\rangle\}$ :

$$H_0 + V_{\text{dd}}(\delta\mu_1, \delta\mu_2) = \hbar \begin{pmatrix} \omega_1 + \omega_2 + g_{12} & 0 & 0 & g_{12}^{\text{EE}} \\ 0 & \omega_1 & g_{12}^{\text{EH}} & 0 \\ 0 & g_{12}^{\text{EH}*} & \omega_2 & 0 \\ g_{12}^{\text{EE}*} & 0 & 0 & 0 \end{pmatrix}. \quad (3.6)$$

Of these terms, we will immediately dismiss  $g_{12}^{\text{EE}}$  which describes the energy non-conserving transition  $|gg\rangle \mapsto |ee\rangle$ . To argue more formally for this, we could consider that changing to a basis rotating with the ions, this term would rotate as fast as the counter-rotating part of an optical field which is ignored in the rotating wave approximation.

The remaining off-diagonal element,  $g_{12}^{\text{EH}}$  of the Hamiltonian describes *excitation hopping* transitions, where a unit of excitation ‘‘hops’’ from one ion to another [39]. Had  $|eg\rangle$  and  $|ge\rangle$  been degenerate, the excitation hopping would lead to a splitting between the symmetric and antisymmetric combination of  $|eg\rangle$  and  $|ge\rangle$  of  $2\hbar g_{12}^{\text{EH}}$ . In the general case, the correction to the eigenvalues is of second order in  $g_{12}^{\text{EH}}/(\omega_1 - \omega_2)$ . We will mainly be interested in dipole interaction between ions which are well separated in frequency, so that we can ignore the excitation hopping term: this point will be commented upon later when

we present the various proposals for quantum computing with rare-earth-ion doped crystals.

Ignoring both the off-diagonal elements of  $V_{\text{dd}}(\delta\mu_1, \delta\mu_2)$ , the only part left is  $g_{12}$ , which is seen to describe a shift of the multiply excited state  $|ee\rangle$ , so that we are left with the following simple model of the dipole interaction:

$$V_{\text{dd}}(\delta\mu_i, \delta\mu_j) \approx \hbar g_{ij} (|e\rangle \langle e|)_i \otimes (|e\rangle \langle e|)_j. \quad (3.7)$$

When a group of ions are simultaneously excited, the dipole coupling (3.7) will lead to shifts of the excited states of all other ions. Since the shift experienced by any single ion will depend critically on the position of nearest ions of the excited group, this will lead to an *instant diffusion* of any spectral feature, providing a clear demonstration of the dipole interaction (3.7). We will study this phenomenon in much detail in chapter 9, and will just mention at this point that the observed broadening due to instant diffusion agrees with the magnitudes of the dipole elements estimated here. For the case of  $\text{Eu}^{3+}:\text{YAlO}_3$  at 0.5% doping, this corresponds to dipole coupling strengths on the order of GHz at typical dopant distances [40].

### 3.4 Summary

In summary, we have seen that rare-earth ions embedded in cryogenic crystals have a number of properties that make them interesting as quantum information processing hardware:

- Phase coherence times between ground state hyperfine levels as high as several ms have been observed, which together with gate time scales of  $\mu\text{s}$  allows us to use the ground state hyperfine levels as quantum registers.
- The optical transitions are inhomogeneously broadened by several GHz, due to variations in the crystal field. Since the homogeneous linewidths are as low as a few kHz, this allows us to address a large number of disjunct subsets of the ions by the value of their inhomogeneous shift (Fig. 3.4).
- Due to the field anisotropy caused by the host crystal, the ions acquire static dipole moments. The interaction between these, as modeled by (3.7), can be used to mediate quantum gate operations.



# CHAPTER 4

## Introduction to Quantum Computing with Rare-Earth-Ion Doped Crystals

If we had a way of picking specific ions in a rare-earth-ion doped crystal, it would be relatively simple to build and operate a quantum computer: If we chose the ions at different inhomogeneous detunings and close together, we could manipulate them independently by coherent optical fields of different frequencies, and the dipole-dipole coupling would allow us to implement multi-qubit gate operations. Unfortunately, it is not at all clear how to address single embedded ions in a crystal, not to mention how to read out the final state.

Instead, Kröll and co-workers have suggested to use an ensemble of quantum computers running in parallel in a crystal, so that the read-out could be performed by absorption spectroscopy, yielding an ensemble average of the qubit state [40]. Ensemble quantum computers have to be operated differently from standard projective measure quantum computers, but they are essentially equally powerful.

The central idea of the REQC proposal is that the ions of different *frequency channels* are interspersed throughout the crystal. By deactivating some of the ions, we can achieve a configuration where each remaining ion is within interaction distance of exactly one member of all other channels, thus being part of an *instance* of the quantum computer. How to perform this *initialization* will be the subject of the first two sections of the chapter. By means of optical field, we can address all members of a channel simultaneously, thus operating all the instances in parallel. In section 4.3, we give an example of how this can be used to implement gate operations, a subject we will discuss in much more detail in chapters 5, 6, and 7. The defining quality of an ensemble quantum computer

is that we read out an expectation value of the qubit registers, implying that the algorithms described in chapter 2 cannot be used directly. In section 4.4, we describe how and to what degree, quantum algorithms can be adapted to ensemble quantum computing. Finally, in the last section of the chapter, we will briefly describe two alternative proposals for quantum computing systems based on rare-earth-ion doped crystals.

## 4.1 Digging Channels

In Fig. 4.1(a) we introduce an idealized level diagram of a rare-earth ion: two ground state hyperfine levels labeled  $|0\rangle$  and  $|1\rangle$  will be used as qubit levels, while a third level  $|aux\rangle$  will be used to park unwanted ions. As illustrated by the arrows, we assume all three ground state levels to be connected by optical transitions to the excited state  $|e\rangle$  which is inhomogeneously shifted by an amount  $\delta$  away from the the channel center level. We are interested in addressing different frequency *channels*, that is: groups of ions with nearly identical inhomogeneous shifts,  $|\delta| < \Delta^{(chan)}$  (Fig. 4.1(b)). In order to be able to manipulate such channels without disturbing other ions, we must deactivate ions that have a transition frequency which is nearly resonant with the  $|0\rangle\text{-}|e\rangle$  or  $|1\rangle\text{-}|e\rangle$  transitions of a channel ion [41].

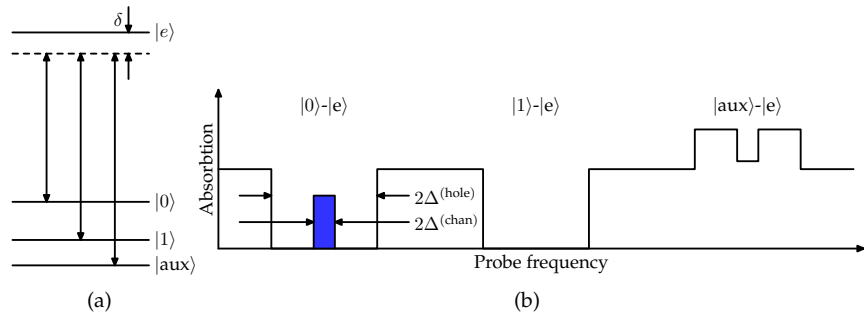


**Figure 4.1:** Schematic level diagram of a rare-earth ion (a).  $\delta$  denotes the inhomogeneous shift of the excited state with respect to the channel center value. (b) The schematic form of the absorption spectrum of an initialized channel.

The proposed way of doing this is conceptually simple: by first scanning a tunable laser around the two transition frequencies corresponding to the  $|0\rangle\text{-}|e\rangle$  and  $|1\rangle\text{-}|e\rangle$  transitions, we *optically pump* all ions away from states where they interact at this frequency, creating *holes* of width  $\Delta^{(hole)}$  in the absorption profile. After the holes have been emptied all members of the channel will be in their  $|aux\rangle$ -state, so that applying a pulse sequence that selectively transfers channel members from their  $|aux\rangle$  state to their  $|0\rangle$  state will result in the channel members appearing as an *anti-hole*: a narrow peak in the middle of the  $|0\rangle$ -hole in the absorption profile as illustrated in Fig. 4.1(b). An experimental setup for

performing this task is shown in Fig. 4.2. It should be noted that this setup is designed to initialize and manipulate a single channel, as its frequency range is limited to some hundreds of MHz by the bandwidth of the acousto-optic modulators.

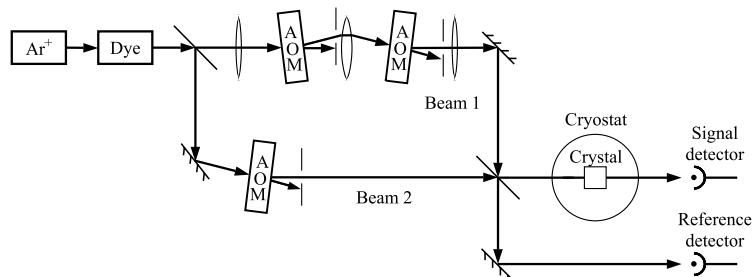


**Figure 4.2:** Experimental setup for manipulating channels in  $\text{Eu}^{3+}:\text{Y}_2\text{SiO}_5$ . The light from the dye laser is passed through acousto-optic modulators, which offset the frequency in order to match transitions from different hyperfine levels. The crystal is immersed in a cryostat with liquid Helium ( $\approx 4\text{ K}$ ) to avoid decoherence due to thermal phonons. To compensate for laser amplitude variations and modulator nonlinearity, detection of probe absorption is performed relative to the intensity of a reference beam. From Ref. [29].

As illustrated by Fig. 4.3, digging channels is not as simple as suggested here: many non-identical ions will absorb at a given frequency, especially when isotope shifts and the possibility of non-identical host sites are taken into account.

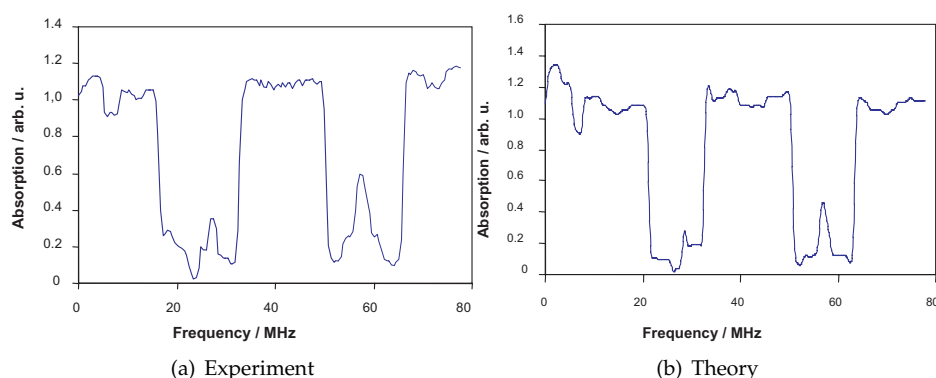


**Figure 4.3:** The experimental (a) and predicted (b) absorption profile of an  $\text{Eu}^{3+}:\text{YAlO}_3$  crystal after attempting to prepare a channel by burning two wells and transferring the atoms at the central frequency back to one of the qubit states. Figure (b) is based on a rate equation. From Ref. [29].

Deciding on the optimal channel parameters is not simple: Ideally, we would like the holes to be infinitely wide, so that we would not have to worry about

disturbing other ions. Unfortunately, this is not possible: A careful analysis [29] of the structure of transitions leading to the form of Fig. 4.3, imply that  $\Delta^{(\text{hole})}$  cannot exceed a limiting value on the order of (but somewhat smaller) the distance between the different transitions we wish to address. The finite width of the hole implies a minimal duration for laser pulses, since a pulse of duration  $\tau$  will always have frequency components on the order of  $1/\tau$ , implying that to not disturb ions on the edge of the channel holes, pulse duration must be larger than  $1/\Delta^{(\text{hole})}$ . Such a limit on the allowable pulse duration runs counter to our desire to use fast operations in order to minimize the probability of spontaneous decay from  $|e\rangle$ .

Similarly, there are conflicting interests with respect to the width of the anti-hole  $\Delta^{(\text{chan})}$ : It is clear that  $\Delta^{(\text{chan})}$  determines the concentration of channel members, so that even though anti-holes as narrow as 50 kHz have been experimentally demonstrated [42], we prefer a higher value of  $\Delta^{(\text{chan})}$  in order to obtain a higher concentration of channel members. On the other hand, this requires us to find ways of manipulating the ions that are *robust*, in the sense that they make all ions with a detuning smaller than  $\Delta^{(\text{chan})}$  evolve identically, while at the same time not disturbing ions outside the hole, *i.e.* ions with  $|\delta| > \Delta^{(\text{hole})}$ . It is clear that this requires us to choose  $\Delta^{(\text{chan})}$  significantly smaller than  $\Delta^{(\text{hole})}$ ; precisely how much smaller will be a central theme of this thesis.

## 4.2 Initialization

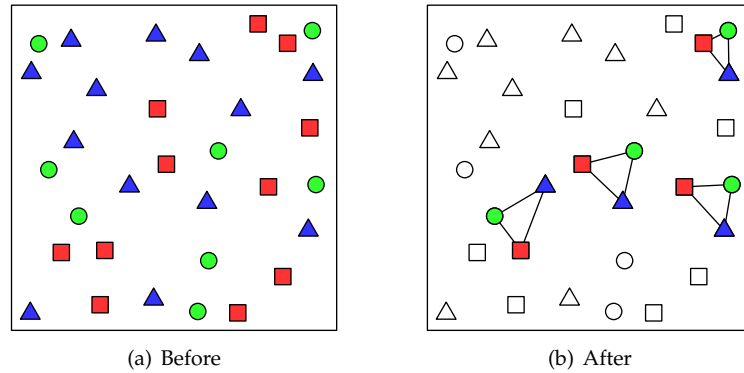


**Figure 4.4:** Rare-earth-ion doped crystal before and after initialization: The different shapes signify ions from different channels, which are distributed uniformly over the crystal (a). To obtain an ensemble quantum computer, those ions which are not part of an *instance* of the quantum computer are deactivated, leaving only the valid instances (b).

Initially, each channel has active ions distributed uniformly over the crystal, as illustrated by Fig. 4.4(a). To obtain an ensemble quantum computer we

need to deactivate those ions which are not part of an instance of the quantum computer, that is, the ions which are not within interaction distance of representatives of all the other channels as shown in Fig. 4.4(b). As we cannot physically remove the ions from the crystal, the deactivation is performed by moving unwanted ions to their auxiliary state  $|aux\rangle$  (Fig. 4.1(a)), a metastable ground state hyperfine level where the ion will not interfere with the further manipulation of the crystal, as long as we avoid addressing the  $|aux\rangle$ - $|e\rangle$  transition.

Since the dipole-dipole interaction is long range, whether or not two ions should be considered within interaction distance is a matter of choice. The threshold coupling strength,  $g_{min}$ , is the result of yet another compromise: As we will prove in section 8.3, there is a direct connection between the minimal gate error rate and  $g_{min}$ , so that a low value of  $g_{min}$  will unavoidably result in a high gate error rate. On the other hand, a high value of  $g_{min}$  reduces the number of available instances in the crystal.

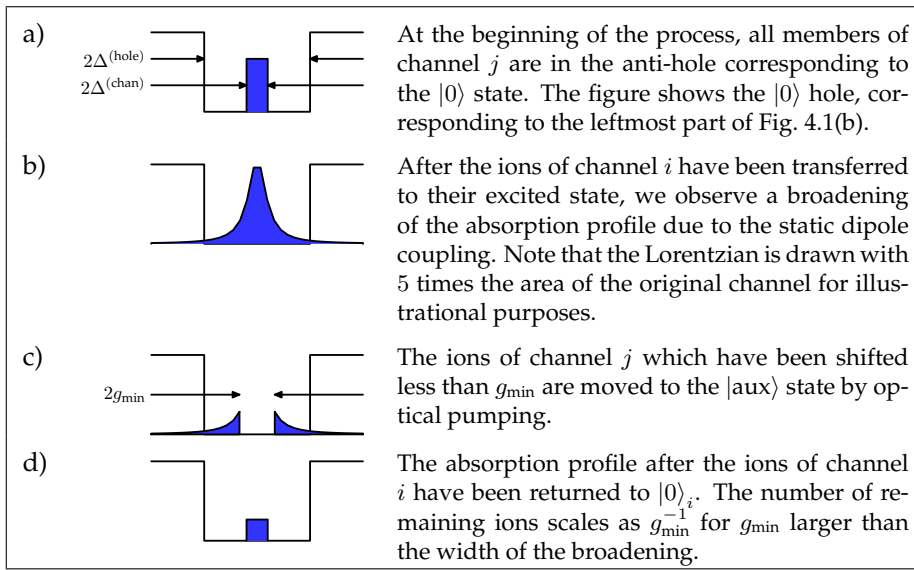


Figure 4.5: The initialization process.

The original REQC proposal describes the following initialization procedure [40]: Consider two channels,  $a$  and  $b$ . To deactivate all ions of channel  $b$  which are not coupled above the threshold  $g_{min}$  to an ion from channel  $a$ , we proceed as follows:

1. Transfer all ions of channel  $a$  to their excited state  $|e\rangle_a$  (Fig. 4.5 b).
2. Transfer all ions of channel  $b$ , which have not been shifted by more than  $g_{min}$  to their excited state (Fig. 4.5 c).
3. Return the channel  $a$  ions to  $|0\rangle_a$  (Fig. 4.5 d).
4. Wait for ions in  $|e\rangle_b$  to decay.
5. Optically pump ions out of  $|1\rangle_b$ .

## 6. Repeat.

Every time an unwanted ion decays from  $|e\rangle_b$ , there is a certain probability, that it will end up in  $|aux\rangle$ , and the number of times we have to repeat the above procedure in order to transfer most of the unwanted ions to their  $|aux\rangle$ -state depends on the branching ratios of the decay. Assuming all branching ratios to be equal, 50% of the unwanted ions will be transferred to  $|aux\rangle$  in each repetition, when the optical pumping out of  $|1\rangle$  is taken into account. In this case, we need  $\log_2(100) \approx 6.6$  repetitions of the above procedure to deactivate for instance 99% of all unwanted channel  $b$  ions. To avoid unwanted decay to  $|aux\rangle$  after the initialization, the system will normally be chosen to have a smaller branching ratio to  $|aux\rangle$ , requiring a larger number of repetitions during initialization.

By applying the above procedure to all pairs of channels, we will eventually arrive at the desired configuration where all remaining active channel members are part of a quantum computer instance: the REQC system has been *initialized*.

## 4.2.1 Bus Architecture

In [II] we suggest to use a *bus architecture* (Fig. 4.6(b)) where the members of an instance are only required to be coupled above threshold to a central *bus* qubit, instead of the fully interconnected architecture (Fig. 4.6(a)) originally proposed by Ohlsson *et al.*



**Figure 4.6:** Coupling in a fully coupled instance (a) and in a bus coupled instance (b), where the square denotes the bus qubit.

Using a bus architecture significantly simplifies the initialization of the system, since only  $n$  coupling strengths have to be checked as compared to  $\mathcal{O}(n^2)$  for a fully interconnected system. The lack of couplings between the outer qubits is not a problem with respect to gate implementation as a two qubit gate between any two outer qubits can be mediated by the central bus qubit:

$$\begin{array}{c}
 \text{---} \\
 \text{---} \\
 \oplus \\
 \oplus \\
 \oplus \\
 \oplus
 \end{array}
 =
 \begin{array}{c}
 \oplus \text{---} \oplus \\
 \text{---} \\
 \oplus \\
 \oplus \\
 \oplus
 \end{array}
 \quad (4.1)$$

Due to the lessened requirement for inter-ion coupling, more bus architecture

instances of a given size will be available than fully interconnected instances of the same size. We will discuss the advantages of the bus architecture in more detail in chapter 10, where we will also consider an asymmetric bus architecture.

### 4.3 A CNOT-Gate

Ohlsson *et al.* suggest [40] a CNOT-gate implementation based on the *dipole blockade* effect [44]. The idea of this gate implementation is to make use of the fact that the dipole interaction will shift the target ion out of resonance when the controlling ion is in its excited state, hence “blocking” the transition to a state where both ions are excited, as we have already made use of in the initialization procedure.

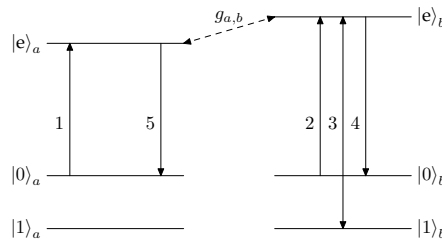


**Figure 4.7:** An implementation of the CNOT-gate due to Ohlsson *et al.* [40]. The numbers labeling the arrows indicate the order of pulses, while the arrow direction shows the resulting population transfer. Note that the third pulse (on the  $|1\rangle_b$ - $|e\rangle_b$  transition) must perform well for all initial states, while the other pulses are only required to perform well for a known initial state.

In order to understand the operation of the gate (Fig. 4.7), we write the initial state of the two qubits as  $|0\rangle|\psi_0\rangle + |1\rangle|\psi_1\rangle$  and consider the evolution the two components independently. For  $|1\rangle|\psi_1\rangle$ , we see that pulses 1 and 5 on the  $|0\rangle_a$ - $|e\rangle_a$  transition have no effect. This means that pulses 2-4 will be resonant, implementing a not operation on ion  $b$ . In contrast, we see that for the component  $|0\rangle|\psi_0\rangle$ , pulse 1 will transfer ion  $a$  to  $|e\rangle_a$  and consequently shift  $|e\rangle_b$  by  $g_{ab}$  making pulses 2-4 off-resonant. If the shift is sufficiently large, the off-resonant pulses will have no effect, and the state of ion  $b$  will remain unchanged. In total, we see that the gate operation is described by the truth table of the CNOT-gate (Fig. 2.3).

This gate implementation has several shortcomings, of which we will just mention some, in order to illustrate the type of problems we will be addressing in far more detail in chapters 5, 6 and 7. For one thing, an implementation in terms of square pulses would require us to use a very large ratio between  $\Delta^{(\text{chan})}$  and  $\Delta^{(\text{hole})}$  to obtain a good performance for all instances, and similarly, we would have to require a very large coupling threshold  $g_{\text{min}}$ . A less obvious problem is that the asymmetrical nature will unavoidably lead to phase errors due to the finite channel width.

## 4.4 Read-Out and Ensemble Algorithms

When we read out the state of a channel, the corresponding qubit ions in the individual instances will collapse to either the  $|0\rangle$  or  $|1\rangle$  states, but since we are addressing a macroscopic number of ions, the result of the measurement will be something in between, conveniently expressed as an ensemble average of  $\sigma_z$ . Experimentally,  $\langle\sigma_z\rangle$ , can be obtained e.g. through absorption spectroscopy or by addressing a cycling transition in the ion [45].

An *expectation value quantum computer* differs fundamentally from the standard *projective measure quantum computer* described in chapter 2. In this section, we study how quantum algorithms can be modified to work on an expectation value quantum computer. As the register expectation values can be statistically inferred from multiple readouts on a projective measure quantum computer, it is clear that projective measure quantum computing is at least as powerful as its expectation value counterpart. The difference in running time will be a constant factor determined by the precision of the expectation value readout, which is limited by the number of instances in the expectation value quantum computer, making the analogy to parallel computing obvious. It is also clear that projective measure quantum computers can do things that expectation value quantum computers cannot: For one thing, the readout from the expectation value quantum computer is completely determined by the deterministic master equation, while the projective measure quantum computer can generate true quantum randomness.

It is interesting to note that from an algorithmic point of view, pure state ensemble quantum computers (such as REQC) are equivalent to mixed state ensemble quantum computers (e.g. the NMR quantum computer) as both are fully described by the deterministic evolution of their density matrix.

Although projective measure quantum computers are able to perform a larger class of tasks than expectation value quantum computers, there are situations where the continuous value output from expectation value quantum computing make algorithms much simpler than their projective measure counterparts. One example of such a situation is the rotations estimation for a fully entangled state, which can be performed by one measurement on an expectation value quantum computer [II], but required thousands of repetitions in the 4-ion setup where it was originally implemented [46, 47]. As we will see below, a very similar situation is found in the case of *amplitude estimation*.

### 4.4.1 Quantum Database Search

We will now return to the quantum database search presented in chapter 2, and consider how it can be implemented in an expectation value quantum computing system. Rather than the one match problem considered earlier, we now address the more general problem, where we are requested to find a member of

a set  $\chi$  of matches,

$$\mathbf{U}_\chi |x\rangle = \begin{cases} -|x\rangle & \text{if } x \in \chi \\ |x\rangle & \text{if } x \notin \chi, \end{cases} \quad (4.2)$$

where we will assume the number  $M$  of elements in  $\chi$  to be known.

In the following, we describe a very elegant transformation of the Grover's problem into one of *quantum amplitude amplification* [48, 49], which was actually not described until a year after Grover's original paper [6].

### Quantum Amplitude Amplification

The oracle induces a decomposition of  $\mathcal{H}$  in a good part  $\mathcal{H}_a = \text{span}\{|x\rangle | x \in \chi\}$  and a bad part  $\mathcal{H}_b = \mathcal{H}_a^\perp$ . Starting from an initial state  $|s\rangle$ , the aim of the quantum amplitude amplification is to amplify the component  $|s_a\rangle$  of  $|s\rangle$  in  $\mathcal{H}_a$  until a measurement of the state will yield a member of  $\chi$  with certainty.

Based on our total ignorance, the initial guess is chosen to be an equal superposition of the computational basis states.

$$|s\rangle = \frac{1}{\sqrt{N}} \sum_{x=0}^{N-1} |x\rangle. \quad (4.3)$$

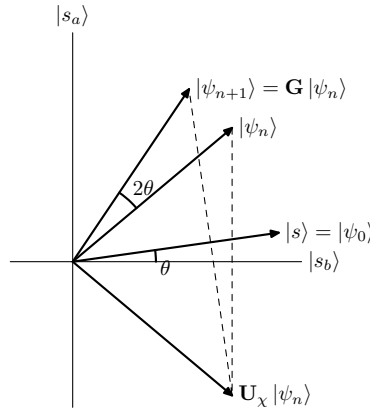


**Figure 4.8:** A geometrical interpretation of the Grover iteration: the two reflections,  $\mathbf{U}_s$  and  $\mathbf{U}_\chi$  maps  $|\psi_n\rangle$  to  $|\psi_{n+1}\rangle$ , corresponding to a rotation by twice the angle  $\theta$  between the reflection normals.

As in section 2.3.1, we introduce the inversion about the mean:

$$\mathbf{U}_s = 2 |s\rangle \langle s| - \mathbf{1}, \quad (4.4)$$

and the Grover iterate as

$$\mathbf{G} = \mathbf{U}_s \mathbf{U}_\chi. \quad (4.5)$$

The central observation made by Boyer *et al.* [50], is that the subspace  $\mathcal{H}_G = \text{span}\{|s_a\rangle, |s_b\rangle\}$  is invariant under the Grover iterate  $\mathbf{G}$ , in other words: as long as we only apply the Grover iterate, we stay within a two-dimensional subspace of  $\mathcal{H}$ .

Within  $\mathcal{H}_G$ , the Grover iteration has a simple geometrical interpretation (Fig. 4.8) as a rotation by an angle  $2\theta$ , where  $\theta$  is determined by the overlap between the initial guess  $|s\rangle$  and  $\mathcal{H}_a$ :  $\sin(\theta)^2 = \langle s|s_a\rangle$ . In the case where we have no information about the oracle and choose  $|s\rangle$  to be an equal superposition, this implies

$$\sin(\theta)^2 = \frac{M}{N}. \quad (4.6)$$

The objective is to rotate the state vector  $|\psi_n\rangle$  as close to  $|s_a\rangle$  as possible. The geometrical picture makes it clear that this will take  $\mathcal{O}(\sqrt{N/M})$  applications of  $G$  as (4.6) implies that  $\theta \approx \sqrt{M/N}$  to first order in  $M/N$ . If  $\theta$  or  $M$  is known, the optimal number of applications of  $\mathbf{G}$  is easily calculated. This approach can be further optimized by slightly modifying  $\mathbf{G}$  for all or only the last application, in order to map  $|s\rangle$  completely onto  $\mathcal{H}_a$  so that we find a match with certainty [49].

### Readout

After the amplitude amplification has been successfully performed, we expect to have the state  $|\psi\rangle$  entirely within  $\mathcal{H}_a$ . On a projective measure quantum computer, all that remains to be done to determine a member of  $\chi$  is to perform a measurement in the computational basis. On an expectation value quantum computer, a measurement in the computational basis would yield the expectation value of the register qubits, which is not of much use in a mixed state: consider for instance the state  $|\psi\rangle = 1/\sqrt{2}(|011\rangle + |110\rangle)$ :

$$\begin{array}{r} \sqrt{2} |\psi\rangle = \begin{array}{|c} 0 & 1 & 1 \\ 1 & 1 & 0 \end{array} \rangle + \\ \hline \langle \sigma_z \rangle = \begin{array}{|c} 0 & -1 & 0 \end{array} \end{array} \quad (4.7)$$

as  $\sigma_z = |0\rangle\langle 0| - |1\rangle\langle 1|$ . By repeated measurements, it is, however, possible to obtain a member of  $\chi$  by a method discovered by Collins [51]. The key idea of this method is the observation that if  $\langle \sigma_z^{(1)} \rangle$  indicate that qubit 1 is in a superposition state,  $|\psi\rangle$  must have at least one component with a first bit value of  $|b_1\rangle = |1\rangle$ . We now perform a controlled not from  $|b_1\rangle$  to the remaining qubits, obtaining  $|\psi'\rangle$

$$\begin{array}{r} \sqrt{2} |\psi'\rangle = \begin{array}{|c} 0 & 1 & 1 \\ 1 & 0 & 1 \end{array} \rangle + \\ \hline \langle \sigma'_z \rangle = \begin{array}{|c} 0 & 0 & -1 \end{array} \end{array} \quad (4.8)$$

If we now consider the difference between the  $\sigma_z$  and  $\sigma'_z$  expectation values, the expectation value for  $\sigma_z^{(i)}$  conditioned on qubit 1 being in state  $|1\rangle$  can be

derived. By repeating this procedure for all the qubits in superposition states a member of  $\chi$  can be identified.

On an expectation value quantum computer capable of non-demolition read-out, the conditioned read-out can be performed without redoing the amplitude amplification. As there are currently no suggestions for non-demolition measurements for the REQC system, we have to perform the amplitude amplification again for each bit with multiple values. This process is not expensive, as we will at most have to perform  $\mathcal{O}(\log(N))$  repetitions (one for each bit), resulting in an overall complexity of the algorithm of  $\mathcal{O}(\log(N)\sqrt{N})$ .

To reduce the price of redoing the amplitude amplification, we can modify the original guess  $|s\rangle$  to include the bit-values we now know to be represented, thus enlarging the rotation angle  $\theta$  and reducing the number of iterations. Another reduction in the number of iterations comes from the fact that  $|\psi\rangle$  does not have to be rotated entirely into  $\mathcal{H}_a$ : as long as we can tell  $|0\rangle$  from  $|1\rangle$ , the amplification has been sufficient.

### Amplitude Estimation

To use quantum amplitude amplification for quantum searching, we need to know in advance how many times to iterate as determined by  $\theta$ . If  $M$  is known, we can calculate  $\theta$  by (4.6), if not, we would like to be able to determine it by other means. This problem is known as *quantum amplitude estimation*.

On a projective measure quantum computer, amplitude estimation is a rather complicated task [49]. The basic idea is to use an algorithm for quantum period finding to find the period of the function  $m \mapsto \mathbf{G}^m |s\rangle$ , as this is given by  $2\pi/\theta$ .

In contrast to this complicated algorithm, a simple method exists for amplitude estimation on an expectation value quantum computer [52]: Given a state vector  $|\psi\rangle = |\psi_a\rangle + |\psi_b\rangle$  where  $|\psi_a\rangle \in \mathcal{H}_a$  and  $|\psi_b\rangle \in \mathcal{H}_b$ , our goal is to determine  $\sin^2(\theta) = \langle \psi | \psi_a \rangle$ . To do this, we introduce an ancilla in the state  $(|0\rangle + |1\rangle)/\sqrt{2}$ , and apply  $\mathbf{G}$  to  $|\psi\rangle$  conditioned on the state of the ancilla. Since we know  $\mathbf{G}$  to be a rotation by  $2\theta$  in  $\mathcal{H}_G$ , it will have eigenstates  $|s_{\pm}\rangle$  with eigenvalues  $e^{\pm i\theta}$ . Writing the state before applying the conditioned Grovers iterate as

$$|\Psi_1\rangle = \frac{1}{\sqrt{2}}(|0\rangle + |1\rangle) \otimes (c_+ |s_+\rangle + c_- |s_-\rangle), \quad (4.9)$$

the state after applying the iterate followed by a Hadamard transform on the ancilla is seen to be

$$|\Psi_2\rangle = c_+ e^{i\frac{\theta}{2}} \left( \cos\left(\frac{\theta}{2}\right) |0\rangle - i \sin\left(\frac{\theta}{2}\right) |1\rangle \right) |s_+\rangle + c_- e^{-i\frac{\theta}{2}} \left( \cos\left(\frac{\theta}{2}\right) |0\rangle + i \sin\left(\frac{\theta}{2}\right) |1\rangle \right) |s_-\rangle, \quad (4.10)$$

so that we find<sup>1</sup>  $\langle \sigma_z \rangle$  for the ancilla to be  $\sin(\theta)$ . By applying the conditioned

<sup>1</sup> This can be seen much more directly by noting that a phase shift conjugated by Hadamard operations is a rotation on the Bloch sphere.

Grovers iterate several times we can increase the rotation angle in order to improve read-out accuracy.

#### 4.4.2 Other Quantum Algorithms

We have seen that amplitude amplification and estimation can be performed on an expectation value quantum computer, allowing us to implement Grover's search algorithm.

Unfortunately, no elegant ways of implementing Shor's algorithm on an expectation value quantum computer have been found. A theoretical approach is to perform the quite involved post-processing, which would normally take place on a classical computer, within each instance, and then allowing only instances with the correct answer in the read-out [12, Chapter 10].

### 4.5 Other Proposals

The REQC proposal is not the only proposal aiming at harnessing the quantum information processing power of rare-earth-ion doped crystals. In this section we briefly review the most noteworthy alternatives, with the focus on similarities and differences with regard to REQC.

Lukin and Hemmer were the first to propose to use the dipole blockade effect to generate entanglement [44], an idea which was quickly extended to a gate operation [39]. This proposal actually differs fundamentally from what is being considered here, as the gate operation is using the off-diagonal *excitation hopping* elements of the transition matrix, which we have presently decided to ignore. Since this approach avoids populating the multiply excited states, the proposal takes advantage of the fact that the symmetric singly excited states are highly stable against decoherence [53].

The group of M. Sellars is working in directions quite similar to the REQC-proposal [42, 45], the main difference being that the group is suggesting to use a much lower value of the threshold coupling strength  $g_{\min}$  than in the REQC-proposal [54, 55]: This could lead to much improved scaling properties, but as we will see in chapter 8, it appears to be incompatible with obtaining a high gate performance when decay from the excited state is taken into account.

### 4.6 Summary

The central idea of the REQC proposal is that by parking unwanted ions in their  $|aux\rangle$  states, we can carve an ensemble of identical instances of the same quantum computer out of a rare-earth-ion doped crystal (Fig. 4.4). Although quantum algorithms have to be modified to be used on an ensemble quantum computing system, we have seen that ensemble quantum computers are essentially as strong as regular projective measure quantum computers.

At this point, the main question appears to be how to implement high fidelity gate operations for the system, which will be the topic of the following four chapters, after which we will in chapter 10 take a step back and reconsider the prospects of REQC in the light of what we have learned.



# CHAPTER 5

## Single Qubit Gates

In this chapter, we will consider in detail how single qubit gate operations for the REQC system can be implemented. The main problem we face in finding such implementations is that the operations must perform well for all the quantum computer instances in the system. This is made difficult by the small differences between the instances, such as variations in the field strength experienced by the ions, and variations in the inhomogeneous shift within a channel due to the finite channel width. In addition to inhomogeneous effects which are specific to ensemble quantum computing, we will, as in all quantum information processing, be fighting the plagues of decay and decoherence.

As stated in chapter 2, the only building blocks needed in order to implement any given quantum circuit is a sufficiently strong two-qubit gate operation, and a complete set of one qubit gates. The aim of this chapter is to establish implementations for the universal set of one qubit gates, while the implementation of a two qubit gate will be the subject of chapter 8.

### 5.1 Ion-Field Interaction

Since we have to describe the interaction of all ions in a channel with the same optical fields, we will use a basis corresponding to the free evolution of an ideal ion at the center of the channel (Fig. 5.1). In this basis, a difference  $\delta$  between the inhomogeneous shift of an ion and that of the ideal ion will lead to a free evolution as described by the free Hamiltonian<sup>1</sup>

$$H_0 = \delta |e\rangle \langle e|. \quad (5.1)$$

In the same basis, the interaction with the optical fields is described by

$$V_{\text{field}} = \gamma \sum_{i=0,1} \frac{\Omega_i(t)}{2} |i\rangle \langle e| + \text{h.c.}, \quad (5.2)$$

---

<sup>1</sup> We will in this and following chapters let  $\hbar = 1$ .

where  $\Omega_i(t)$  is the complex resonant Rabi frequency of the  $i$ .th field and  $\gamma$  is the relative field strength experienced by the ion, which is included to describe variations in the field amplitude through the crystal. We have ignored counter-rotating terms in the rotating wave approximation as well as fields addressing other transitions. Note that in the formulation used here, a detuning of the field from the channel center is described as a linear term in the phase of  $\Omega_i(t)$ .

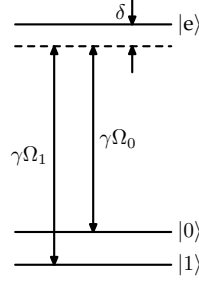


Figure 5.1: Schematic level diagram for a single ion.

The total Hamiltonian,  $H = H_0 + V_{\text{field}}$ , has two *ion-specific parameters*: the relative field strength,  $\gamma$ , and the inhomogeneous shift relative to the channel center,  $\delta$ , with values 1 and 0 respectively for an “ideal ion”. The goal of this chapter is to find *robust* gate implementations that perform well for a range of values of these parameters.

### 5.1.1 Single Field Evolution

When only the  $i$ .th field is present,  $H$  acts solely on the subspace spanned by  $|e\rangle$  and  $|i\rangle$ . In the basis  $\{|e\rangle, |i\rangle\}$ , the Hamiltonian is in this case conveniently expressed as

$$H \doteq \frac{\delta}{2} + \frac{1}{2}\Omega_i(t) \cdot \sigma \quad \text{with } \Omega_i(t) = \begin{pmatrix} \gamma \operatorname{Re}(\Omega_i(t)) \\ \gamma \operatorname{Im}(\Omega_i(t)) \\ \delta \end{pmatrix}, \quad (5.3)$$

where we note in particular that the last term is formally equivalent to a spin-1/2 particle interacting with a magnetic field parallel to the Rabi vector  $\Omega_i$  of the field [56].

**The Bloch Vector.** By making full use of the spin-1/2 analogy, we obtain a very powerful visual picture of the states and dynamics of the  $\{|e\rangle, |i\rangle\}$  system. If we identify  $|e\rangle$  with the spin-up state  $|\uparrow\rangle$  and  $|i\rangle$  with  $|\downarrow\rangle$ , the direction of the spin in the state  $|\psi\rangle = c_e |e\rangle + c_i |i\rangle$  is

$$\mathbf{S} = \langle \psi | \boldsymbol{\sigma} | \psi \rangle = \begin{pmatrix} 2 \operatorname{Re}(c_e^* c_i) \\ 2 \operatorname{Im}(c_e^* c_i) \\ |c_e|^2 - |c_i|^2 \end{pmatrix}, \quad (5.4)$$

which we refer to as the *Bloch vector* of the two level system<sup>2</sup>. We note that  $\mathbf{S}$  is a real unit vector, describing the state of the system uniquely up to a common phase factor.

**Evolution of the Bloch Vector.** We will adopt a concise notation from the NMR community, and use the notation  $\theta_\phi$  to denote a pulse of duration  $\tau = \theta/\Omega_0$ , amplitude  $\Omega_0$  and phase  $\phi$ . Since  $(\hat{\mathbf{n}} \cdot \boldsymbol{\sigma})^2 = \mathbf{1}$  for any unit vector  $\hat{\mathbf{n}}$ , it is easy to determine the evolution due to a  $\theta_\phi$  pulse by exponentiating  $-iH\tau$ :

$$\mathbf{U}(\gamma, \delta; \theta_\phi) \doteq e^{-i\delta\tau} \left[ \cos\left(\frac{|\boldsymbol{\Omega}_i|\tau}{2}\right) - i \sin\left(\frac{|\boldsymbol{\Omega}_i|\tau}{2}\right) \hat{\boldsymbol{\Omega}}_i \cdot \boldsymbol{\sigma} \right]. \quad (5.5)$$

The strength of the Bloch sphere picture is, that the effect of this complicated evolution on  $\mathbf{S}$  is simply a rotation,  $\mathcal{D}(\hat{\boldsymbol{\Omega}}_i, \tau|\boldsymbol{\Omega}_i|)$ , through an angle  $\tau|\boldsymbol{\Omega}_i|$  around the axis  $\hat{\boldsymbol{\Omega}}_i$ , as is most easily seen from the analogy to the spin system. For an ideal ion with  $\delta = 0$  and  $\gamma = 1$ , this is seen to correspond to a rotation through the angle  $\theta$  around the equatorial axis  $\hat{\mathbf{n}}(\phi) = \cos(\phi)\hat{\mathbf{x}} + \sin(\phi)\hat{\mathbf{y}}$ . Formally, this picture of the evolution rests on the fact that  $\mathcal{D} \langle \psi | \boldsymbol{\sigma} | \psi \rangle = \langle \psi | \mathcal{D}^\dagger \boldsymbol{\sigma} \mathcal{D} | \psi \rangle$ .

We note that only the second term of (5.5) influences the direction of the Bloch vector, which is not affected by a change of the common phase as caused by the first term. From a group theoretical point of view, this freedom in phase is a result of the fact that the group of unitary evolutions of a two level quantum systems,  $U(2)$ , is isomorphic with not the group of space rotations,  $SO(3)$ , but with the product  $SU(1) \otimes SO(3)$ , or more pragmatically: all possible evolutions correspond to a set of a rotation and a unimodular complex number. While the common phase is insignificant in isolated two-level systems, we will need to keep an eye on it when using the Bloch-sphere picture to describe parts of a larger system.

## 5.2 Population Swapping

We will start our survey of one qubit operations by considering the problem of transferring the population of  $|0\rangle$  to  $|e\rangle$ , an operation that will prove a central building block for many more complicated operations. In terms of rotations, we are interested in obtaining a rotation  $\mathcal{D}(\hat{\mathbf{n}}(\phi), 180^\circ)$  around any equatorial axis of the  $\{|e\rangle, |0\rangle\}$  system, and can even allow  $\phi$  to vary between ions.

### 5.2.1 Single Pulse

A straightforward way of implementing the  $180^\circ$  rotation would be a pulse of duration  $\pi/\Omega_0$  and a phase of  $270^\circ$  (to ensure real coefficients on the resulting state), which in the shorthand notation introduced in section 5.1.1 would be

<sup>2</sup> We are here only considering unitary evolution. In the general case, the Bloch vector is defined as the expectation value of  $\boldsymbol{\sigma}$ .

$180_{270}$ . This pulse will rotate the Bloch vector of an ideal ion by  $180^\circ$  around  $-\hat{y}$ , but evaluating the outcome of the operation according to (5.5), we find that to leading order in  $\delta$  and  $\gamma - 1$ , the final state is

$$\mathbf{U}(180_{270})|0\rangle = |e\rangle + \left(\frac{i}{\pi}\delta - \frac{\pi}{2}(\gamma - 1)\right)|0\rangle + \mathcal{O}(\{\delta, (\gamma - 1)\}^2). \quad (5.6)$$

In other words: the  $180_{270}$  pulse implements the state transfer for an ideal ion, but the amplitude of the ground state  $|0\rangle$  is first order in both  $\delta$  and  $\gamma - 1$ , implying that only ideal ions will be transferred efficiently.

## 5.2.2 Composite Pulses

One way of addressing this problem is to replace the simple pulse with a *composite pulse*: a pulse sequence that result in the same evolution as the simple pulse for an ideal ion, but in a more *robust* way, so that ions that are almost ideal will go through almost the same evolution [57, 58]. Composite pulses are studied intensely in the NMR community where the technological requirements for manipulating the controlling radio frequency pulses have been available for some time, see Ref. [59] for an excellent review.

To demonstrate that composing pulses can indeed improve robustness, we will consider a simple composite implementation of a  $180^\circ$  rotation. As illustrated by Fig. 5.2 the pulse sequence  $90_0 180_{90} 90_0$  is capable of transferring almost all population from the  $|0\rangle$  to the  $|e\rangle$ -state despite large differences in the relative field  $\gamma$  experienced by the ions.

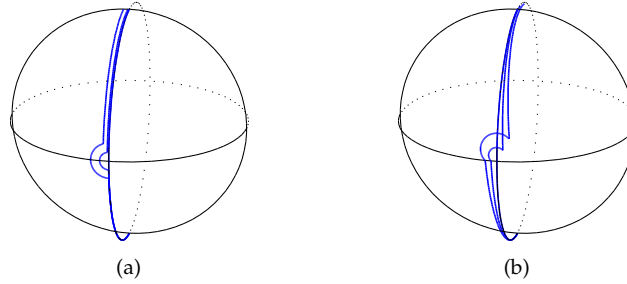


**Figure 5.2:** The evolution of the  $|0\rangle$ -state during the  $90_0 180_{90} 90_0$  pulse sequence for  $\gamma = 0.9, 0.95, 1.00$  (a) and  $\delta/\Omega_0 = 0, 0.5, 0.1$  (b). We see that the composite pulse is particularly robust with respect to variations in  $\gamma$ .

In the case of the  $90_0 180_{90} 90_0$  implementation of the  $180^\circ$  rotation, there is a clear underlying idea to the pulse sequence. In general, the ideas behind composite pulses are not so obvious, and a range of different design techniques are used to obtain composite pulses with different properties. As an example, Levitt [59] quotes the following pulse as being a  $180^\circ$  rotation which is robust with respect to both variations in field strength and detuning [60]:

$$360_0 180_{120} 180_{60} 180_{120} \quad (5.7)$$

Just how much more robust the pulse sequence (5.7) is compared to a naive  $180_0$  pulse is illustrated by Fig. 5.3.

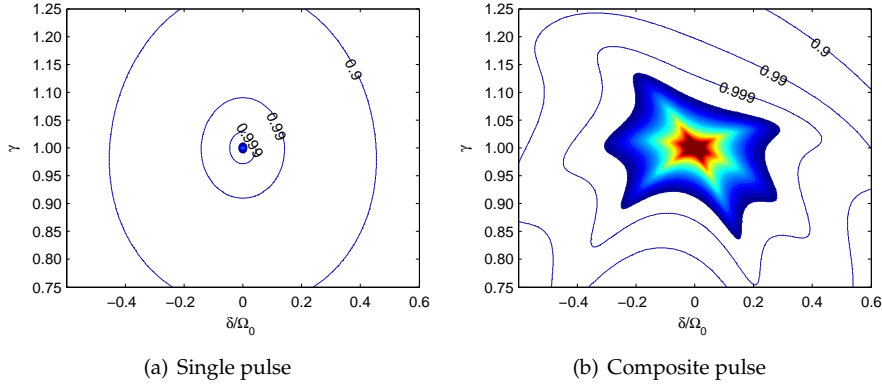


**Figure 5.3:** The performance of a naive  $180^\circ$  pulse (a) compared with that of the composite pulse given by Eq. (5.7) (b) as a function of relative field strength  $\gamma$  and inhomogeneous shift  $\delta$ . Contour line values are the overlap  $|\langle e|\psi(T)\rangle|$  between the final state and  $|e\rangle$ , the colored area corresponds to values above 0.9999. The calculation does not include decay, which would affect the implementations quite differently due to their durations of 1 and 5.5 times  $\pi/\Omega_0$  respectively. Ref. [60] also gives a sequence of 25  $180^\circ$ -pulses, which achieves an overlap greater than 0.9999 for all the parameter values of the above plots.

### 5.2.3 Smooth Fields

Figure 5.3 might be taken to indicate that good composite pulses such as (5.7) would be well suited for our purpose since an extremely high transfer rate is achieved for a large range of parameters. There is, however, an important point that we have not yet taken into account: In the REQC-system, we will be manipulating *channels*, as illustrated by Fig. 5.4. Although we have to transfer all

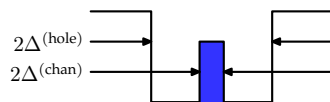


**Figure 5.4:** Schematic form of the absorption spectrum of a frequency channel.

ions in the channel, that is with  $|\delta| < \Delta^{(\text{chan})}$ , we must at the same time be careful not to disturb ions outside the hole, *i.e.* ions with  $|\delta| > \Delta^{(\text{hole})}$ . These ions do not take part in the quantum information processing, so disturbing coherences in these ions is not a problem. What is a problem, however, is accidental excitations: if an ion outside the hole is excited it will not necessarily decay to the

same ground state from which it started out, but could end up in a state interacting with the fields used to address a channel, thus disturbing the operation of the REQC-system.

Figure 5.5(a) shows the effect of the pulse (5.7) on highly detuned ions, and it is evident that the pulse sequence does indeed influence ions far from resonance. This turns out to be a general fact of discontinuous pulses [61]: For far detuned ions, the perturbation will be proportional to the Fourier component of the field corresponding to the detuning frequency. This can never fall off faster than  $1/\delta$  for discontinuous fields.

As a consequence, to employ composite square pulses, we would need to use a low field strength (and corresponding Rabi frequency) in order to not disturb ions outside the channel hole. Using a low field strength is not desirable: first of all, a low Rabi frequency implies a long gate duration, increasing the probability of decay during the gate operation. Furthermore, a lower Rabi frequency would require us to use pulses that are robust up to a larger  $\delta/\Omega_0$ -ratio, in order to robustly control a channel of a given width.

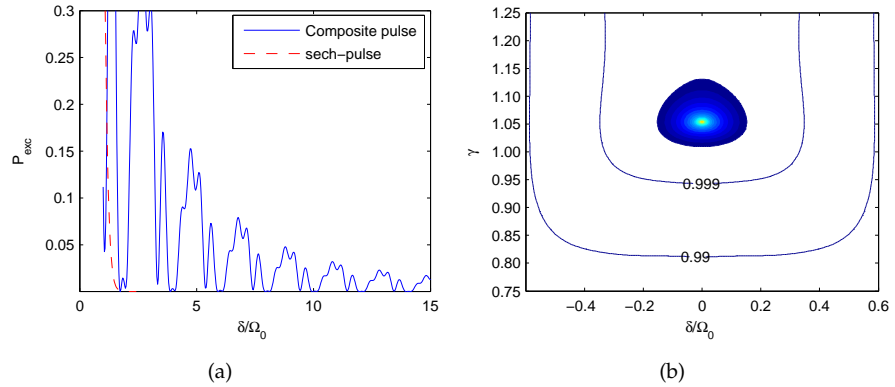


**Figure 5.5:** (a) The excitation probability  $P_{\text{exc}}$  for ions far from resonance with the driving fields after performing a  $180^\circ$  rotation by the composite pulse (5.7) (solid line) or the the sech-pulse (5.8) (dashed line). In the case of the sech-pulse,  $P_{\text{exc}}$  can only be discerned from 0 at low detunings. (b) The performance of the sech-pulse plotted with the same contour line values and color scale used for Fig. 5.3.

To avoid disturbing the neighbors of the channel, we will turn our attention to smoothly varying fields, which can potentially work selectively on a much narrower frequency range than composite square pulses. Analyzing such pulses, not to mention getting an intuitive understanding of them, is quite complicated with but a few exceptions, one being the *sech-pulse*:

$$\Omega_{\text{sech}}(t) = \Omega_0 (\text{sech}(\beta t))^{1+i\mu} = \Omega_0 \text{sech}(\beta t) e^{i\mu\beta \log(\text{sech}(\beta t))}, \quad (5.8)$$

which as illustrated by Fig. 5.5 provides a very robust implementation of the state transfer without disturbing neighboring ions [62].  $\Omega_{\text{sech}}(t)$  is plotted in

Fig. 5.6(a), where we note that the instantaneous frequency, as given by the time derivative of the phase, is swept from  $\mu\beta$  to  $-\mu\beta$  during the pulse. We can to some degree understand the action of the sech pulse as an adiabatic transfer, and the dressed state picture might be a good starting point for developing other continuously varying pulses.

Another approach to designing smooth pulses is to replace the square pulses of composite pulses with Gaussian pulses with the same area, as have been done by Roos and Mølmer with impressive results [63].

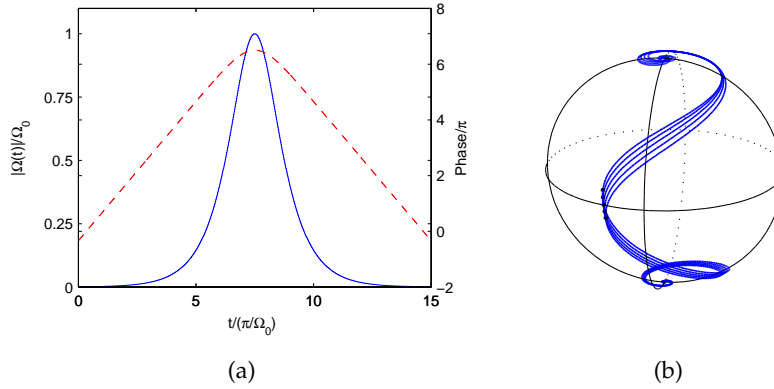


**Figure 5.6:** (a) Amplitude (solid line) and phase (dashed line) vs. time for the sech-pulse (5.8) with  $\mu = 3$  and  $\beta = 0.32$ . (b) The paths followed on the Bloch sphere for ions with detunings ranging from  $0.9\Omega_0$  to  $1.1\Omega_0$ . Points on the paths indicate the state halfway through the pulse.

## 5.3 Coherent Operations

We will now turn our attention to operations that implement a given evolution  $U_0$  for any initial state in the qubit subspace  $\mathcal{H}_Q = \text{span}(\{|0\rangle, |1\rangle\})$ .

### 5.3.1 Sequential Pulses

The operation performed on the target ion of the CNOT-gate proposed by Ohlsson *et al.* (Fig. 4.7) is an example of how coherent operations can be implemented by sequential pulses on the two transitions. To describe the sequence of pulses, or rather the corresponding rotations, in a compact form, we will use the following table:

	1	2	3	
$ 0\rangle- e\rangle$	$\hat{\mathbf{x}}_\pi$		$\hat{\mathbf{x}}_\pi$	(5.9)
$ 1\rangle- e\rangle$		$-\hat{\mathbf{x}}_\pi$		

where  $\hat{\mathbf{n}}_\theta$  is introduced as a shorthand for  $\mathcal{D}(\hat{\mathbf{n}}, \theta)$ .

It is relatively clear that this sequence of rotations exchanges the populations of  $|0\rangle$  and  $|1\rangle$ . In order to determine in detail the coherent evolution, we can for instance calculate the evolution of a perfect ion by extending the evolution operators obtained from (5.5) to the  $\{|e\rangle, |0\rangle, |1\rangle\}$  basis and multiplying:

$$\mathbf{U} = \begin{pmatrix} 0 & -i & 0 \\ -i & 0 & 0 \\ 0 & 0 & 1 \end{pmatrix} \begin{pmatrix} 0 & 0 & i \\ 0 & 1 & 0 \\ i & 0 & 0 \end{pmatrix} \begin{pmatrix} 0 & -i & 0 \\ -i & 0 & 0 \\ 0 & 0 & 1 \end{pmatrix} = \begin{pmatrix} -1 & 0 & 0 \\ 0 & 0 & 1 \\ 0 & 1 & 0 \end{pmatrix}, \quad (5.10)$$

where we see that the effect on  $\mathcal{H}_Q$  is indeed a NOT operation.

**Type A vs. Type B Pulses** The original proposal suggests to implement the rotations  $\mathcal{D}(\hat{n}(\phi), \theta)$  of (5.9) by the corresponding hard pulses  $\theta_\phi$ . This implementation will obviously not be any more robust than the simple pulses themselves.

Some care should be taken, if we use the  $180^\circ$  pulses of section 5.2 to implement the rotations: In the previous section, we only considered population swapping operations, mapping  $|0\rangle$  to  $|e\rangle$  by a  $180^\circ$  rotation about any axis. We will refer to such pulses that only work for some initial states as *type B* pulses.

It would appear that in order to implement (5.9), we need all instances to be rotated around the specified axes. Pulses implementing the same rotation for all parameter values are known as *type A* pulses, and it is perhaps no surprise that type A pulses are much harder to come by than type B pulses: As an example, the comprehensive listing of  $180^\circ$  pulses by Levitt [59] does not list any type A pulses which are robust with respect to both detuning and field strength.

In the case of the NOT operation (5.9), a closer analysis actually shows that we can get by with a type B  $180^\circ$  rotation such as the sech-pulse, if only we use the same pulse for all three rotations, or more precisely: if we implement each rotation  $\mathcal{D}(\hat{n}(\phi'), \pi)$  by the pulse  $\exp(i\phi')\Omega_s(t)$ , where  $\Omega_s(t)$  is any  $180^\circ$  template pulse. The reason is that  $\Omega_s(t)$  being a  $180^\circ$  pulse implies that it must implement a rotation  $\mathcal{D}(\hat{n}(\phi(\delta, \gamma)), \pi)$  around a consistent axis for each ion. Since  $\exp(i\phi')\Omega_s(t)$  will necessarily implement a rotation about the axis  $\hat{n}(\phi(\delta, \gamma) + \phi')$ , we see that for each ion the difference between the rotation axes, will be correct. As this distance is the only parameters that enter the final form of (5.10), we see that (5.9) can indeed be implemented by type B rotations. Because of the symmetry of the sequence, the operation will not be affected by phase errors due to the first term of the evolution operator (5.5).

### 5.3.2 Parallel Fields

The only reason we can use type B pulses to implement the NOT-operation (5.9), is that the NOT-operation corresponds to a  $180^\circ$  rotation in  $\mathcal{H}_Q$ , so that we could use the same pulse for all three rotations.

One way to avoid the need for type A pulses in implementing a more general class of rotations of  $\mathcal{H}_Q$ , was suggested by Roos and Mølmer [63], and is based on the notion of *bright states* when two coherent fields interact with a three-level

system. If we restrict ourselves to *parallel fields*, i.e. time dependent complex Rabi frequencies of the form  $\Omega_i(t) = c_i \Omega(t)$ , where we will require  $|c_0|^2 + |c_1|^2 = 1$ , the field-ion interaction takes the form

$$V_{\text{field}} = \frac{1}{2} \Omega(t) (c_0 |0\rangle + c_1 |1\rangle) \langle e| + \text{h.c.} \quad (5.11)$$

This has the form of a single field of Rabi frequency  $\Omega(t)$  addressing a transition between  $|e\rangle$  and the superposition state  $|\psi_+\rangle = c_0 |0\rangle + c_1 |1\rangle$ , referred to as the bright state of the system. The component of  $\mathcal{H}_Q$  orthogonal to  $|\psi_+\rangle$ , dubbed the *dark state*, does not interact with the field at all. To address the dark state  $|\psi_-\rangle$  we can swap the field amplitudes and change the relative phase by  $\pi$  to interchange the dark and bright states.

The key idea of the parallel fields proposal, is that any rotation in  $\mathcal{H}_Q$  can be implemented as a phase shift on a suitably chosen superposition state  $|\psi_+\rangle$ . To see this, we need only note that

$$e^{-i \frac{\hat{n} \cdot \sigma}{2} \theta} = e^{-i\theta/2} |\hat{n}, +\rangle \langle \hat{n}, +| + e^{i\theta/2} |\hat{n}, -\rangle \langle \hat{n}, -| \quad (5.12a)$$

$$= e^{-i\theta/2} [\mathbf{1} + (e^{i\theta} - 1) |\hat{n}, -\rangle \langle \hat{n}, -|], \quad (5.12b)$$

where  $|\hat{n}, \pm\rangle$  are the eigenstates of  $\hat{n} \cdot \sigma$  corresponding to eigenvalues  $\pm 1$ . This implies that to rotate the  $\{|0\rangle, |1\rangle\}$  system by an angle  $\theta$  around an axis  $\hat{n}$ , we can choose field amplitudes  $c_{\{0,1\}}$  so that the bright state  $|\psi_+\rangle$ , coincides with the negative eigenstate of  $\hat{n} \cdot \sigma$ , and shift the phase of this state by  $\theta$  by manipulating the common amplitude  $\Omega(t)$  as if dealing with a two-level system.

Compared to the sequential pulse approach, the advantage is that the phase shift operation is a type B operation: we know the initial state, making a robust implementation much more feasible. Coherent control of rare-earth ions by multiple optical fields has been performed experimentally, see e.g. Ref. [64]. The fact that the fields are parallel could possibly serve to simplify the experimental implementation, since the modulator implementing  $\Omega(t)$  could be placed before the two fields were separated and frequency-shifted.

## 5.4 Phase Shift Operations

We will now consider possible implementations of a phase shift operation  $|0\rangle \mapsto e^{i\theta} |0\rangle$ , which by means of parallel fields could be used to implement a general rotation in the qubit space. As the phase shift is a type B operation, obtaining a robust implementation should be simpler than for a direct coherent manipulation of the qubit space.

To express the phase shift operation in terms of rotations, we start by noting that the rotation must necessarily be around the  $\hat{z}$ -axis of the Bloch sphere of the  $\{|0\rangle, |e\rangle\}$  system: The state  $|0\rangle$ , corresponding to the south pole, must be mapped onto itself and so must be a pole of the rotation. Comparing with (5.3), we find that a phase shift of  $\theta$  on the  $|0\rangle$  state, corresponds to the rotation  $\mathcal{D}(\hat{z}, 2\theta)$ . An important point to note is that the two identical (as  $SO(3)$ )

elements) rotations  $\mathcal{D}(\hat{z}, 2\theta)$  and  $\mathcal{D}(\hat{z}, 2\theta + 2\pi)$  result in two different phase factors:  $\exp(i\theta)$  and  $-\exp(i\theta)$ . As can be seen from (5.3), this is quite general: each element in  $SO(3)$ , as described by a rotation axis and an angle, correspond to two different elements of  $SU(2)$ . In particular, we note that a phase of  $\pi$ , corresponding to a phase factor of  $-1$ , corresponds to a rotation by  $2\pi$ . Since any point on the Bloch sphere is a pole for any  $2\pi$  rotation, this invalidates our initial argument that we must use  $\hat{z}$  rotations to implement phase shifts, for the case of  $\pi$  phase shifts.

### 5.4.1 Phase Shift by Population Swapping

As we have seen, optical fields rotate an (ideal) ion about equatorial axes. In terms of such rotations a phase shift of  $\theta$ , corresponding to the rotation  $\mathcal{D}(\hat{z}, 2\theta)$ , can be implemented by two  $\pi$  rotations as

$$\frac{1}{|0\rangle\langle e|} \frac{2}{-\hat{x}_\pi \hat{n}(\theta)_\pi} \quad (5.13)$$

To convince yourself of this without resorting to (5.3), consider the following: Starting from the south pole, walk straight ahead until reaching the north pole. Now sidestep left back to the south pole (this would admittedly take a while), and you find yourself facing the opposite direction of when you started, although the difference between the rotation axes was only  $\pi/2$ .

Again, it is important to note that only the difference in rotation axis is of importance in this sequence, since this implies that the rotations can be implemented by type B pulses. The principal weakness of phase shift operations based on state transfer appears to be that the integrated population of the excited state will be quite significant in most cases, implying a relatively high probability of decay from the excited state.

### 5.4.2 Phase Compensating Pulses

So far, we have talked of pulses in terms of rotations, ignoring the common phase described by the first term of  $H$  as given by (5.3). While this term was canceled out by symmetry in the NOT operation (5.9), it does in general warrant some caution: If we try implementing a parallel field gate operation by only operating on the  $|e\rangle$  and  $|0\rangle$  states we find that the obtained phase shift  $\phi(\delta)$  of the population in the  $|0\rangle$  state, will have a strong first order dependence on the inhomogeneous shift  $\delta$  of the excited state  $|e\rangle$ . In fact, we show below that if the pulse leaves no population in the excited state, we have

$$\frac{\partial \phi}{\partial \delta} = \int_0^T P_{\text{exc}}(t) dt, \quad (5.14)$$

where  $P_{\text{exc}}$  is the population in  $|e\rangle$ , so that  $\phi(\delta)$  will be a monotonous function of  $\delta$ . This linear term implies that a phase shift implemented by (5.13) can never

be robust: Consider two ions with inhomogeneous shift  $\delta^{(1)}$  and  $\delta^{(2)}$ . The above result implies that the difference between the phase obtained by these ions will always differ by  $(\delta^{(2)} - \delta^{(1)}) \int P_{\text{exc}} dt$ .

Fortunately, the ill-effects of the phase shift are easily removed by turning the erroneous phase into a common phase by means of *phase compensating pulses* [II]. One approach to phase compensation is to use pulses that have no effect on an ideal ion, but merely ensure that the phase  $\phi(\delta)$  becomes a global phase. For example, a phase compensated version of the sequence (5.13), would be

$$\begin{array}{cccc} & 1 & 2 & 3 & 4 \\ \hline |0\rangle\text{-}|e\rangle & -\hat{x}_\pi & \hat{n}(\theta)_\pi & & \\ |1\rangle\text{-}|e\rangle & & & -\hat{x}_\pi & \hat{x}_\pi \end{array} \quad (5.15)$$

**Phase bookkeeping.** The analysis the phase properties of of pulse sequences such as (5.15) is most easily done by tracking the phase of a detuned ion with respect to that of an ideal ion for each initial state.

For the phase compensating pulse scheme (5.15), this can be achieved by a table such as the following

$$\begin{array}{cccccc} & 1 & 2 & 3 & 4 & \Sigma \\ \hline |0\rangle & \phi(\delta) & \phi(\delta) & & & 2\phi(\delta) \\ |1\rangle & & & \phi(\delta) & \phi(\delta) & 2\phi(\delta) \end{array} \quad (5.16)$$

where we have labeled the populations by the qubit state it starts out in, the numbers in the first row indicate pulse numbers according to (5.15), and the table entries are the phase difference between an ideal ion and a detuned ion accumulated during that subinterval. Note that for the errors to add to a global phase, we assume  $\phi(\delta)$ , to be identical for the all of the four two-pulse pairs: this can be achieved by implementing all  $\pi$  rotations in the same way.

**Proof of (5.14)** To derive (5.14), we consider the difference in evolution for two ions with opposite detunings:  $\delta^{(1)} = -\delta^{(2)} = \delta$ . Expanding the state on  $|0\rangle$  and  $|e\rangle$  as  $c_0^{(i)} |0\rangle + c_e^{(i)} |e\rangle$ , the Schrödinger equation takes the form

$$i\dot{c}_e^{(i)} = \delta^{(i)} c_e^{(i)} + \frac{\bar{\Omega}}{2} c_0^{(i)} \quad (5.17a)$$

$$i\dot{c}_0^{(i)} = \frac{\Omega}{2} c_0^{(i)}, \quad (5.17b)$$

where  $\bar{\cdot}$  denotes complex conjugate. To compare the resulting phases, we consider  $c_0^{(1)} \bar{c}_0^{(2)}$  which is equal to  $\exp(i(\phi(\delta) - \phi(-\delta)))$  in the case of perfect transfer. From (5.17) we find

$$\frac{\partial}{\partial t} c_0^{(1)} \bar{c}_0^{(2)} = -2i\delta c_e^{(1)} \bar{c}_e^{(2)} - \delta \frac{\partial}{\partial t} c_e^{(1)} \bar{c}_e^{(2)},$$

so that after integrating, we have (assuming  $c_0^{(i)} = 1$ )

$$c_0^{(1)} \bar{c}_0^{(2)} \Big|_T = -2i\delta \int_0^T c_e^{(1)} \bar{c}_e^{(2)} dt - \delta c_e^{(1)} \bar{c}_e^{(2)} \Big|_T. \quad (5.18)$$

If we have perfect transfer, the last term vanishes, and taking the limit of  $\delta \rightarrow 0$  we obtain (5.14), which is valid at any  $\delta$  where we get perfect transfer, since change of energy reference would just correspond to a linear phase in the field.

### 5.4.3 Direct Phase Shift Operations

It should be possible to design robust phase shift implementations that do not rely on prolonged population of the excited state. One approach is to note that up to a common phase, mapping  $|0\rangle$  to  $e^{i\theta} |0\rangle$  is equivalent to the mapping  $|0\rangle \mapsto e^{i\theta/2} |0\rangle$ ,  $|1\rangle \mapsto e^{-i\theta/2} |1\rangle$ . In terms of rotations on the optical transitions, the latter form translates into a symmetrical set of rotations:

$$\begin{array}{c|cc} & 1 & 2 \\ \hline |0\rangle-|e\rangle & \hat{z}_\theta & \\ |1\rangle-|e\rangle & & -\hat{z}_\theta \end{array} \quad (5.19)$$

The advantage of this symmetrical pulse sequence is that given an implementation of the  $\hat{z}_\theta$  rotation suitable for rotation 1 we can obtain an associated implementation of  $-\hat{z}_\theta$  to use for replacing rotation 2, while obtaining the same integrated population of the  $|e\rangle$ -state, and consequently compensating for phase errors: If  $\Omega^{(z)}(t)$  implements the rotation  $\hat{z}_\theta$  for an ion with detuning  $\delta$ , we find that  $\bar{\Omega}^{(z)}$  implements  $\hat{z}_{-\theta}$  for an ion with detuning  $-\delta$ . To see this, we note that mapping  $\Omega$  to  $\bar{\Omega}$  and  $\delta$  to  $-\delta$  corresponds to a parity mapping on the instantaneous rotation axis  $\Omega \mapsto -\Omega$  (5.3). Since the dynamics are completely determined by  $\Omega$ , the resulting operation must also be transformed by the parity mapping. If additionally  $\Omega^{(z)}(t)$  is time symmetric, we see that the  $\int P_{\text{exc}} dt$  will be independent of the sign of  $\delta$ , so that  $\Omega_z$  will indeed implement a phase compensated phase operation.

We have not considered the problem of constructing phase shift implementations in much detail, but the concept of *geometric phase* [65–68], which has been employed in quantum gate design, [69], appears to be useful for designing such gates, even though the initially much heralded intrinsic robustness of geometric gates seems to be questionable [70, 71]. In particular, the double state transfer approach could be considered as a geometrical gate, and the analysis of Nazir *et al.* [70] applies to this implementation also.

As a simple example of a non-exciting phase gate we consider the following pulse sequence

$$\eta_{(\phi+\pi/2)} \lambda_0 \eta_{-(\phi+\pi/2)} \quad (5.20)$$

which for  $\lambda = 2 \tan^{-1}(\tan(\eta) \sin(\phi))$  performs a  $\hat{z}$ -rotation resulting in a phase of  $\theta = \tan^{-1}(\sec(\eta) \tan(\phi)) - \phi$ , as can be seen from (5.5). Since the phase is

additive, several such pulses could be employed to achieve a certain phase, as illustrated in Fig. 5.7, and it appears that such composite loops could lead to some degree of robustness. To avoid neighbor disturbance it would be beneficial to replace the pulses with a smooth pulse causing a similar evolution.

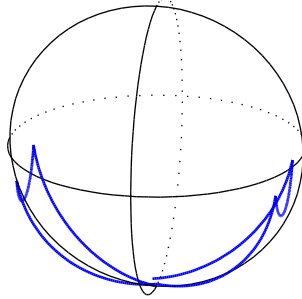


**Figure 5.7:** A hard pulse phase gate implementation based on the pulse sequence (5.20) with  $\phi = \pi/8$  and  $\eta = \sec^{-1}(\tan(3\pi/8)/\tan(\pi/8))$ , leading to a phase of  $45^\circ$  per loop. Figure shows the evolution of  $|0\rangle$  on the Bloch sphere during two loops, where the phases of the pulses implementing the second loop have been collectively shifted by  $\pi$ .

#### 5.4.4 Other Gate Implementations

There are many alternatives to the gate implementation considered so far.

**Non-parallel fields.** An additional degree of freedom can be had by dropping the constraint that  $\Omega_0$  and  $\Omega_1$  should be parallel. From an experimental point of view, this would require the use of two modulators. Aside from the higher cost, this could be less difficult than frequency shifting part of the modulated signal, as would be required by our suggestion for a parallel field setup using only a single modulator.

The main problem with non-parallel fields implementations is the design, as three level quantum systems are hard to visualize. We present a way around this problem in chapter 6.

**Multiple Excited States.** Our model ion (Fig. 5.1) has only one excited state  $|e\rangle$ , although in most cases there will be other hyperfine levels nearby. By making use of these, we can implement a gate operation in a way similar to (5.9), without the need for type A operations as illustrated in Fig. 5.8 [72]. In the light of the observations of section 5.3 that type A operations are not necessary to implement the NOT operation (5.9), this approach has lost some of its appeal.

The main problem with making use of additional excited states is that it further restricts the maximum hole width (Fig. 4.1(b)) for a given physical system.

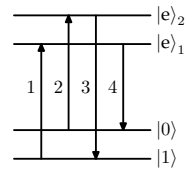


**Figure 5.8:** Sequential pulse NOT-gate implementation without type A pulses.

## 5.5 Summary

In summary, we have seen that it is possible to implement high fidelity one qubit gates in the REQC system.

More precisely, we have established that by suitable phase compensation (5.19), any  $180^\circ$  pulse can be used to implement a universal set of one qubit rotations through the use of parallel fields. Furthermore, we have found that we can achieve very robust  $180^\circ$  rotations by means of smooth pulses, such as the sech-pulse (5.8), without disturbing ions outside the hole.

We have not considered quantitatively the influence of decay on gate performance in this chapter, but intuitively, some of the gate implementations will be severely affected by decay due to prolonged population of the  $|e\rangle$ -state. As a way around this, we have suggested looking for dedicated low excitation phase shift implementations such as (5.20). We will consider this approach in more detail in chapter 7.

# CHAPTER 6

## Automated Design of Robust Gate Implementations

In this chapter we describe a numerical method for finding time dependent *controls*, such as phase and amplitude of an optical field, that cause a desired evolution of a quantum system in a way that the resulting evolution of the system is insensitive to variations in certain *system parameters* e.g. inhomogeneous shifts or local field strengths. We have reason to believe that such a method could lead to useful gate operations, as similar methods are being successfully applied to related problems in NMR pulse design and for pulse shaping in femtosecond spectroscopy [73, 74].

The central idea of the approach presented here is that robustness can be achieved by numerically optimizing the worst case performance over a sample set of system parameter values: One might hope, that if sufficient smoothness requirements are placed on the controls, this optimization will lead to a result that is close to the result which would have been found by optimizing over all system parameter values of interest.

Since evaluating the performance of a set of controls is simply a matter of propagating the Schrödinger equation for each set of system parameter values, one could leave the optimization to a simple minimization algorithm without taking gradients into account. Although this approach has been applied to similar problems [75], we believe that the space of possible controls in our case is far too large for such an unstructured approach to be computationally viable. To obtain the gradient information needed to efficiently optimize the performance of a gate implementation, we will turn our attention to the results of optimal control theory.

The present chapter is devoted to describing the technical details of applying optimal control theory to the construction of robust pulses by sampling. We will describe the structure of the chapter in more detail at the end of the first

section, after having introduced some notation and central concepts. The results of applying the method to the problem at hand will, however, be the topic of the next chapter.

## 6.1 Introduction to Optimal Control Theory

We consider a collection of quantum system, each characterized by a set of *system parameter values*  $\zeta$ , and all governed by a common vector of time-dependent controls  $\varepsilon(t)$ , e.g. the phase and amplitude of one or more optical or radio frequency electric fields. For notational simplicity, we will describe the evolution of the systems by a generic first order differential equation

$$\dot{\mathbf{x}}(t) = \mathbf{f}(\zeta; \mathbf{x}(t), \varepsilon(t)), \quad \mathbf{x}(0) = \mathbf{x}_0(\zeta). \quad (6.1)$$

In the simplest case of interest here, the *state vector*  $\mathbf{x}(t)$  would be the quantum state vector, and the differential equation the Schrödinger equation. Besides hiding the details of the Schrödinger equation, this more general formulation has the advantage that we can replace the quantum state vector with an evolution operator, or even a superoperator describing the evolution of the density matrix according to the full master equation of the problem.

### 6.1.1 The Objective Functional

Due to different system parameter values the systems will evolve differently. We will quantify how well a choice of controls  $\varepsilon$  performs for a given set of system parameter values  $\zeta$  by the *single system objective functional*  $J(\zeta, \varepsilon)$ , for which we by convention take smaller values to indicate better performance. In order to be able to calculate the gradient of the objective, we will restrict our attention to single system objective functionals of the form,

$$J(\zeta, \varepsilon) = \phi(\zeta, \mathbf{x}(T)) + \int_0^T l(\zeta, \mathbf{x}(t), \varepsilon(t)) dt, \quad (6.2)$$

which is seen to be quite general: The real-valued function  $\phi(\zeta, \mathbf{x}(T))$  quantifies how close the final state  $\mathbf{x}(T)$  is to our goal, while the real-valued function  $l(\zeta, \mathbf{x}(t), \varepsilon(t))$ , referred to as the *penalty function*, can be chosen to discourage the use of certain states or control values.

In terms of the single system objective functional, robustness can be expressed in a conceptually simple way in terms of the worst case performance over a range  $X$  of system parameter values:

$$J_X(\varepsilon) = \max_{\zeta \in X} J(\zeta, \varepsilon), \quad (6.3)$$

so that finding the optimal solution is simply a matter of finding the controls  $\varepsilon$  from a set of allowed controls  $M$  that minimizes  $J_X(\varepsilon)$ . In many cases,  $X$  will

cover a continuous range of single system parameters, e.g. all inhomogeneous shifts smaller than some threshold. In order to be able to evaluate the objective functional numerically, we will, however, replace  $X$  with a discrete subset  $X' = \{\zeta_i\}$  of *samples*, so that  $J_{X'}$  can be evaluated by simply calculating  $J(\zeta_i, \varepsilon)$  for each sample  $\zeta_i$ .

### 6.1.2 Optimal Control Software

As formulated above, constructing robust gate implementations takes the form of an *optimal control problem* [76, 77].

A number of software packages for solving optimal control problems arising in many engineering disciplines are available. We have considered SOCS, a commercial (Boeing) product developed by Betts [78], Miser3, developed at the University of Western Australia [79, 80], and RIOTS, which uses the sequential quadratic programming library FSQP internally for optimization [76].

These optimal control packages all work by calculating the gradient of the objective functional, by a method we will spend the rest of this chapter developing, and feeding this information to a specialized minimization algorithm. By integrating the two parts of this process (evaluation of  $J$  and  $\partial J/\partial \varepsilon$  on one side and the optimization algorithm on the other), several advantages are achieved: Firstly, both the differential equation solver and the optimization algorithm can be optimized since the accuracy requirements and structure of the input is known. Secondly, the parametrization of the controls can be made adaptive, so that for instance the number of time steps can be increased at points of high activity.

Unfortunately, none of the programs considered appear to fit our needs. In particular, the propagation methods used are not accurate enough to propagate the Schrödinger equation consistently.

### 6.1.3 Optimal Control as a Constrained Optimization Problem

Instead of using existing optimal control software, we will construct our own from independent building blocks. The drawback of this approach is that we do not get the advantages of using optimized parts.

The first step is to choose a suitable parametrization of the time dependent controls  $\varepsilon(t)$  in terms of a vector  $\mathbf{u}$  of real numbers, allowing us to consider  $J(\zeta, \varepsilon(\mathbf{u}))$  as a function of  $\mathbf{u}$ . As mentioned above, it is possible to numerically calculate the dependency of  $J$  on the controls at any given time. This information allows us to determine the gradient of  $J(\zeta, \varepsilon(\mathbf{u}))$  with respect to  $\mathbf{u}$ . In terms of  $\mathbf{u}$ , minimizing  $J_{X'}$  takes the form of a so-called *minimax* problem, as we are interested in finding

$$\min_{\mathbf{u} \in M} \max_{\zeta \in X'} J(\zeta, \varepsilon(\mathbf{u})), \quad (6.4)$$

where  $M$  is the set of allowed values of  $\mathbf{u}$ , which will in usually be defined through a number of constraints.

### 6.1.4 Overview of the Chapter.

The remainder of the chapter is devoted to calculating the gradient of the single sample objective functional  $J(\zeta, \varepsilon)$  for a number of specific problems of interest. We start in section 6.2 by calculating the gradient of  $J$  in the general form (6.2), first for the simplest case of a real state vector, then for the notationally more complicated case of a complex state vector. In the next section, we describe the relation of the optimization method used here, to the direct optimization methods which are widely used for NMR pulse design.

In sections 6.4 and 6.5 we will consider the specifics of applying the results to single state and multi state quantum dynamics. This will require us to discuss control parametrization and fidelity measures for quantum evolution.

## 6.2 Calculating the Objective Gradient

We will now see how the control dependency of the single system objective functionals may be calculated by methods from optimal control theory.

For simplicity, we will first calculate  $\partial J/\partial \mathbf{x}$  for the case of the state vector  $\mathbf{x}$  residing in a real vector space, even though this case will not be relevant for actual calculations. We will then proceed to consider the case of the evolution of a single, and subsequently multiple, pure states under the Schrödinger equation. For notational simplicity, we will omit the system parameter values  $\zeta$  in this section, as we will only be considering the evolution of a single system.

### 6.2.1 Real State Vector

The central idea for calculating  $\partial J/\partial \varepsilon$  is due to Lagrange: we introduce the *adjoint state*  $\boldsymbol{\lambda}(t)$ , which is in effect a continuous set of Lagrange multipliers, and the *modified objective functional*:

$$J'(\varepsilon) = J(\varepsilon) - \int_0^T \boldsymbol{\lambda}(t) \cdot (\dot{\mathbf{x}}(t) - \mathbf{f}(\mathbf{x}(t), \varepsilon(t))) dt, \quad (6.5)$$

thus incorporating the dynamical equation (6.1) as a constraint. Introducing the *Hamiltonian* of the optimal control problem

$$h = l(\mathbf{x}, \varepsilon) + \boldsymbol{\lambda} \cdot \mathbf{f}(\mathbf{x}, \varepsilon), \quad (6.6)$$

not to be confused with the Hamiltonian of an underlying physical system, we rewrite  $J'$  (after a partial integration) as

$$J'(u) = \phi(\mathbf{x}(T)) - \boldsymbol{\lambda} \cdot \mathbf{x}|_0^T + \int_0^T (h(\mathbf{x}, \boldsymbol{\lambda}, \varepsilon) + \dot{\boldsymbol{\lambda}} \cdot \mathbf{x}) dt. \quad (6.7)$$

The lowest order variation in  $J'$  as a result of a variation  $\delta\varepsilon$  in  $\varepsilon$  and the resulting change  $\delta x$  in  $x$  is seen to be

$$dJ' = \left[ \frac{\partial \phi}{\partial \mathbf{x}} - \boldsymbol{\lambda} \right] \Big|_T \cdot \delta \mathbf{x}(T) + \int_0^T \left( \left[ \frac{\partial h}{\partial \mathbf{x}} + \dot{\boldsymbol{\lambda}} \right] \cdot \delta \mathbf{x} + \frac{\partial h}{\partial \boldsymbol{\varepsilon}} \cdot \delta \boldsymbol{\varepsilon} \right) dt, \quad (6.8)$$

so that requiring  $\boldsymbol{\lambda}$  to fulfill the *adjoint equations*

$$\dot{\boldsymbol{\lambda}} = -\frac{\partial h}{\partial \mathbf{x}}, \text{ and } \boldsymbol{\lambda}(T) = \frac{\partial \phi}{\partial \mathbf{x}} \Big|_T, \quad (6.9)$$

implies that the differential of the modified objective takes the simple form

$$\boxed{dJ' = \int_0^T \frac{\partial h}{\partial \boldsymbol{\varepsilon}} \cdot \delta \boldsymbol{\varepsilon} dt,} \quad (6.10)$$

since the terms in square brackets in (6.8) vanish.

Eq. (6.10) is the most important result of this chapter: given a dynamical system (6.1) we are now able to calculate the partial derivative of an objective functional in the form (6.2) with respect to the controls at any given time. To do this, we first propagate the initial state vector  $\mathbf{x}_0$  to obtain  $\mathbf{x}(t)$  for all  $t$ . Based on  $\mathbf{x}(T)$  and the form of the objective functional, we now determine the boundary value for the adjoint state  $\boldsymbol{\lambda}$  at  $t = T$ . This boundary value is then back-propagated according to the adjoint equation (6.9) to obtain  $\boldsymbol{\lambda}(t)$  at all times. Having computed the  $\mathbf{x}(t)$  and  $\boldsymbol{\lambda}(t)$  for all  $t$ , (6.10) allows us to calculate the first order change  $dJ$  in the objective functional due to any variation  $\delta\varepsilon$  in the controls. The role of the adjoint state and the adjoint equations is often described as back-propagating the errors in achieving the desired final state.

We should note at this point, that variations in the process duration,  $T$ , can easily be taken into the differential. We will not consider this further, since for our purposes using larger than optimal value of  $T$  will not result in any performance penalties: If an optimal pulse of shorter duration than  $T$  is available, the optimization procedure is free to park the population in the decay and decoherence free qubit levels while waiting for the time to run out. In this way, a predetermined value of  $T$  merely serves as a limit on the pulse duration.

## 6.2.2 Complex State Vector

In most quantum dynamic setting we will be interested in using a complex state vector  $\mathbf{x} \in \mathbb{C}^n$ . Since there is a trivial isomorphism between the vector spaces  $\mathbb{C}^n$  and  $\mathbb{R}^{2n}$  given by

$$\vec{\mathbf{u}} = \begin{pmatrix} \text{Re}(\mathbf{u}) \\ \text{Im}(\mathbf{u}) \end{pmatrix}, \quad (6.11)$$

we could say that the result of the previous section trivially generalizes. In practice however, it proves beneficial to add some additional notation, although the

approach based on dual vectors to be introduced here is perhaps on the abstract side. None the less, besides being free of mumbling, it has proven to be efficient to work with.

We will use the notation  $\overrightarrow{v}$  to denote a vector in the real state vector space  $V$ . The *dual space* of  $V$ , which we will denote  $V^*$  is the real vector space of all linear mappings from  $V$  to  $\mathbb{R}$ . We will assume a 1 : 1 mapping between  $V$  and  $V^*$ , so that we can write  $\overleftarrow{v}$  for the uniquely defined dual vector to  $\overrightarrow{v}$ .

As an example, a good mapping between  $V$  and  $V^*$  in the case of an underlying complex vector space turns out to be:

$$\overleftarrow{u} \overrightarrow{v} \equiv 2 \overrightarrow{u} \cdot \overrightarrow{v}, \quad (6.12)$$

since this leads to

$$\overleftarrow{u} \overrightarrow{v} \equiv 2 \begin{pmatrix} \text{Re}(\mathbf{u}) \\ \text{Im}(\mathbf{u}) \end{pmatrix} \cdot \begin{pmatrix} \text{Re}(\mathbf{v}) \\ \text{Im}(\mathbf{v}) \end{pmatrix} = \mathbf{u}^\dagger \mathbf{v} + \text{c.c.}, \quad (6.13)$$

which is a convenient form to work with.

When we consider a real function  $h$  of complex variables, calculating  $\partial h / \partial \overrightarrow{z}$  in terms of real and imaginary parts turns out to be cumbersome in most cases. The standard solution to this is to consider  $z$  and  $z^\dagger$  to be independent with respect to partial differentiation, so that we may write

$$dh = \frac{\partial h}{\partial z} dz + \frac{\partial h}{\partial z^\dagger} dz^\dagger \quad (6.14)$$

$$= 2 \frac{\overrightarrow{\partial h}}{\partial \overrightarrow{z}} \cdot d\overrightarrow{z} = \frac{\overleftarrow{\partial h}}{\partial \overrightarrow{z}} d\overrightarrow{z}, \quad (6.15)$$

implying that

$$\frac{\partial h}{\partial \overrightarrow{z}} = \frac{\overleftarrow{\partial h}}{\partial \overrightarrow{z}} \quad (6.16)$$

With these observations in mind and the optimal control Hamiltonian (6.6) generalized as  $h = l(x, u) + \overleftarrow{\lambda} \overrightarrow{f}(x, u)$  we have

$$dJ' = \left( \frac{\overleftarrow{\partial \phi}}{\partial \overrightarrow{x}} - \overleftarrow{\lambda} \right) \Big|_T \delta \overrightarrow{x}(T) + \int_0^T \left( \left[ \frac{\overleftarrow{\partial h}}{\partial \overrightarrow{x}} + \overleftarrow{\dot{\lambda}} \right] \delta \overrightarrow{x} + \frac{\partial h}{\partial \overrightarrow{\varepsilon}} \cdot \delta \overrightarrow{\varepsilon} \right) dt, \quad (6.17)$$

so that the adjoint equations take the form

$$\dot{\overleftarrow{\lambda}} = - \frac{\partial h}{\partial \overrightarrow{x}}, \quad \overleftarrow{\lambda}(T) = \frac{\partial \phi}{\partial \overrightarrow{x}} \Big|_T, \quad (6.18)$$

and the differential of  $J'$  is again found to be given by (6.10).

## 6.3 Direct Minimization Methods

Instead of feeding the gradient information obtained through (6.10) to an optimization algorithm as we are planning to do, we could try to solve the minimum condition  $dJ = 0$  directly, an approach known as *direct minimization*. Solving the minimum condition is significantly simplified if a penalty function proportional to  $\varepsilon^2$  is introduced [73, 81–84],  $h = \alpha\varepsilon^2 + h_0$ , so that the extremum condition according to (6.10) reads,

$$\varepsilon(t) = -\frac{1}{2\alpha} \frac{\partial h_0}{\partial \varepsilon}, \quad (6.19)$$

which may be used as an iterative formula for calculating  $\varepsilon$ . Variations over this iterative approach give rise to the Krotov [85] and Zhu-Rabitz [82, 83] algorithms which have shown to be stable and have excellent convergence properties. These methods have been successfully applied to optimal control of unitary transformations for one set of parameters by Palao *et al.* [84, 86]. A unifying view of the direct methods can be found in Ref. [87].

The main drawback of direct optimization methods is that they require the penalty function to depend on the controls, and that they do not cooperate well with bounds on the controls. Using bounds rather than penalty functions allows us to more accurately model the fact that the experimental limitations most often only distinguish between possible and impossible controls: no possible controls are significantly harder than others.

In addition, for the direct approach to be applied to our minimax problem, it appears that it would be necessary to replace  $J_{X'}(\varepsilon)$  with some smooth function of the various  $J(\zeta_i, \varepsilon)$ , such as

$$J_{X'}(\varepsilon) \approx \sqrt[k]{\sum_i J^k(\zeta_i, \varepsilon)}, \quad (6.20)$$

for some large integer  $k$ , in effect a smooth approximation of the maximum function.

It should be noted that the existence of a non-vanishing adjoint state fulfilling the adjoint equations so that  $dJ = 0$  by (6.10) in the case of a global extrema was only established in 1962 by Pontryagin and co-workers [88]. In general, the technicalities of optimal control theory are quite challenging: even Lagrange got it wrong. For a very readable introduction to the mathematical theory of optimal control we refer to the excellent book by Young [89, Vol. II, chap. 2].

## 6.4 Application to Single State Quantum Dynamics

We will now, at last, consider the optimal control of the evolution of a quantum system. In this section, we will limit our attention to the a single pure state evolving under the Schrödinger equation:

$$i\dot{\psi} = H(\varepsilon)\psi. \quad (6.21)$$

We will allow the Hamiltonian  $H(\varepsilon)$  of the quantum system to include non-Hermitian terms describing loss. If we take the objective to be *path independent*, i.e. with  $l$  independent of  $\psi$ :

$$J(\zeta, \varepsilon) = \phi(\zeta, \psi(T)) + \int_0^T l(\varepsilon(t)) dt, \quad (6.22)$$

so that  $h = l(\varepsilon) + 2\text{Im}(\lambda^\dagger H\psi)$ , we find the state and adjoint equations to be highly symmetrical:

$$i\dot{\psi} = H(\varepsilon)\psi \quad \psi(0) = \psi_0 \quad (6.23a)$$

$$i\dot{\lambda} = H(\varepsilon)^\dagger \lambda \quad \lambda(T) = \left. \frac{\partial \phi}{\partial \psi^\dagger} \right|_T. \quad (6.23b)$$

An obvious choice for the target objective function  $\phi$  is the overlap with a desired final state  $\psi_1(\zeta)$ :

$$\phi(\zeta, \psi) = 1 - |\psi^\dagger \psi_1(\zeta)|^2 \quad (6.24)$$

leading to  $\partial\phi/\partial\psi^\dagger = -\psi_1\psi_1^\dagger\psi$ . The differential  $dJ$  of the objective can be found from (6.10) by

$$\frac{\partial h}{\partial \varepsilon} = \frac{\partial l}{\partial \varepsilon} + 2\text{Im} \left( \lambda^\dagger \frac{\partial H}{\partial \varepsilon} \psi \right). \quad (6.25)$$

Before moving on to the case of optimizing the evolution over a multidimensional subspace of the Hilbert space, we will now consider in detail how the controls could be parametrized for a form of  $H$  often seen in quantum optics. In addition we will consider a rather technical point concerning the choice of adjoint boundary value in the case of a Hermitian Hamiltonian.

### 6.4.1 Control Parametrization for Quantum Optics

For any numerical calculation, the time dependent controls  $\varepsilon(t)$  must be parametrized in terms of a finite number of real numbers. To perform an optimization, what we are actually interested in, is the gradient of the objective with respect to the vector  $u$  of these numbers. We will now introduce a parametrization of a class of Hamiltonians often seen in quantum optics, and show explicitly how this gradient can be computed by means of the results above.

The controls seen in quantum optics will most often be optical fields, which are conveniently parameterized by their complex Rabi frequencies  $\Omega(t)$ . In terms of these, we may write  $H$  as

$$H(t) = H_0 + \sum_i H_i \Omega_i(t) + H_i^\dagger \Omega_i^*(t), \quad (6.26)$$

where the sum is over the number of fields, and  $H_i$  will typically have the form  $\frac{1}{2} |i\rangle \langle e|$ , but could also be chosen to describe the evolution of parallel fields with a bright state as described in section 5.3.

For reasons to become clear later, we will only consider piecewise constant fields:

$$\Omega_i(t) = \sum_j \Omega_i^{(j)} \mathbf{1}_{[t_{j-1}, t_j]}(t), \quad (6.27)$$

with  $\mathbf{1}_I$  being the indicator function on interval  $I$ . In this case, according to (6.25) the gradient of  $J$  is

$$\frac{\partial J}{\partial \mathbf{u}} = \int_0^T \frac{\partial l}{\partial \mathbf{u}} dt + \sum_{i,j} 2 \operatorname{Im} \left( \frac{\partial \Omega_i^{(j)}}{\partial \mathbf{u}} \int_{t_{j-1}}^{t_j} (\boldsymbol{\lambda}^\dagger H_i \boldsymbol{\psi} - \boldsymbol{\psi}^\dagger H_i \boldsymbol{\lambda}) dt \right). \quad (6.28)$$

In particular this result shows that all information of relevance for the objective gradient is held in the integrand:  $g_i(t) = \boldsymbol{\lambda}(t)^\dagger H_i \boldsymbol{\psi}(t) - \boldsymbol{\psi}(t)^\dagger H_i \boldsymbol{\lambda}(t)$ . The first order approximation to the integral above is obviously  $\Delta t(g(t_1) + g(t_2))/2$ . To increase the accuracy of the estimate without decreasing the size of the time step, we can use a second order correction based on the derivative of the integrand:

$$g'_i(t) = i \boldsymbol{\lambda}^\dagger [H, H_i] \boldsymbol{\psi} - i \boldsymbol{\psi}^\dagger [H^\dagger, H_i] \boldsymbol{\lambda}. \quad (6.29)$$

Approximating  $g(t)$  with a third order polynomial fitting the endpoint value and derivative yields the approximation:

$$\int_{t_1}^{t_2} g(t) dt \approx \frac{1}{2} \Delta t (g(t_1) + g(t_2)) + \frac{1}{12} \Delta t^2 (g'(t_1) - g'(t_2)) \quad (6.30)$$

It is important to note that (6.30) allows us to calculate the second order correction to the integral appearing in (6.27) without decreasing the size of the time step, as both  $g(t)$  and  $g'(t)$  can be calculated from the values of  $\boldsymbol{\psi}$  and  $\boldsymbol{\lambda}$  at time  $t$ .

## 6.4.2 Optimized Adjoint State Boundary Condition

In this section we will show that in the case of a Hermitian Hamiltonian and a penalty function that does not depend on the state  $\boldsymbol{\psi}$ , it is possible to modify the adjoint state boundary condition (6.23) to reduce the required accuracy of the adjoint state propagation. In this case we have by Eq. (6.25) that  $dJ$  is given by

$$dJ = \int_0^T \left[ \frac{\partial l}{\partial \boldsymbol{\varepsilon}} + 2 \operatorname{Im} \left( \boldsymbol{\lambda}^\dagger \frac{\partial H}{\partial \boldsymbol{\varepsilon}} \boldsymbol{\psi} \right) \right] \delta \boldsymbol{\varepsilon}(t) dt. \quad (6.31)$$

Since  $H$  and thus  $\partial H / \partial \boldsymbol{\varepsilon}$  are assumed to be Hermitian, we see that  $dJ$  is not affected by replacing  $\boldsymbol{\lambda}$  with  $\tilde{\boldsymbol{\lambda}}(t) = \boldsymbol{\lambda}(t) + \alpha \boldsymbol{\psi}(t)$  for any real constant  $\alpha$ . As we assume  $l$  to be independent of  $\boldsymbol{\psi}$  and  $H$  to be Hermitian, Eq. (6.23) implies that  $\boldsymbol{\lambda}$  and  $\boldsymbol{\psi}$  will evolve according to the same linear equation, so that replacing  $\boldsymbol{\lambda}$  with  $\tilde{\boldsymbol{\lambda}}$  is equivalent to replacing the boundary conditions for the adjoint state to read

$$\tilde{\boldsymbol{\lambda}}(T) = \boldsymbol{\lambda}(T) + \alpha \boldsymbol{\psi}(T), \quad (6.32)$$

where  $\lambda(T)$  is the unmodified adjoint state boundary value as given by (6.23).

One use of this freedom in the choice of the constant  $\alpha$  is to minimize the norm of the adjoint state,  $|\tilde{\lambda}|$ , in order to relax the requirements of the relative precision of the adjoint state propagation. This minimum is easily calculated from (6.32), but we prefer to illustrate the physical background of the result by calculating it in a different way: We introduce  $\tilde{\phi}$  as  $\tilde{\phi}(\psi) = \phi(\hat{\psi})$ , where  $\hat{\psi}$  denotes  $\psi$  normalized to unit length. Since  $H$  is assumed to be Hermitian,  $\psi$  has unit length at all times, so  $\tilde{\phi}(\psi) = \phi(\psi)$ . None the less, the derivatives of  $\tilde{\phi}$  and  $\phi$  are not equal, as we find that

$$\frac{\partial \phi(\hat{\psi})}{\partial \psi^\dagger} = \frac{1}{|\psi|} \left[ \frac{\partial \phi(\psi)}{\partial \psi^\dagger} - \operatorname{Re} \left( \hat{\psi}^\dagger \frac{\partial \phi(\psi)}{\partial \psi^\dagger} \right) \hat{\psi} \right], \quad (6.33)$$

so that the adjoint state boundary condition, as given by (6.23), corresponding to  $\tilde{\phi}$  is found to be

$$\tilde{\lambda}(T) = \lambda(T) - \operatorname{Re} \left\{ \psi^\dagger(T) \lambda(T) \right\} \psi(T). \quad (6.34)$$

Comparing this expression to Eq. (6.32), it is tempting to let  $\alpha = \operatorname{Re}(\psi^\dagger(T)\lambda(T))$ , which is indeed found to be the value that minimizes  $|\tilde{\lambda}|$  subject to Eq. (6.32).

In conclusion, we have shown that in the case of a Hermitian Hamiltonian and a state-independent penalty function, we are free to replace the adjoint state  $\lambda$  with a modified adjoint state  $\tilde{\lambda}$ , which evolves according to Eq. (6.23), but with boundary conditions given by Eq. (6.34).  $\tilde{\lambda}$  will carry the same error information as  $\lambda$ , but the required relative numerical precision when propagating the adjoint state will be reduced, since the norm of the columns of  $\tilde{\lambda}$  will be smaller than those of  $\lambda$ .

## 6.5 Application to Multi State Quantum Dynamics

When considering quantum information processing, we are often interested in obtaining some coherent evolution of the *qubit subspace*  $\mathcal{H}_Q$  of the full Hilbert space  $\mathcal{H}$ , rather than just transferring a single initial state to a given output state.

As long as we are dealing with the Schrödinger equation, this evolution is completely described by the  $\dim(\mathcal{H}) \times \dim(\mathcal{H}_Q)$  matrix  $\mathbf{U}(t)$  describing the evolution of states starting in  $\mathcal{H}_Q$ , *i.e.* the columns of  $\mathbf{U}(t=0)$  form a basis of  $\mathcal{H}_Q$ .

If we map the state vector  $\mathbf{U}$  to  $\vec{\mathbf{U}}$  by concatenating the real and imaginary parts of the entries of  $\mathbf{U}$  in column order, *i.e.*

$$\overrightarrow{\begin{pmatrix} | & | \\ v_1 & v_2 \\ | & | \end{pmatrix}} = (\operatorname{Re}(v_1)^\top \operatorname{Re}(v_2)^\top \operatorname{Im}(v_1)^\top \operatorname{Im}(v_2)^\top)^\top, \quad (6.35)$$

and stick with the mapping (6.13) between  $V$  and  $V^*$ , we find that

$$\overleftarrow{\mathbf{A}} \overrightarrow{\mathbf{B}} = 2 \operatorname{Re}(\operatorname{Tr}(\mathbf{A}^\dagger \mathbf{B})). \quad (6.36)$$

Again, the state and adjoint equations are found to be highly symmetrical if we choose a state independent penalty function:

$$\dot{\mathbf{U}} = -iH(\varepsilon)\mathbf{U} \quad \mathbf{U}(0) = \mathbf{U}_0 \quad (6.37a)$$

$$\dot{\mathbf{\Lambda}} = -iH(\varepsilon)^\dagger \mathbf{\Lambda} \quad \mathbf{\Lambda}(T) = \left. \frac{\partial \phi}{\partial \mathbf{U}^\dagger} \right|_T. \quad (6.37b)$$

Since the columns of  $\mathbf{U}$  and  $\mathbf{\Lambda}$  are treated independently, we see that the optimized boundary condition for the adjoint state in the case of a Hermitian Hamiltonian discussed in section 6.4.2 applies to each column independently. The gradient of  $J$  is in this case given by:

$$\frac{\partial h}{\partial \varepsilon} = \frac{\partial l}{\partial \varepsilon} + 2 \operatorname{Im} \operatorname{Tr} \left( \mathbf{\Lambda}^\dagger \frac{\partial H}{\partial \varepsilon} \mathbf{U} \right). \quad (6.38)$$

### 6.5.1 Fidelity of Quantum Evolution

In the case of multiple state propagation, the choice of the function  $\phi$ , quantifying how well an obtained evolution  $\mathbf{U}$  approximates the desired evolution  $\mathbf{U}_0$ , is not as obvious as in the case of a single state. As we are concerned with quantum information processing we will assume that all operations start out with an unknown state in the qubit subspace  $\mathcal{H}_Q$  of the full system Hilbert space  $\mathcal{H}$ , and that this subspace is invariant under the ideal evolution  $\mathbf{U}_0$ . The function  $\phi$  should not depend on the evolution of states outside  $\mathcal{H}_Q$ , nor on collective phases on the states originating in  $\mathcal{H}_Q$ . A cautious choice of  $\phi$  fulfilling these conditions could be based on the gate fidelity [12]:

$$\mathcal{F}(\mathbf{U}_0, \mathbf{U}) = \min_{|\psi\rangle \in \mathcal{H}_Q} \left| \langle \psi | \mathbf{U}_0^\dagger \mathbf{U} | \psi \rangle \right|, \quad (6.39)$$

which measures the least possible overlap between the obtained output state  $\mathbf{U} |\psi\rangle$  and the ideal output  $\mathbf{U}_0 |\psi\rangle$  for initial states in  $\mathcal{H}_Q$ . This fidelity measure has the desirable quality that both population transfer from  $\mathcal{H}_Q$  to  $\mathcal{H}_Q^\perp$  and population transfer completely out of  $\mathcal{H}$ , as described by a non-unitary evolution, is counted as loss of fidelity.

From the point of view of optimal control, a significant drawback of the gate fidelity,  $\mathcal{F}$ , is that it is computationally complicated [II]. A computationally accessible fidelity measure which share many appealing features with  $\mathcal{F}$  is the trace fidelity [84],

$$\mathcal{T}(\mathbf{U}_0, \mathbf{U}) = \frac{1}{n} \left| \operatorname{Tr}_{\mathcal{H}_Q} \left( \mathbf{U}_0^\dagger \mathbf{U} \right) \right|, \quad (6.40)$$

where  $n = \dim(\mathcal{H}_Q)$ . In fact, as we will now show,  $\mathcal{T}$  is related to  $\mathcal{F}$  by the strict bound [III]

$$1 - \mathcal{F} \leq n(1 - \mathcal{T}), \quad (6.41)$$

indicating that we can safely replace  $\mathcal{F}$  by  $\mathcal{T}$  for numerical computations on a few qubits at high fidelity.

To prove (6.41), we start by noting that  $\mathcal{F}(\mathbf{U}_0, \mathbf{U})$  is completely determined by the restriction  $\mathbf{O}$  of the operator  $\mathbf{U}_0^\dagger \mathbf{U}$  to  $\mathcal{H}_Q$ . Since  $\mathbf{U}$  describes the evolution of a quantum system, it is possible to extend it to a unitary operation on a Hilbert space containing  $\mathcal{H}$ , and  $\mathbf{O}$  is consequently the restriction of a unitary operator to  $\mathcal{H}_Q$ . In the ideal case  $\mathbf{O}$  will be equal to the identity on  $\mathcal{H}_Q$ , perhaps with the exception of a complex phase.

$\mathcal{F}$  is defined as the minimum of the overlap  $|\langle \psi | \mathbf{O} | \psi \rangle|$  for  $|\psi\rangle \in \mathcal{H}_Q$ . Since the unit sphere of  $\mathbb{C}^n$  is compact, this minimum will be attained for some  $|\psi_0\rangle$ :  $\mathcal{F} = |\langle \psi_0 | \mathbf{O} | \psi_0 \rangle|$ . We now extend  $\{|\psi_0\rangle\}$  to an orthonormal basis  $\{|\psi_k\rangle\}_{k=0, \dots, n-1}$  of  $\mathcal{H}_Q$  by the Gram-Schmidt process. Evaluating the trace fidelity in this basis we find by the triangle inequality:

$$\mathcal{T} \leq \frac{1}{n} \sum_{k=0}^{n-1} |\langle \psi_k | \mathbf{O} | \psi_k \rangle| \quad (6.42a)$$

$$\leq \frac{1}{n} (\mathcal{F} + (n-1)), \quad (6.42b)$$

where we have used that  $|\langle \psi | \mathbf{O} | \psi \rangle| \leq 1$  for all  $|\psi\rangle$  since  $\mathbf{O}$  is the restriction of a unitary operator. By rewriting (6.42b) we obtain the desired relation (6.41)<sup>1</sup>.

We note that the established bound is strict in the sense that for any  $0 \leq \mathcal{F}_0 \leq 1$ , the operator

$$\mathbf{O}_{\mathcal{F}} = \mathbf{1} - (1 - \mathcal{F}_0) |\psi\rangle \langle \psi| \quad (6.43)$$

will fulfill Eq. (6.41) with equality for any  $|\psi\rangle$ .

For numerical calculations it is beneficial to use  $\mathcal{T}^2$  rather than  $\mathcal{T}$  [86]. To make high fidelity correspond to lower values of  $\phi$  with a minimum of 0, we will use

$$\phi(\zeta, \mathbf{U}) = 1 - \frac{1}{n^2} |\text{Tr}(\mathbf{U}_0(\zeta)^\dagger \mathbf{U})|^2 \quad (6.44)$$

which according to (6.37) yields an adjoint state boundary condition of

$$\Lambda(T) = -\frac{1}{n^2} \mathbf{U}_0 \text{Tr}(\mathbf{U}_0^\dagger \mathbf{U}(T)). \quad (6.45)$$

---

<sup>1</sup> Please appreciate the simplicity of this proof: the result lived for several months as a conjecture and had been the subject of much hard work before the proof was suddenly obvious.

## 6.6 Summary

In summary, we have described how methods from optimal control theory can be used to calculate the gradient of an objective functional of the form

$$J(\zeta, \varepsilon) = \phi(\zeta, \mathbf{x}(T)) + \int_0^T l(\zeta, \mathbf{x}(t), \varepsilon(t)) dt, \quad (6.2)$$

describing the performance of the time dependent controls  $\varepsilon(t)$  for a set of system parameter values  $\zeta$ .

We have described in detail how this method can be applied to quantum dynamics governed by the Schrödinger equation, and have also established a close connection between the worst case fidelity (6.39) and the computationally much simpler trace fidelity (6.40). The method could be straight forwardly extended to describe evolution according to a master equation, but we have not done so, as it is not necessary in the REQC system where decoherence is mainly caused by decay.

Main references on optimal control theory have been the books by Bryson & Ho [91] and Luenberger [92].



## CHAPTER 7

# Optimized Gate Implementations for Rare Earth Quantum Computing

We have successfully used the method described in chapter 6 to construct robust implementations of both one and two qubit gates for the REQC-system [III]. This work is far from completed, and the aim of the present chapter is to report on our observations on the performance of the method: what worked, as well as what did not. In addition, we will present our recommendations for a possible continuation of the work.

We have worked exclusively with models based on the Schrödinger equation rather than on the more general master equation. As described in chapter 4, decay from the excited state will be the main intrinsic contributor to loss of coherence in the REQC-system. We believe that the influence of excited state decay on the performance, as measured by the fidelity  $\mathcal{F}$ , is modeled quite well by a non-Hermitian term in the Hamiltonian: This will cause all ions which have experienced decay to not contribute to the overlap defining  $\mathcal{F}$ . Also, to make any difference from direct minimization methods as clear as possible, we have enforced a strict limit of  $\Omega_0$  on the time dependent Rabi frequencies by means of control bounds and not employed any penalty functions.

There are two sides to implementing the method numerically: the purely technical of finding well-performing propagation and minimization algorithms, and the much more heuristic part of deciding on the form of the objective function, the sample parameter values  $\{\zeta_i\}$  to use, and what set of controls to optimize over. The former side will be briefly addressed in the following section, while the emphasis of the chapter will be on the latter part of the problem.

## 7.1 Numerical Implementation

Looking through the conclusions of chapter 6, all we need to implement the optimization method numerically is an optimization algorithm suitable for solving the minimax problem, preferably with the possibility of using nonlinear bounds on the control vector  $\mathbf{u}$ , a state propagation algorithm for determining  $\mathbf{x}(t)$ , and some linear algebra to glue everything together. The commercially available software package Matlab has all these algorithms in an integrated environment, and was consequently an obvious platform for this proof-of-concept implementation.

### 7.1.1 State Propagation

The main problem faced by the state propagation algorithm is that the dependence on the components of  $\mathbf{u}$  must be smooth, so that the values of  $J(\zeta, \mathbf{u})$  are in agreement with the derivative information  $\partial J/\partial \mathbf{u}$  obtained by (6.28). As shown by Fig. 7.1, this requirement is not met by common low order ODE solvers, such as the much used 4.th order Runge-Kutta, and we have consequently examined other methods.

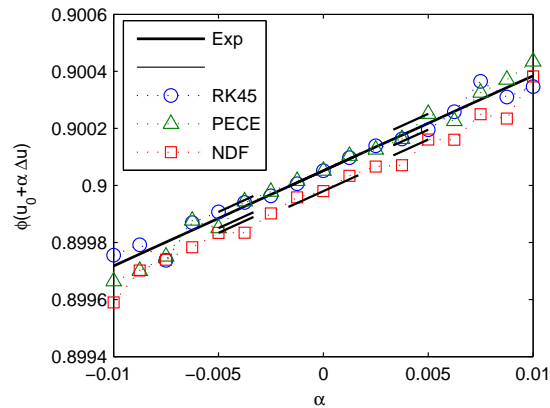


**Figure 7.1:** Propagation noise. The figure shows the computed value of a final state objective function  $\phi$  along a random line  $\mathbf{u}_0 + \alpha \Delta \mathbf{u}$  in the control-parameter space: colored dots are the results obtained by propagating with state of the art low order ODE-solvers: 4.th order Runge-Kutta, variable order Adams-Bashforth-Moulton PECE, and variable order numerical differentiation formulas (NDF), while the solid line indicates the result obtained by numerical matrix exponentiation. Thin line segments indicate the tangents predicted by (6.28), and are seen to be in agreement between propagation methods, and with the results obtained by matrix exponentiation. This figure illustrates that even at high precision, low order solvers can lead to inconsistencies between the calculated objective values and the gradient predicted by (6.28).

In order of increasing accuracy (and implementational difficulty), the relevant alternative propagation schemes for the Schrödinger equation appear to be [93, 94]:

1. Split propagator
2. Short iterative Lanczos
3. Polynomial expansion (Chebychev, Newton, ...)

Split operator propagation is widely used for solving the Schrödinger equation, and is for instance used by the group of H. Rabitz to design optimal type B operations [82]. The global polynomial propagator schemes [95] are very accurate, and have been successfully applied to optimal control of quantum evolution by the group of R. Kosloff [84]. It appears that the performance of the global polynomial propagator methods are clearly superior for high accuracy propagation according to the Schrödinger equation. The numerical complexity of the method has, however, discouraged us from implementing it at this stage of the project.

Instead, we have used a simpler alternative, which has turned out to perform well: By splitting up the the propagation in time slices over which the Hamiltonian can be considered constant, we can reduce polynomial propagation to simple “matrix exponentiation” which is efficiently implemented in standard libraries, often by methods that can be described as global polynomial propagation for constant Hamiltonians. As illustrated by Fig. 7.1, testing have shown the short time polynomial propagation to deliver very consistent results. The method can also be considered advantageous from the point of view of physical intuition: for all practical purposes the result of the propagation is the exact result of propagation with the piecewise constant Hamiltonian submitted to the propagation algorithm.

### 7.1.2 Minimax Algorithm

As seen from the minimax algorithm, the physical problem is just a *black box* described by the vector of objective functions  $J(\zeta_i, \mathbf{u})$ , which maps a control parameter vector  $\mathbf{u}$  to a vector of performances for the different samples  $\zeta_i$ . The purpose of the minimax algorithm is to minimize the worst case performance for the selected samples  $X'$ ,

$$J_{X'}(\mathbf{u}) = \max_{\zeta \in X'} J(\zeta, \mathbf{u}), \quad (7.1)$$

over a set of control parameter vectors  $M$ . By (6.17) the black box calculating  $J(\zeta_i, \mathbf{u})$  is also able to report the partial derivative with respect to  $\mathbf{u}$ , which is what makes the optimization feasible.

For a general discussion of optimization methods (also referred to as nonlinear programming algorithms), we refer to Refs. [96–98]. Various software packages for solving minimax problems are available [99]. In order to have total freedom in choosing the parametrization of the controls, we are interested in optimization methods that are able to handle nonlinear bounds on  $\mathbf{u}$ , such as

some implementations of the Sequential Quadratic Programming (SQP) algorithm [100], e.g. the NLPQL and FSQP packages. We have based our implementation on the minimax procedure of Matlab's optimization toolbox [101], which is based on a quasi-Newton SQP algorithm and is capable of handling nonlinear bounds as well as a range of termination heuristics.

### 7.1.3 Performance

The time complexity of the combined algorithm is somewhat complicated by the fact that for the type of problems considered here, time consumption seems to be split fairly even between the optimization algorithm and the propagation algorithm. The running time of the propagation algorithm is linear in the number of time steps and the number of samples and roughly third order in  $\dim(\mathcal{H})$ . The minimax algorithm on the other hand involves matrix manipulations of the Hessian matrices and is consequently  $\mathcal{O}(\dim(\mathbf{u})^3)$ . It should also be noted that non-linear constraints on the controls are not surprisingly much more expensive than simple bounds.

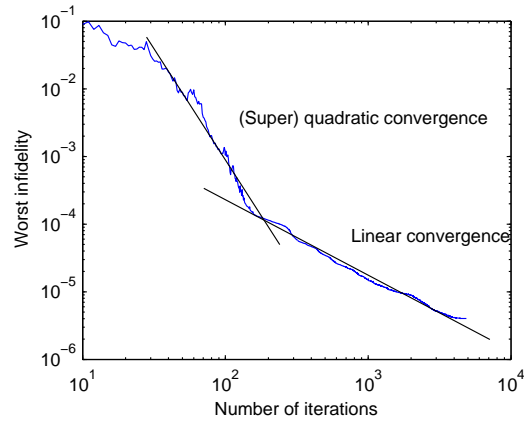


**Figure 7.2:** The achieved gate infidelity ( $1 - \mathcal{F}$ ) as a function of the number of iterations for a typical run of the optimization algorithm. We note that the convergence towards no infidelity is at first quadratic, so that for instance the 90 iteration from number 10 to 100 result in a reduction in the infidelity by a factor of 100. After reaching infidelities on the order of  $10^{-4}$ , the convergence changes to linear, and we see that an increase in the number of iterations by another factor of 10 from 100 to 1000, only results in a reduction of the infidelity by a factor of 10.

As illustrated by a typical convergence sequence as shown in Fig. 7.2, the convergence of the combined algorithm goes through a transition from quadratic to linear convergence at an infidelity on the order of  $10^{-4}$ .

In the quadratic regime, the algorithm updates its approximation of the Hessian along the way, *i.e.* based on the function evaluations at the end of each step.

The transition to the linear regime coincides with the algorithm losing faith in the Hessian, which prompts it to sample an area in parameter space in order to establish a credible approximation of the Hessian before deciding the next step. The transition consistently takes place at infidelities on the order of  $10^{-4}$ , but the precise cause is an open question, although there are some indications that it is related to residual propagation noise.

## 7.2 Examples of Optimized Pulses

To illustrate the problems associated with using the optimization algorithm, we will now consider the problem of robustly implementing a type B operation, *i.e.* a transfer of the population from a known initial state  $|\psi_i\rangle$  to a given final state  $|\psi_f\rangle$ . As in section 5.1 we take the ion to interact with a single field according to the Hamiltonian

$$H = \delta |e\rangle \langle e| + \gamma \left( \frac{\Omega(t)}{2} |0\rangle \langle e| + \text{h.c.} \right). \quad (7.2)$$

To translate this problem to a form that can be addressed by the optimization algorithm, we need to define an objective function,  $J(\zeta, \mathbf{u})$ , choose the sample ion parameters  $\zeta_i = (\gamma_i, \delta_i)$ , and choose a parametrization of the field  $\Omega(t)$  in terms of a real vector  $\mathbf{u}$  of controls.

For the objective function, we will refrain from using a penalty function, and use a final state objective function  $\phi$  based on the overlap between the obtained and desired final state:

$$J(\zeta, \mathbf{u}) = 1 - |\langle e | \mathbf{U}(\zeta, \mathbf{u}; T) | g \rangle|^2. \quad (7.3)$$

Note that the bracket can be considered a generalization of the restricted trace fidelity (6.40) to the case of evolution out of a certain Hilbert subspace, and trivially generalizes to multi-dimensional subspaces.

### 7.2.1 Time Based Field Parametrization

Due to our choice of propagation algorithm, we must use a piecewise constant complex Rabi frequency

$$\Omega(t) = \sum_j \Omega^{(j)} \mathbf{1}_{[t_{j-1}, t_j]}(t), \quad (7.4)$$

where  $\mathbf{1}_I$  is the indicator function on the interval  $I$ . The simplest ways to parametrize the complex vector of  $\Omega^{(j)}$  values in terms of a real parameter vector  $\mathbf{u}$  is by the real and imaginary parts or alternatively by argument and magnitude. Both approaches have minor drawbacks: the gradient of  $J$  with respect to  $\arg(\Omega^{(j)})$  will vanish when  $|\Omega^{(j)}| = 0$ . On the other hand parameterizing  $\Omega(t)$  in terms of  $(\text{Re}(\Omega^{(j)}), \text{Im}(\Omega^{(j)}))$  will turn the bound  $|\Omega^{(j)}| < \Omega_0$  into a nonlinear constraint, making it more demanding to handle for the minimax algorithm.

**Population Swapping.** As our first example, we take that of population swapping, *i.e.*  $|\psi_i\rangle = |0\rangle$ ,  $|\psi_f\rangle = |e\rangle$  as studied in section 5.2. We have seen that an implementation of this operation have surprisingly many applications, and additionally we have a number of implementations with which to compare the resulting pulse.

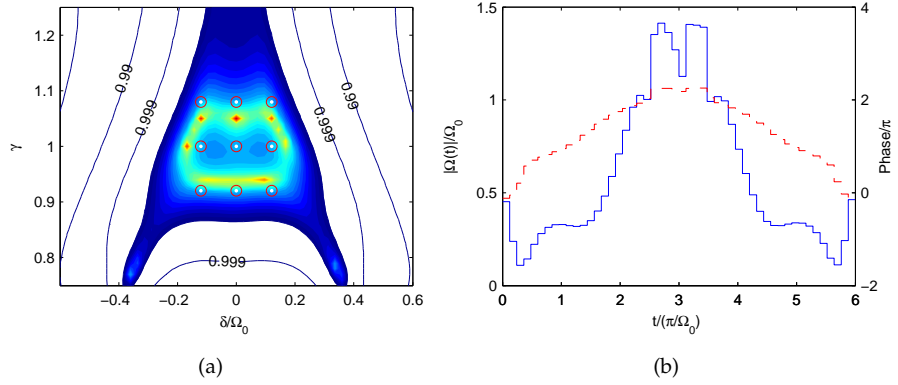


**Figure 7.3:** The performance (a) and pulse shape (b) of a pulse optimized to robustly swap the two populations of a two level system without decay. (a) shows the overlap  $|\langle e|\psi(T)\rangle|$  between  $|e\rangle$  and the final state after starting in  $|0\rangle$ , the infidelity in the colored area is below  $10^{-4}$ . Red circles indicate the sample values used in the optimization process. In (b) the field amplitude is plotted as  $|\Omega(t)|/\Omega_0$  (solid line) together with the phase (dashed line) as a function of time  $t$  in units of  $\pi/\Omega_0$ .  $\Omega(t)$  was parametrized in terms of the real and imaginary parts at each time-step, and only simple bounds on the two components were enforced, allowing the field amplitude to rise to  $\sqrt{2}\Omega_0$ .

Figure 7.3 shows the result of the optimization, starting from a square pulse and using a piecewise constant field with 51 constant parts, parametrized in terms of real and imaginary parts. The duration and the 9 sample parameter values were chosen to obtain a performance similar that of the composite pulse (5.7), as illustrated by Fig. 5.3(b). The calculation presented here required on the order of two minutes to run on a 200 Mflops desktop computer. Several features of the resulting field and performance should be noted:

- The most important observation is that  $J$  is indeed a smooth function of  $\delta$  and  $\gamma$ .
- Duration and performance are similar to that of the composite pulse (5.7).
- The symmetry properties of the field were in no way enforced in the optimization, but is related to the symmetrical choice of samples  $\zeta_i$ . Symmetry considerations are a very important part of composite pulse design, and could be used to reduce the set of control function  $M$  over which the optimization is performed.
- The amplitude fluctuations between 1 and  $\sqrt{2}$  at the center of the pulse

seems to indicate that the simple bounds enforced as  $|\operatorname{Re}(\Omega)| < \Omega_0$  and  $|\operatorname{Im}(\Omega)| < \Omega_0$ , have interfered with the optimization.

- Based on the discussion in chapter 5, we expect that the discontinuities at the edges of the pulse will lead to disturbances of ions surrounding the hole.

## 7.2.2 Fourier Based Field Parametrization

As we aim to construct gate implementations for the REQC system, we cannot allow for detuned ions to be disturbed by the pulses. Obtaining pulses that meet this requirement should be straight forward: if we include samples at large detuning and require that these are not disturbed by the pulse. Attempting this approach with the time-based field parametrization makes the optimization converge towards almost chaotic fields, which do not disturb ions with the exact parameters used for sample values, but are in general highly disturbing to all other detuned ions.

In retrospect, this could have been anticipated: The fundamental assumption in our approach to obtaining robust gate implementations is, that the function  $J(\zeta, \mathbf{u})$  will be a smooth function of  $\zeta$ , so that minimizing  $J_{X'}(\mathbf{u})$  for a discrete set of sample parameter values  $X' = \{\zeta_i\}$  will lead to good performance over a continuous range  $X$  of parameter values. As the smallest frequency scale of the system is  $2\pi/T$ , we should not expect  $J$  to be smooth on larger scales than this. For pulse durations on the order of  $T = 10\pi/\Omega_0$ , this corresponds to a frequency scale of  $0.1 \Omega_0$ . Although this is fine for the core region, as vividly illustrated by Fig. 7.3, it is a very small frequency scale in the far detuned region of  $|\delta| \gg \Omega_0$ .

According to linear response theory, as mentioned in section 5.2.3, we expect the evolution of far detuned ions to be proportional to the Fourier component of the field corresponding to the ion detuning. Based on this, it seems favorable to parametrize the field in terms of a truncated Fourier basis with no frequency components in the far-detuned region:

$$\Omega(t) = \sum_n c_n e^{i\omega_n t}. \quad (7.5)$$

Apart from avoiding disturbing detuned ions, this parametrization reduces the number of controls, and ensures that the resulting pulse does not exceed experimental limitations such as modulator bandwidth. To enforce the field strength limit  $\Omega_0$ , we use a bound based on sampling the field magnitude.

**A 90° Rotation.** As an example of an optimization using the truncated Fourier basis, Fig. 7.4 shows the performance of an optimized 90° pulse with the field expanded on a 21 component truncated Fourier basis.

Although the Fourier basis has no component with angular frequency greater than  $2\Omega_0$ , we observe a significant amount of excitation for ions detuned as far as  $10\Omega_0$ . Looking at the field returned by the optimization (Fig. 7.5), a possible

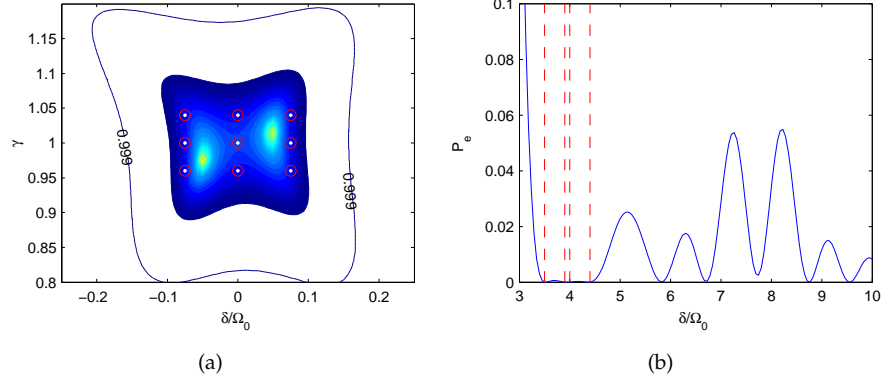


**Figure 7.4:** The performance of a pulse optimized for transferring the population initially in  $|0\rangle$  to the coherent superposition state  $|\psi_f\rangle = (|0\rangle + |e\rangle)/\sqrt{2}$ . In (a) the performance is measured by the overlap  $\langle \psi_f | \psi(T) \rangle$  with the red circles marking parameter values used for optimization, as in Fig. 7.3(a), while (b) shows the excitation probability  $P_{exc}$  for detuned ions with dashed vertical lines marking parameter values used for optimization.

explanation of the failure of the Fourier expanded field to avoid exciting far detuned ions presents itself: Although the frequencies  $\{\omega_i\}$  of the Fourier modes are bounded by  $2\Omega_0$ , the continuous Fourier transform  $\tilde{\Omega}(\omega)$  of the field will not vanish for  $|\omega| > 2\Omega_0$ , in fact we have

$$\tilde{\Omega}(\omega) = \int_0^T \Omega(t) e^{-i\omega t} \frac{dt}{2\pi} = \sum_n c_n \tilde{\delta}^{(T)}(\omega - \omega_n), \quad (7.6)$$

where  $\tilde{\delta}^{(T)}(\omega) = \exp(-i\omega T/2) \delta^{(T)}(\omega)$ , and  $\delta^{(T)}$  is a normalized weight function with a width on the order of  $1/T$ :

$$\delta^{(T)}(\omega) = \frac{\sin(\omega T/2)}{\omega\pi}. \quad (7.7)$$

Numerical calculations indicate, however, that the level of excitation  $P_{exp}$  of far off-resonant ions is still not in agreement with linear response theory when this distinction is taken into account, except at very large detunings.

### 7.3 Approximate Evolution of Off-Resonant Ions

A method for evaluating an approximate evolution of off resonant ions would allow the optimization procedure to address the objective of not disturbing off-resonant ions far more effectively than the sampling approach. Such an approximation method could either be employed to narrow the set of controls,  $M$ , over

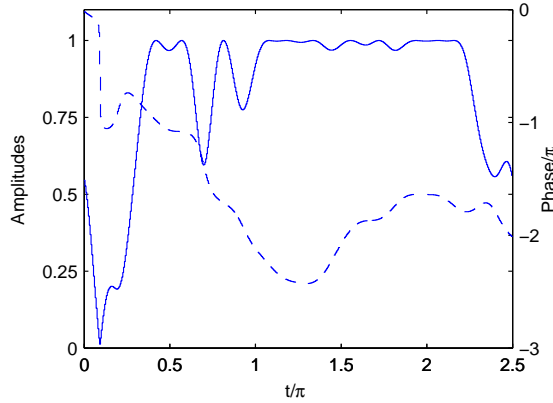


**Figure 7.5:** The field amplitude  $|\Omega(t)|/\Omega_0$  (solid line) and phase (dashed line) of the optimized pulse illustrated in Fig. 7.4. Time  $t$  is plotted in units of  $\pi/\Omega_0$ .

which the optimization is performed, or alternatively to implement *broad range samples* describing the average or worst case fidelity for a range of parameter values.

In this section we briefly report on our unsuccessful attempt to apply a Dyson series expansion to this problem, and also introduce the Magnus expansion, as a seemingly more viable approach.

### 7.3.1 Dyson Expansion

To determine whether the distinction between discrete and continuous Fourier transforms together with linear response theory can explain the observed behavior of far off-resonant ions, we consider a Dyson expansion of the evolution operator, obtained by recursively evaluating the integral form of the Schrödinger equation

$$\mathbf{U}(t_1, t_0) = \mathbf{U}_0(t_1, t_0) + \frac{1}{i} \int_{t_0}^{t_1} \mathbf{U}_0(t_1, t) \mathbf{V}(t) \mathbf{U}(t, t_0) dt. \quad (7.8)$$

**First order.** The only first order matrix elements of  $\mathbf{U}$  are  $\langle e | \mathbf{U}^{(1)} | 0 \rangle$  and Hermitian conjugate, for which we find

$$\langle e | \mathbf{U}^{(1)} | 0 \rangle = \frac{1}{2i} \tilde{\Omega}(\delta), \quad (7.9)$$

which is the result of linear response theory. As mentioned above, numerical calculations indicate that this result is only accurate for very high detunings, so we proceed to determine the second order estimate.

**Second order.** Using an analytical form of the Heaviside step function to make the integration region quadratic [102, Chap. A<sub>1</sub>], the matrix element of the second order term of the Dyson series can be evaluated as:

$$\mathbf{U}_{00}^{(2)} = -2\pi i \int \left| \frac{\tilde{\Omega}(\omega)}{2} \right|^2 \frac{d\omega}{\omega - \bar{\omega}}, \quad (7.10)$$

where  $\bar{\omega} = \delta - i\eta$ , and the expression should be evaluated in the limit  $\eta \rightarrow 0^+$ . In the case of time independent potentials, a re-summation would allow us to take all orders of virtual transitions to  $|e\rangle$  into account. This method does not seem to generalize to the time dependent case and furthermore, the validity in our situation is questionable since higher order corrections should also include transitions to other ground state levels.

To determine  $\mathbf{U}_{00}^{(2)}$ , we must evaluate the integrals

$$I_{n,m} = \int \left( \tilde{\delta}^{(T)}(\omega - \omega_n) \right)^\dagger \tilde{\delta}^{(T)}(\omega - \omega_m) \frac{d\omega}{\omega - \bar{\omega}}. \quad (7.11)$$

which have two removable first order poles on the real axis (or one removable second order pole if  $\omega_n = \omega_m$ ), and can be completed by the method of residues. Doing so we find that

$$\mathbf{U}_{00}^{(2)} = \frac{1}{4} \left( \sum_n \frac{c_n^\dagger}{\Delta_n} \right) \sum_m \frac{c_m}{\Delta_m} (e^{-i\Delta_m T} - 1 + i\Delta_m T \delta_{n,m}), \quad (7.12)$$

where we have introduced  $\Delta_k = \delta - \omega_k$ . Again, we find by numerical calculations that the approximation is only valid for very large detunings.

This negative result could have been anticipated if we had noted that the case of a single field component  $\Omega(t) = \Omega_0 \exp(i\omega t)$  is easily solved exactly. The transition element is found to be:

$$\mathbf{U}_{00}(T) = e^{-i\Delta T/2} \left( \cos \frac{\Omega T}{2} + i \frac{\Delta}{\Omega} \sin \frac{\Omega T}{2} \right) \quad (7.13a)$$

$$\approx 1 + \frac{1}{4} \left( (e^{-i\Delta T} - 1) + i\Delta T \right) \left| \frac{\Omega_0}{\Delta} \right|^2, \quad (7.13b)$$

where  $\Delta = \delta - \omega$  is the combined detuning and  $\Omega^2 = |\Omega_0|^2 + \Delta^2$ . The approximation is the result of a second order Taylor expansion in  $\Omega_0/\Delta$ , as we would expect to obtain from a second order Dyson expansion, and is a special case of (7.12). It is clear that (7.13b) is not a good approximation to (7.13a) as it is not able to describe the oscillatory nature of the exact expression. Based on this observation the failure of the Dyson expansion is not surprising.

### 7.3.2 Magnus Expansion

It appears that perturbation theory in the form of the Dyson expansion is not well suited for describing the oscillatory dependency of  $J$  on  $\delta$  for large detunings. A promising alternative to the Dyson expansion is the *Magnus expansion*,

which has been successfully applied to the perturbative analysis of a similar system by Warren [61].

We refer to Ref. [103] for a recent description of the application of the method to quantum information processing. The central idea is that the exact evolution of the system could also be obtained by evolution according to a constant average Hamiltonian  $\bar{H}$ , for which a series expansion can be obtained. The first term  $\bar{H}^{(0)}$  is the average Hamiltonian, and in our case, the magnitude of the second term  $\bar{H}^{(1)}$  for an ion is given by the Fourier component of the field autocorrelation function corresponding to the detuning frequency of the ion.

## 7.4 Conclusions

In conclusion, our sampling method for robust pulse construction has performed remarkably well. In particular  $J$  has proven to be a smooth function  $\zeta$  in the core parameter area, enabling us to obtain a good performance for a large range of  $\zeta$  values based on a few samples. Below we try to identify and address the central shortcomings of the method as currently implemented.

**Evolution of far off-resonant ions.** It appears that the sampling strategy is not well suited for ensuring that detuned ions are not disturbed by a pulse. Instead we suggest to use a perturbative method to estimate the performance of a set of controls over a range of  $\zeta$ -values, thus avoiding the problems associated with sampling. It appears that the Dyson expansion is not adequate for such a perturbative calculation, whereas the Magnus expansion seems to be a viable approach.

**Implementation robustness.** We have not considered robustness with respect to the implementation: it is conceivable that the performance of the fancy optimized fields collapses at the smallest perturbation of the input phase or amplitude. We do, however, not consider this to be likely since the optimized field is exactly one for which  $J$  experiences a (local) minimum with respect to all instantaneous field values, implying that the dependence on fluctuations in the field would be of at least second order. The dominant implementation imperfection would in most cases be laser phase noise, which could be adequately modeled by decoherence on the optical transitions in a density matrix implementation.

**Pulse duration.** Although the calculations of chapter 6 could easily be extended to include variation in the pulse duration, we have not done so, since in the case of the REQC system, where the optimization algorithm is free to finish "before time", we can obtain the same results by simply using a sufficiently long time interval. This greatly simplifies pulse parametrization, but could be considered a limitation for other uses.

**Parametrization.** It seems that much could be gained by improving the parametrization of the fields. An ideal parametrization would only describe implementable fields with smooth performance in both the core and far-detuned regions. In addition, the resulting pulses should be analytically understandable. Also, symmetry considerations, which are widely employed for pulse construction in the NMR community [59], could be much more widely used to reduce the number of necessary samples and field parameters. We have considered using a truncated Fourier basis multiplied with a sech envelope function. In section 8.1.3 we give an example of an optimization based on a truncated set of harmonic oscillator eigenfunctions, as suggested by Warren [61].

**Direct optimization.** Finally, the central question raised by this chapter is, if sufficient understanding of the detuned samples could allow us to dispel of the field limit, and perhaps switch to a direct optimization method. The point is that without performance criteria for detuned samples, a given pulse can in most cases be improved by increasing the field strength and decreasing the duration, meaning that the direct methods are only convergent because of their penalty functions. The same is not true when disturbing detuned samples is disallowed: in this case there might very well be an optimal field strength defined by the problem. Instead of, or before, actually implementing a direct optimization, the current algorithm could be employed without field limits to see if the problem is well-defined.

# CHAPTER 8

## Two-Qubit Gate Operations

In this chapter, we consider how two-qubit gate operations for the REQC system can be implemented robustly. In contrast to the case of single qubit gates, we do not need to implement every possible gate: together with a complete set of single qubit gates, any completely entangling two qubit gate will suffice.

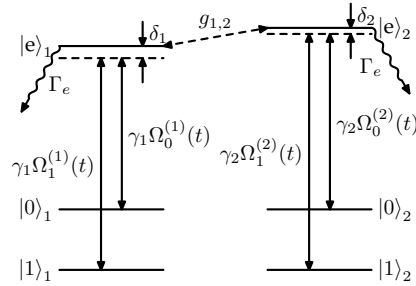


**Figure 8.1:** Two interacting ions.

We will be considering a pair of ions interacting by a static dipole coupling between their excited states (Fig. 8.1), as described by the coupling (3.7)

$$H_c = g (|e\rangle \langle e|)_1 \otimes (|e\rangle \langle e|)_2, \quad (8.1)$$

where we have omitted indices on the coupling strength, as we only consider one pair of ions. What values of  $g$  we will find in an active quantum computer instance is determined during the initialization in accordance with the requirements of the gate operations. The choice of such requirements will determine the number of available quantum computer instances in a given crystal.

We model the ion-field interaction by a single ion Hamiltonian of the form

$$H_i = (-i\Gamma_e/2 + \delta_i) |e\rangle_i \langle e|_i + \gamma_i \sum_j \frac{\Omega_j^{(i)}}{2} |j\rangle_i \langle e|_i + \text{h.c.} \quad (8.2)$$

including the inhomogeneous shift  $\delta_i$  of the excited state with respect to the channel center and a non-Hermitian term describing decay from the excited state.

The optimization method described in chapters 6 and 7 can also be applied to the design of two-qubit gates. One way of doing this would be to plug the whole two-ion Hamiltonian  $H = H_1 + H_2 + H_c$  and the desired evolution matrix into the algorithm, but this is not interesting for a number of reasons: Most importantly, our chance of achieving any intuitive idea of the workings of four simultaneous fields are limited, thus making it impossible to use the optimization results as inspiration for analytically defined gate implementations. Secondly, a direct optimization would result in a set of four time-dependent fields to be applied simultaneously, which would be quite challenging from an experimental point of view. Instead of this brute force approach, we will use the optimization algorithm to design optimized pulses for well defined one-qubit subproblems which emerge in the following.

Gates proposed for the REQC system fall in two categories: the dipole blockade type gates, of which the CNOT-gate described in chapter 4 is an example, suggested for the REQC system by the group of S. Kröll [40], and the comb-gate suggested by the group of M. Sellars [55]. The former class of gates require the coupling strength to be larger than some threshold, while the latter work for a comb of coupling values. These two types of gates will be the topic of the first two sections of the chapter, after which we will take a step back and consider the fundamental capacity of the dipole coupling for creating entanglement, thus establishing a strict relation between gate failure rate and the chosen value of  $g$ .

## 8.1 Dipole Blockade Gates

A formal way to describe the functioning of the dipole blockade gates, such as the CNOT-gate described in section 4.3, is to note that when no fields are applied to ion 1, the two-qubit Hamiltonian can be decomposed as  $H = H^{(1)} + H^{(2)}$ , where

$$H^{(1)} = |e\rangle \langle e| \otimes \left[ \delta_1 \mathbf{1} + (\delta_2 + g) |e\rangle \langle e| + V_{\text{field}}^{(2)} \right] \quad (8.3)$$

$$H^{(2)} = \Pi_Q \otimes \left[ \delta_2 |e\rangle \langle e| + V_{\text{field}}^{(2)} \right]. \quad (8.4)$$

We have ignored decay terms and  $\Pi_Q$  is the orthogonal projection on  $\mathcal{H}_Q$ , i.e.  $\Pi_Q = |0\rangle \langle 0| + |1\rangle \langle 1|$ .

The implication of the above decomposition is that ion 2 will evolve according to an effective detuning of  $\delta_2 + g$  if ion 1 is in the excited state  $|e\rangle_1$ . The

underlying idea of the dipole blockade gates is that if the coupling  $g$  is strong enough, the fields  $\Omega_i^{(2)}$  will be shifted so far out of resonance that they will not affect ion 2 if ion 1 is excited.

### 8.1.1 A Simple Controlled-Phase Gate

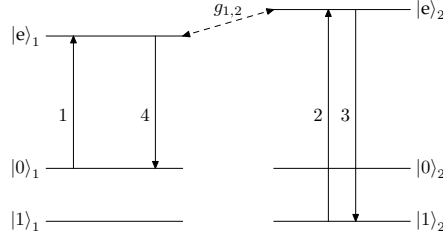


Figure 8.2: Simple phase gate

A fundamental problem of the originally proposed CNOT-gate is that it is not phase compensated. As we have not been able to find any ways of phase compensating it, we will instead consider the similar and equally powerful CPHASE-gate implemented by the following sequence of rotations (Fig. 8.2)

$$\begin{array}{c}
 \hline
 \begin{array}{ccc}
 & 1 & 2-3 & 4 \\
 \hline
 |0\rangle_1-|e\rangle_1 & \hat{x}_\pi & & -\hat{x}_\pi \\
 |1\rangle_1-|e\rangle_1 & & & \\
 |0\rangle_2-|e\rangle_2 & & & \\
 |1\rangle_2-|e\rangle_2 & & \hat{x}_{2\pi} & 
 \end{array}
 \end{array}
 \quad (8.5)$$

The operation of the gate is clear: if ion 1 is in  $|0\rangle_1$  and  $g$  sufficiently large, pulses 2 and 3 will be shifted out of resonance and the target ion will not be affected. If, on the other hand the control ion is in  $|1\rangle_1$ , pulses 2 and 3 will lead to a phase of  $\pi$  on the  $|1\rangle_2$  state, so that the overall effect of the pulse sequence is a phase shift of  $\pi$  on the combined  $|11\rangle$  state.

In effect, a *controlled phase shift* has been applied to the target ion. The CPHASE-gate can be converted to a CNOT-gate by local operations as follows,

$$\begin{array}{c}
 |x_1\rangle \text{---} \bullet \text{---} |y_1\rangle \\
 | \quad | \\
 |x_2\rangle \text{---} \oplus \text{---} |y_2\rangle
 \end{array}
 =
 \begin{array}{c}
 |x_1\rangle \text{---} \bullet \text{---} |y_1\rangle \\
 | \quad | \\
 |x_2\rangle \text{---} \boxed{H} \text{---} \boxed{Z} \text{---} \boxed{H} \text{---} |y_2\rangle
 \end{array}
 \quad (8.6)$$

To see this, consider that if the control qubit is initially in the state  $|1\rangle$ , the operation  $\mathbf{HZH} = \mathbf{X}$  is applied to the target qubit. If on the other hand  $|x_1\rangle = |0\rangle$ , the operation on the target qubit will be  $\mathbf{HH} = \mathbf{1}$ . Eq. (8.6) implies that the CPHASE-gate is as strong as the CNOT-gate. By using parallel fields for the target ion, the Hadamard operations can effectively be integrated in the gate operation as suggested by Roos and Mølmer [63].

### 8.1.2 Twelve-Pulse Phase-Compensated Gate

In light of our discussion of phase errors in chapter 5, it is clear that the simple phase gate (8.5) must be modified to avoid phase errors. In Ref. [II] we suggest the following quite dramatic modification to achieve robustness:

	1	2	3	4	5	6	7	8	9	10	11	12
$ 0\rangle_a e\rangle_a$	$\hat{x}_\pi$					$-\hat{x}_\pi$						
$ 1\rangle_a e\rangle_a$							$\hat{x}_\pi$					$-\hat{x}_\pi$
$ 0\rangle_b e\rangle_b$				$\hat{x}_\pi$	$-\hat{x}_\pi$					$\hat{x}_\pi$	$-\hat{x}_\pi$	
$ 1\rangle_b e\rangle_b$		$\hat{x}_\pi$	$\hat{x}_\pi$					$\hat{x}_\pi$	$-\hat{x}_\pi$			

(8.7)

The idea is to use phase compensating pulses that have no effect on ideal ions, but lead to the right phase contributions for off-resonant ions. In fact, we see that pulses 1-3 and 6 correspond to the uncompensated gate (8.5), while pulses 4-5 and 7-12 have no effect on ideal ions. Compared to the situation discussed in section 5.3, the phase bookkeeping for the controlled gate is slightly more complicated as the population interact with more states. Never the less, since the pulses are sequential, we can calculate the accumulated phase of an ion with detuning  $\delta$  relative to that of an ideal ion by the following table

	1	2-3	4-5	6	8-9	10-11	12
$ 00\rangle$	$\phi_1$		$\phi_3$	$\phi_1 + T\delta_1$		$\phi_2$	
$ 01\rangle$	$\phi_1$	$\phi_3$		$\phi_1 + T\delta_1$	$\phi_2$		
$ 10\rangle$			$\phi_2$		$\phi_1$	$\phi_3$	$\phi_1 + T\delta_1$
$ 11\rangle$		$\phi_2$			$\phi_1$	$\phi_3$	$\phi_1 + T\delta_1$

(8.8)

$\phi_1$ ,  $\phi_2$ , and  $\phi_3$  are the erroneous phase contributions due to the effective inhomogeneous shifts by  $\delta_1$ ,  $\delta_2$  and  $\delta_2 + g$  respectively.  $\phi_3$  may also include contributions from erroneous  $\hat{z}$  rotations caused by the detuned pulse. The terms  $T\delta_1$  included in pulses 6 and 12 describe the phase accumulated due to the inhomogeneous shift of  $|e\rangle_1$  during pulses 1-6 and 7-12 respectively.

In [II] we consider the fidelity of the twelve pulse sequence based on a composite pulse implementation of the rotations. These results were spectacularly improved by Roos and Mølmer [63], by replacing the composite hard pulses with composite Gaussian pulses or sech-pulses Fig. 8.3.

**Optimized Pulse.** An alternative way of formulating the phase bookkeeping of (8.8) is that pulses 2 – 5 and 8 – 11 must implement the operations

$$\mathbf{U}_a^{(12)} = e^{i2\phi_2} \begin{pmatrix} -1 & 0 \\ 0 & 1 \end{pmatrix} \quad \text{and} \quad \mathbf{U}_b^{(12)} = e^{i2\phi_2} \begin{pmatrix} 1 & 0 \\ 0 & 1 \end{pmatrix}, \quad (8.9)$$

respectively for ions within the channel, while at the same time at most inflicting a phase shift of  $\phi_3$  on ions that are shifted beyond the coupling threshold. The latter group of ions will include both ions that have been shifted by the dipole coupling to an excited ion, and ions that live outside the channel anti hole.

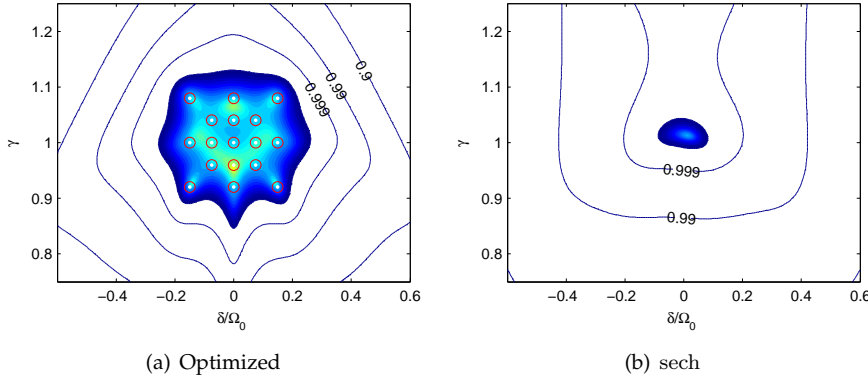


**Figure 8.3:** The fidelity  $\mathcal{F}$  of an optimized pulse implementing  $\mathbf{U}_a^{(12)}$  (a), compared with that of an implementation based on sech-pulses (b). The colored area corresponds to infidelities smaller than  $10^{-4}$ , and the red circles on (a) marks the sample  $\zeta$ -values used for optimization. The duration of the optimized implementation is  $24\pi/\Omega_0$ , compared to  $48\pi/\Omega_0$  for the sech-pulse sequence, and  $2\pi/\Omega_0$  for a naive implementation. The fields were parametrized in terms of a 49 member truncated Fourier basis.

Fig. 8.3 show the performance of an optimized implementation of  $\mathbf{U}_a^{(12)}$  constructed by the method described in chapter 6, compared with that of an implementation based on sech-pulses [III]. The optimization used an objective function based on the reduced trace objective (6.40),

$$J(\zeta, \mathbf{u}) = 1 - \left| \frac{1}{2} \text{Tr} \mathbf{U}_0^\dagger \mathbf{U}(\zeta, \mathbf{u}; T) \right|^2, \quad (8.10)$$

with  $\mathbf{U}_0 = \mathbf{U}_a^{(12)}$  for core samples and  $\mathbf{U}_0 = \mathbf{1}$  for off-resonant samples.

As is clear from Fig. 8.3, the optimized pulse outperforms the sech implementation for the core samples, while Fig. 8.4 illustrates that the sech implementation is better at not disturbing off-resonant samples. It is not clear how a corresponding implementation of  $\mathbf{U}_b^{(12)}$  with the same values of  $\phi_2$  and  $\phi_3$  for all  $\delta_2$  and  $g$  could be constructed by optimization.

### 8.1.3 Seven-Pulse Phase-Compensated Gate

It appears wasteful for the twelve pulse gate (8.7) to rotate the target through  $8\pi$  radians in order to obtain what is just a phase of  $\pi$ . The waste of rotations is particularly worrying, when considering that the controlling qubit must occupy the excited state during half the process. An alternative gate implementation using only a total rotation of  $2\pi$  radians of the target qubit is the following sequence

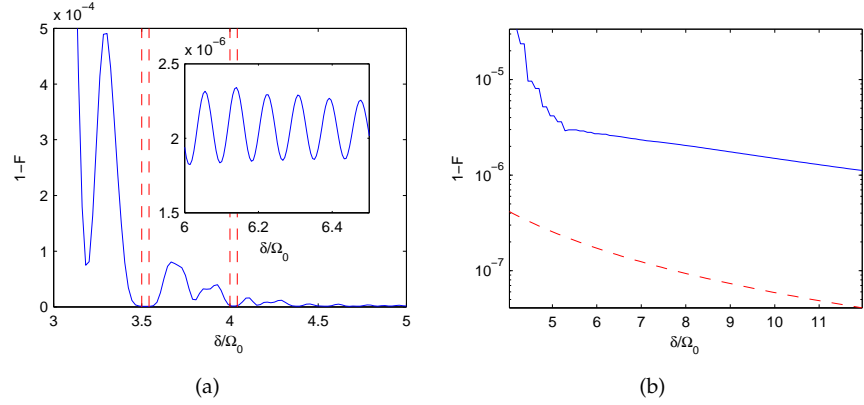


**Figure 8.4:** The perturbation of shifted ions caused by the optimized implementation of  $U_a^{(12)}$ .  $\mathcal{F}$  is calculated with respect to  $\mathbf{1}$ . In (a), the dashed vertical lines show the parameter values used for optimization, and the inset shows the oscillations of the fidelity with a period of the inverse duration of the pulse. In (b), the dashed line shows the much smaller perturbing effect of the implementation based on sech-pulses, compared to a running maximum of the infidelity of the optimized pulse (solid line).

of seven rotations:

$$\begin{array}{cccccccc}
 & & 1 & 2 & 3 & 4 & 5 & 6 & 7 \\
 \hline
 |0\rangle_1 |e\rangle_1 & & \hat{\mathbf{x}}_\pi & & & & & & \hat{\mathbf{x}}_\pi \\
 |1\rangle_1 |e\rangle_1 & & & & & -\hat{\mathbf{x}}_\pi & & & \\
 |0\rangle_2 |e\rangle_2 & & & \hat{\mathbf{z}}_{-\pi/2} & & & \hat{\mathbf{z}}_{\pi/2} & & \\
 |1\rangle_2 |e\rangle_2 & & & & \hat{\mathbf{z}}_{\pi/2} & & & \hat{\mathbf{z}}_{-\pi/2} & 
 \end{array} \quad (8.11)$$

where all  $\hat{\mathbf{z}}$  rotations on the target ion should be dependent on the controlling ion not being in the excited state. Due to the symmetrical form, this gate implementation is seen to be intrinsically robust with respect to phase errors.

To see that the sequence (8.11) indeed implements a universal two-qubit gate, we note that in the standard basis  $\{|00\rangle, |01\rangle, |10\rangle, |11\rangle\}$ , the resulting evolution of  $\mathcal{H}_Q$  is described by

$$e^{-\pi/4} \begin{pmatrix} & 1 & 0 \\ & 0 & i \\ i & 0 & \\ 0 & 1 & \end{pmatrix}, \quad (8.12)$$

so that applying a NOT operation to the control qubit and subsequently applying a  $\hat{\mathbf{z}}_{\pi/2}$  rotation on both qubit spaces will yield an combined operation corresponding to the CPHASE-gate:  $\mathbf{1} - 2|11\rangle\langle 11|$ .

**Optimized Pulse.** Pulses 2–3 and 5–6 of the seven pulse scheme, (8.11) must implement the rotations

$$\mathbf{U}_a^{(7)} = e^{i2\phi_2} \begin{pmatrix} e^{-i\pi/4} & 0 \\ 0 & e^{i\pi/4} \end{pmatrix} \quad \text{and} \quad \mathbf{U}_b^{(7)} = e^{i2\phi_2} \begin{pmatrix} e^{i\pi/4} & 0 \\ 0 & e^{-i\pi/4} \end{pmatrix}, \quad (8.13)$$

respectively for ions within the channel, while at the same time not disturbing ions that are shifted beyond the coupling threshold. The central benefit of the symmetry of the 7 pulse sequence is that a matched set of  $\mathbf{U}_{a,b}^{(7)}$  are automatically provided by an optimization, since an implementation of  $\mathbf{U}_a^{(7)}$  immediately yields an implementation of  $\mathbf{U}_b^{(7)}$  with the exact same value of  $\phi_2$ : all we have to do is interchange the fields.

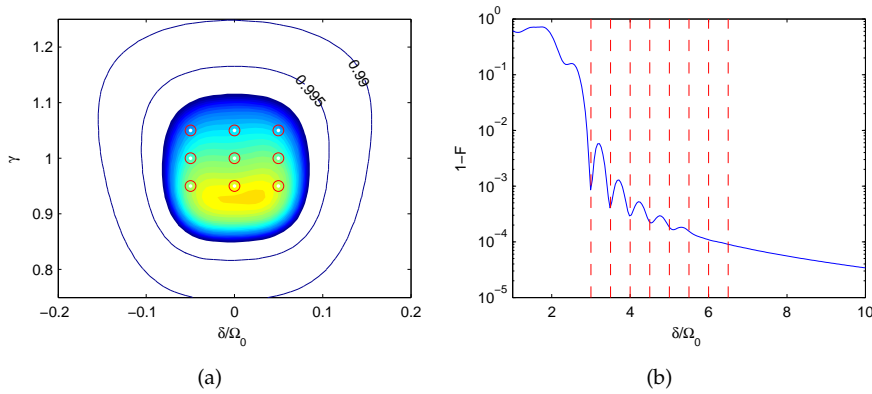


**Figure 8.5:** Performance of an optimized implementation of  $\mathbf{U}^{(7)}$ , including decay from the excited state as described by  $\Gamma_e = 0.002\Omega_0$ . Fidelity of the colored area is between 0.996 and 0.997. The performance for detuned samples (b), where fidelity calculated with respect to the identity, is seen to be good. Red circles (a) and dashed lines (b) indicate optimization sample  $\zeta$ -values.

Figure 8.5 show the performance of an optimized implementation of  $\mathbf{U}^{(7)}$ , starting from a pulse of the type (5.20). Compared to the optimization performed for the twelve pulse scheme, we have introduced a relatively strong decay from the excited state, with  $\Gamma_e = 0.002\Omega_0$ , which as expected leads to significantly lower performance. Furthermore, to obtain a smooth field without edge discontinuities, we have used the 25 first harmonic oscillator wavefunctions for basis functions as suggested by Warren [61]. The oscillator wavefunctions have the advantage of being localized in time, which reflects in the obtained field Fig. 8.6.

A very appealing implementation of (8.11) could be obtained by implementing the  $\hat{x}_\pi$  rotations on the control ion as long-tailed sech-pulses. The performance of the optimized pulse (Fig. 8.5) gives us reason to believe that we can

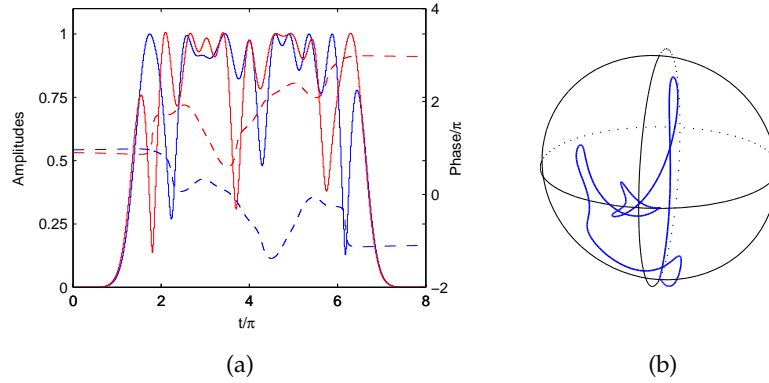


**Figure 8.6:** The field (a) of the optimized  $U_a^{(7)}$  implementation has been expanded on the 25 first harmonic oscillator functions, scaled for the desired duration, which we see is less than  $8\pi/\Omega_0$ , compared to  $48\pi/\Omega_0$  for a sech-pulse implementation. Perhaps surprisingly, the evolution (b) of the Bloch vector of the  $|0\rangle$ - $|e\rangle$  subspace shows that the excited state is not avoided, in spite of the penalty incurred by the decay.

construct pulses implementing  $U^{(7)}$  capable of running on top of the tails of the sech-pulses.

## 8.2 The Comb Gate

The comb-gate proposed by the group of M. Sellars [45] is fundamentally different from the dipole blockade gates considered so far: Instead of relying on the sparse ion pairs with strong coupling, it works for a subset of the much more common low coupling strengths.

We will first describe the original proposal for the comb gate, which uses  $|e\rangle$  and a ground state level, e.g.  $|0\rangle$  as qubit states, and is implemented by the following sequence of rotations,

	1	2	3	4	5	
wait		$T$		$T$		
$ 0\rangle_1$ - $ e\rangle_1$			$\hat{y}_\pi$		$\hat{y}_\pi$	(8.14)
$ 0\rangle_2$ - $ e\rangle_2$	$\hat{y}_{\pi/2}$		$\hat{y}_\pi$		$\hat{x}_{\pi/2}$	

where a  $T$  in the “wait” row specifies a pause of duration  $T$ .

The operation of the comb gate is perhaps best explained by referring to Fig. 8.7. Let us first consider the case of the control ion being in  $|e\rangle_1$  and the target ion being in  $|0\rangle_2$ : here we see that pulse 1 transfers the target ion to the  $\hat{x}$  direction on the equator of the Bloch sphere. During the waiting period, 2, the target ion now evolves under an effective  $|e\rangle_2$  shift of  $g + \delta_2$ , since the control ion is in  $|e\rangle_1$ .

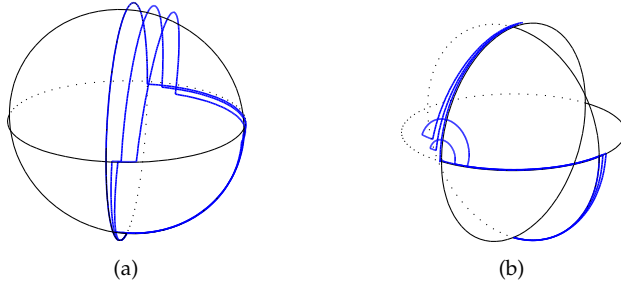


**Figure 8.7:** The evolution of the  $|0\rangle_2$  state of the controlled ion on the  $\{|0\rangle_2, |e\rangle_2\}$  Bloch sphere during the comb gate in the case of the control ion being in the  $|0\rangle_1$ -state (a) or  $|e\rangle_1$ -state (b). The dipole coupling is of a strength corresponding to the innermost positive tooth of the comb, so that during the period  $T$ , it rotates an ideal target ion by  $\pi/4$  around  $\hat{z}$ . Ions are shown with detunings  $\delta/\Omega_0$  of 0, 0.05, and 0.1, and the Bloch sphere (b) is seen from a different angle than (a) in order to more clearly show the dynamics around the  $-\hat{x}$  pole.

This causes the ion to rotate through an angle of  $(g + \delta_2)T$ , before pulse 3 is applied. If we ignore the control ion, pulse 3 would map the state of the target ion to the opposite side of the Bloch sphere, so that after the waiting period 4, the rotation of period 2 would have been canceled for any value of  $g + \delta_2$ , an effect known as *refocusing*. Taking the control ion into consideration, we see that since this is transferred to  $|0\rangle_1$  by pulse 3, only the  $\delta_2$  term will be compensated. In other words: the evolution of the target ion is independent of  $\delta_2$ . By a similar analysis, we find the evolution of  $|0\rangle_2$  to be independent of  $\delta_2$  in the case of ion 1 initially being in  $|0\rangle_1$ .

Having established that the evolution of  $|0\rangle_2$  is independent of  $\delta_2$ , it is relatively easy to see that for  $g$  values such that  $gT = \pi/2 + p2\pi$  for any integer  $p$ , we find the direction of ion 2 at the end of period 4 to be  $-\hat{y}$  or  $\hat{y}$  respectively, depending on the control ion initially being in  $|e\rangle_1$  or  $|0\rangle_1$ . These two states of the target ion are then finally mapped to the  $|0\rangle$  and  $|e\rangle$  states by pulse 5, resulting in a combined operation corresponding to a CNOT-gate up to phase factors.

Note that the gate is intrinsically phase compensated, and that although the rotations appear to be of type A, only the difference in rotation axes are important, making a type B implementation sufficient. We have dubbed the gate “comb gate” in reference to the fact that the values of  $g$  for which the gate operates has the form of a comb, as illustrated in Fig. 8.8.

To initialize the system, Longdell *et al.* [45], suggest to use the gate itself to identify working qubits: By repeatedly applying the CNOT operation on potential qubits initially in the  $|0\rangle$ -state, those ions which do not have the right coupling strengths will not be returned fully from their  $|e\rangle$  state and consequently decay. Since the fidelity of the comb gate in this uncompensated form is approximately  $\cos(\Delta g T)$  where  $\Delta g$  is the deviation from an allowed  $g$  value, we find

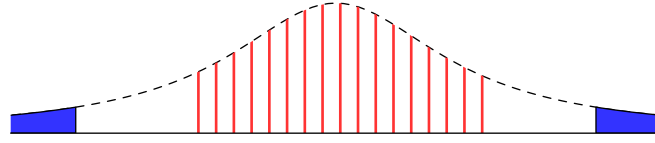


**Figure 8.8:** The coupling strengths  $g = (1 + 4\mathbb{Z})\pi/2T$  accepted by the comb gate (8.14) form a comb across the Lorentzian distribution of coupling strengths experiences between the ions of two channels. Although not shown on the figure, the comb extends into the region of strong coupling. For comparison, the colored areas illustrate the coupling values  $|g| > g_{\min}$  accepted by dipole blockade gates. Note that the teeth of the comb are drawn wider than they should be: their width is at most 1% of the separation.

that the 'duty-cycle' of the comb, *i.e.* the fraction of acceptable  $g$  values, will be on the order of  $(1 - \mathcal{F})^{1/2}$  that is, on the order of 1% for a worst case fidelity of  $1 - 10^{-4}$ .

### 8.2.1 Adaptation of the Comb Gate for the REQC-System

For the REQC-proposal, we need to operate on coherences in the ground state qubit levels. The comb-gate can be adapted to fulfill this by the following sequence of rotations:

	1	2	3	4	5	
wait		$T$		$T$		
$ 0\rangle_1- e\rangle_1$	$\hat{x}_\pi$				$\hat{x}_\pi$	
$ 1\rangle_1- e\rangle_1$			$\hat{x}_\pi$			(8.15)
$ 0\rangle_2- e\rangle_2$	$\hat{x}_\pi$				$\hat{x}_\pi$	
$ 1\rangle_2- e\rangle_2$			$\hat{x}_\pi$			

which is seen to be insensitive to phase errors by symmetry.

Considering the evolution of a basis of  $\mathcal{H}_Q$ , we find, after ignoring global phases due to shifts of the excited state, that the collective states  $|00\rangle$  and  $|11\rangle$  acquire a phase of  $gT$ . Comparing with (8.12), we see that this is equivalent to a phase gate for  $gT = \pi/2 + p2\pi$ .

## 8.3 Entangling Power

In the REQC system, life in the excited state is hard but rewarding: only by placing population in  $|e\rangle$  can we achieve qubit interaction, but at the same time,  $|e\rangle$  is the only state in the system plagued by decay. The proposals for multi-qubit gate operations, which we have seen so far all require a prolonged excitation of the excited states, and one might wonder if this is necessary: could a gate operation conceivably be performed faster, or could the prolonged excitation at least be avoided?

We will now address this question by trying to assess the *entangling power* of the dipole coupling. The idea is quite simple: a two qubit gate strong enough for our purposes must be capable of creating one unit of entanglement. Instead of considering the entanglement created by the full gate operation, we will consider the instantaneous rate of creation of entanglement during the pulse. As we will see, this allows us to draw strong conclusions about the possible performance of any two-qubit gate operation.

Since the results presented here have not previously been published, we present the derivations in some detail.

### 8.3.1 General Theory

**Entanglement** We start by considering the general setting of two quantum subsystems described by Hilbert spaces  $\mathcal{H}_a$  and  $\mathcal{H}_b$ . If the combined system is described by a pure state  $|\Psi\rangle$  in the combined Hilbert space  $\mathcal{H} = \mathcal{H}_a \otimes \mathcal{H}_b$ , the degree of entanglement between the two systems is quantified by the *von Neumann entropy* of the reduced density matrix of either one of the systems:  $E = S(\rho_a) = S(\rho_b)$ , see e.g. Ref. [13].

Calculating  $E$  is most easily done if we Schmidt-decompose  $|\Psi\rangle$  as

$$|\Psi\rangle = \sum_i c_i |v_i\rangle |u_i\rangle, \quad (8.16)$$

where we choose  $c_i$  real and non-negative, and the Schmidt decomposition guarantees that  $\{|v_i\rangle\}$  and  $\{|u_i\rangle\}$  are orthonormal bases of  $\mathcal{H}_a$  and  $\mathcal{H}_b$ , respectively. In terms of the Schmidt decomposition, we have  $\rho_a = \sum_i c_i^2 |v_i\rangle \langle v_i|$ , so that

$$E = S(\rho_a) = - \sum_i c_i^2 \log_2(c_i^2). \quad (8.17)$$

For an initially unentangled system described for instance by the state vector  $|\Psi\rangle = \mathbf{H}|0\rangle \otimes \mathbf{H}|0\rangle$ , we will only have one non-vanishing  $c_i$ , so that  $E = 0$  as expected. By applying a CNOT-gate to the system, we obtain the state

$$\mathbf{U}_{\text{C-PHASE}} |\Psi\rangle = \frac{1}{\sqrt{2}} \left[ |0\rangle \otimes \frac{1}{\sqrt{2}}(|0\rangle + |1\rangle) + |1\rangle \otimes \frac{1}{\sqrt{2}}(|0\rangle - |1\rangle) \right], \quad (8.18)$$

which is written in a Schmidt decomposed form. In this case we find  $E = 1$ : a two qubit quantum gate should be able of creating one unit of entanglement.

**Dynamics of the entanglement.** As described above, we are interested in determining how fast an arbitrary gate operation can create a unit of entanglement.

To maintain the Schmidt decomposition (8.16) during evolution, we must allow all of  $c_i$ ,  $|u_i\rangle$ , and  $|v_i\rangle$  to be time-dependent. The time derivative of the Schmidt coefficients is found to be

$$\left. \frac{\partial}{\partial t} c_i^2 \right|_{t=0} = \frac{\partial}{\partial t} \langle v_i(t) | \rho_a(t) | v_i(t) \rangle = \left. \frac{\partial}{\partial t} \langle v_i(0) | \rho_a(t) | v_i(0) \rangle \right|_{t=0}, \quad (8.19)$$

since  $\rho_a = \sum_i c_i^2 |v_i\rangle\langle v_i|$  and  $\{|v_i(t)\rangle\}$  is an orthonormal basis at all times. To evaluate the derivative, we perform the partial trace of  $\mathcal{H}_b$  in the  $|u_i(0)\rangle$  basis:

$$\frac{\partial}{\partial t} c_j^2 = \frac{\partial}{\partial t} \sum_i \langle v_j(0)u_i(0) | \Psi(t) \rangle \langle \Psi(t) | v_j(0)u_i(0) \rangle \quad (8.20)$$

$$= 2c_j \operatorname{Im} \langle v_j(0)u_j(0) | H | \Psi(0) \rangle, \quad (8.21)$$

using the Schrödinger equation and that  $\langle v_j u_i | \Psi \rangle = c_j \delta_{i,j}$ . Finally, we compute the time derivative of  $E$  according to (8.17), and using that  $\sum c_i^2 = 1$  we find:

$$\dot{E} = -4 \sum_i \log_2(c_i) c_i \operatorname{Im}(\langle u_i v_i | H | \Psi \rangle). \quad (8.22)$$

For later reference, we rewrite (8.22) in a symmetrical form by expanding  $|\Psi\rangle$  in terms of  $|u_i v_i\rangle$ :

$$\dot{E} = 2 \sum_{i,j} \log_2 \left( \frac{c_j}{c_i} \right) c_i c_j \operatorname{Im}(\langle u_i v_i | H | u_j v_j \rangle), \quad (8.23)$$

where we note that the diagonal terms do not contribute.

We see that this expression for  $\dot{E}$  is linear in  $H$ :  $\dot{E}(H_a + H_b) = \dot{E}(H_a) + \dot{E}(H_b)$ , and that terms of the form  $\mathbf{1} \otimes H_a$  corresponding to local operations do not create entanglement:  $\dot{E}(\mathbf{1} \otimes H_a) = 0$  as we would expect.

### 8.3.2 Entangling Power of the Dipole Coupling

According to the final comment of the previous section, the only part of the two-qubit Hamiltonian capable of producing entanglement is not surprisingly the coupling term  $H_c$ ,

$$H_c = g |ee\rangle\langle ee|. \quad (8.24)$$

Note that this implies that in this case, the instantaneous rate of creation of entanglement only depends on the instantaneous state of the ions: the value of the applied field does not enter the expression (8.23).

The total population  $P_e^{(\text{tot})}$  of the two excited states  $|e\rangle_{1,2}$  is

$$P_e^{(\text{tot})} = \sum_i c_i^2 (|\langle u_i | e \rangle|^2 + |\langle v_i | e \rangle|^2) \quad (8.25)$$

Using that  $a + b \geq 2\sqrt{ab}$  for any non-negative  $a$  and  $b$ , we see that

$$w_i \equiv \frac{1}{2} (|\langle u_i | e \rangle|^2 + |\langle v_i | e \rangle|^2) \geq |\langle u_i | e \rangle \langle v_i | e \rangle| = |\langle u_i v_i | ee \rangle|, \quad (8.26)$$

where we have introduced  $\{w_i\}$ , which are seen to fulfill  $\sum_i w_i = 1$  as  $\{|u_i\rangle\}$  and  $\{|v_i\rangle\}$  are orthonormal bases. Inserting  $H_c$  into the expression (8.23), the

inequality (8.26) allows us to establish the following bound on the rate of entanglement creation:

$$\frac{|\dot{E}|}{g} \leq \sum_{i,j} \left| \log_2 \left( \frac{c_i}{c_j} \right) \right| c_i c_j w_i w_j. \quad (8.27)$$

We rewrite this bound by parameterizing  $(c_i, c_j)$  as  $(\sin(\theta_{i,j}), \cos(\theta_{i,j}))(c_i^2 + c_j^2)$ , and introducing  $f(\theta) = |\log(\tan(\theta))| \sin(\theta) \cos(\theta)$ :

$$\begin{aligned} \frac{|\dot{E}|}{g} &\leq \sum_{i,j} f(\theta_{i,j})(c_i^2 + c_j^2)w_i w_j \\ &= 2 \sum_i c_i^2 w_i \sum_j f(\theta_{i,j})w_j, \end{aligned}$$

since  $f(\theta_{i,j}) = f(\theta_{j,i})$ . A closer analysis shows  $f$  to be bounded by 0.5 (or rather the transcendental number 0.478...), so that a rough estimate yields the central result of this section:

$$\boxed{|\dot{E}| < \frac{1}{2} P_e^{(\text{tot})} g.} \quad (8.28)$$

The implications of Eq. (8.28) are clear: in order to obtain one unit of entanglement, a two-qubit gate operation must necessarily suffer an integrated excitation  $\int P_e^{(\text{tot})} dt$  of  $2/g$ , where  $g$  is the dipole coupling strength, or put more briefly: ‘no pain, no gain’.

## 8.4 Conclusion

In this section we compare the different types of multi qubit gates considered, and try to assess how well they are suited for an operational REQC system.

### 8.4.1 Comparison of Multi Qubit Gates

As illustrated by Fig. 8.8 the central difference between the dipole blockade and comb gates is that the former type works for all coupling strengths larger than some threshold  $g_{\min}$ , while the latter operate for a comb of  $g$  values,  $g \in (1 + 4\mathbb{Z})\pi/2T$ .

The shift of the excited state of a given ion when a group of ions are excited is described by a stochastic variable distributed according to a Lorentzian, as we will discuss in detail in chapter 9. The main advantage of the comb gate is that it works for a subset of the ions that are only slightly shifted, which are much more abundant than the highly shifted ions required by the dipole blockade gate.

It appears, however, that this advantage comes at the price of departing from the *independent instance* model, since relying on smaller values of  $g$  will lead to a much more symmetrical coupling topology, where each ion is coupled to a large

number, if not all, members of an other channel. Rather than having an ensemble of independent quantum computers, this would lead to a single quantum computer, in which the register states would be collective states of a macroscopic number of ions. It seems that such a system would be very susceptible to decoherence, but we have not addressed this point in detail.

A less speculative reason for not considering the comb gate further is provided by the limit (8.28) on the entangling power of the dipole coupling. According to this limit, we will not be able to implement a gate with fidelity better than  $1 - 10^{-4}$ , as required by the threshold theorem, for  $g$  less than  $10^4 \Gamma_e$ . For the parameter values considered so far, this would imply a minimal  $g$ -value on the order of 10 MHz. The central advantage of the dipole blockade gate compared to the comb gate is that with the dipole blockade gate, it is possible to use all ions above the threshold, while the comb gate would only be able to use a small subset.

### 8.4.2 Prolonged Excitation of the Control Qubit

A central problem of both the dipole blockade and comb gates considered here, is that the control ion experiences a prolonged excitation, with the associated risk of decay. Even with the relatively short optimized pulse implementation of  $U^{(7)}$  replacing pulses 2, 3, 5, and 6 of the seven pulse sequence (8.11), the control ion must still be excited for a period of  $8\pi/\Omega_0$ .

One way around this problem could be to apply the optimization to the full 4-field problem. As discussed in the chapter introduction, this approach seems uninviting for a number of reasons. Alternatively, the construction of control and target fields could be separated: By first establishing, either through optimization or by classical field design methods, an effective implementation of the control qubit evolution, the target qubit fields could be optimized specifically with respect to that field.

### 8.4.3 Implementability

As illustrated by the performance of the optimized  $U^{(7)}$  implementation (Fig. 8.5), decay of the target ion seems to be a manageable problem. If we are correct in believing decay to be the central intrinsic source of decoherence, the next problem in line is sensitivity with respect to implementation noise. As mentioned in chapter 7.4, we expect the optimized pulses to be first order insensitive to phase and amplitude errors. Also, it appears that it should be possible to implement laser systems with bandwidths several orders of magnitude smaller than other frequency scales of the system, rendering the effects of phase noise insignificant. The validity of this assumption could be tested by modeling laser phase noise as decoherence on the optical transitions.

## CHAPTER 9

# Statistical Properties of the Inter-Ion Dipole Coupling

The strength of the coupling caused by static dipole interaction vary strongly between ion pairs due to the  $r^{-3}$  dependency of the dipole field, together with the random placements of the ions. How exactly the coupling strengths are distributed are of great importance for the scaling properties of REQC, and we will devote this chapter to studying the distribution in detail. To make our approach slightly more general, we will consider the equivalent problem of determining the probability distribution for  $E_z$ , the  $z$ -component of the electric field, inside a random distribution of dipoles.

For ions embedded in a crystal, the distribution in orientation and position will not be uniform: the distribution of orientations will depend on the dipole orientations allowed by the host crystal and the procedure used to change the states of the ions. We will assume the orientations of the individual ions to be independently and identically distributed. Due to the ions being confined to the dopant sites of the host crystal, their positions will be quantized, and, what is more important: since at most one ion can occupy a given site, the spatial positions of the dipoles will be correlated.

In the setting of REQC the occupation rate of the lattice sites will always be low enough that we can ignore spatial correlations between the dipoles, allowing us to use an independent particle model. The main advantage of the simplified model is that we can derive the probability distributions for the field analytically, which we will do in section 9.1 below, for the case where the distribution of dipole orientations is independent of position.

As the results of the analytical calculations for the independent particle model turns out to be rather surprising, we will in section 9.3 introduce an ad-hoc model of spatial correlations to support intuitive feeling that the correlations are indeed unimportant at the dipole concentrations considered here, and to determine to what extend our surprising result carry over to a more precise model. Most of the results of this chapter are published in [IV].

## 9.1 A Spherical Distribution of Dipoles

We will now derive the distribution in field strength experienced by a probe located in the middle of a spherical distribution of dipoles, placed with a uniform density  $\rho$  and with identically distributed orientations. The idea governing the structure of this section, is that we can calculate this distribution by first deriving the distribution of the field caused by placing a single dipole at random in a sphere large enough to hold  $N$  dipoles: Based on the distribution of field contributions from a single dipole, the distribution of the combined field from  $N$  dipoles placed at random in the same sphere can be obtained through a folding integral. Having obtained the distribution of  $E_z$  for finite  $N$ , the bulk distribution<sup>1</sup> can be obtained by taking the limit  $N \rightarrow \infty$ , while keeping the density of the dipoles constant.

Ignoring all effects of the crystal host, the  $z$ -component of the electric field at the probe position due to a source dipole  $\boldsymbol{\mu}$  at  $\mathbf{r}$  is given by

$$E_z = \frac{\mu}{4\pi\epsilon_0} \frac{1}{r^3} ((\hat{\mathbf{z}} \cdot \hat{\boldsymbol{\mu}}) - 3(\hat{\mathbf{r}} \cdot \hat{\mathbf{z}})(\hat{\mathbf{r}} \cdot \hat{\boldsymbol{\mu}})). \quad (9.1)$$

A typical distance between dipoles with density  $\rho$  is  $r_0 = (3/4\pi\rho)^{1/3}$ , and a corresponding typical field strength is  $E_0 = (\mu/4\pi\epsilon_0)r_0^{-3}$ . For notational convenience, we will rewrite Eq. (9.1) in terms of these typical values as

$$g = \frac{E_z}{E_0} = \left(\frac{r}{r_0}\right)^{-3} d(\hat{\mathbf{r}}, \hat{\boldsymbol{\mu}}), \quad (9.2)$$

where we have introduced  $d(\hat{\mathbf{r}}, \hat{\boldsymbol{\mu}})$  as a shorthand for the geometrical factor appearing as the last term of Eq. (9.1).

### 9.1.1 One Dipole in a Sphere

To determine the distribution of  $E_z$  at the center of a sphere of radius  $N^{1/3}r_0$  holding  $N$  dipoles placed at random, we first derive the distribution  $P_{1,N}(g) = P(g|r < N^{1/3}r_0)$  of field contributions from a single dipole placed at random within the same sphere.

The probability density  $P_{1,N}$  can be formally expressed as

$$P_{1,N}(g) = \left\langle \int_0^{N^{1/3}r_0} \delta\left(g - \left(\frac{r}{r_0}\right)^{-3} d(\hat{\mathbf{r}}, \hat{\boldsymbol{\mu}})\right) \frac{3r^2 dr}{Nr_0^3} \right\rangle, \quad (9.3)$$

where we explicitly integrate over the radial distribution of dipoles, and where  $\langle \cdot \rangle$  denotes the expectation value with respect to the orientations of  $\hat{\mathbf{r}}$  and  $\hat{\boldsymbol{\mu}}$ .

<sup>1</sup> When the material has a non-vanishing polarization, care should be taken to distinguish between macroscopic field and local near field, as will be discussed in section 9.2.

<sup>2</sup> Although the formalism is seen to allow for  $\rho$  depending on  $\hat{\mathbf{r}}$ , we have only considered spherically symmetric densities.

Since for a function  $f(x)$  with isolated roots  $x_i$ ,  $\delta(f(x)) = \sum_i \delta(x - x_i)/|f'(x_i)|$ , we can rewrite Eq. (9.3) as

$$P_{1,N}(g) = \frac{1}{Ng^2} \left\langle \left| d(\hat{\mathbf{r}}, \hat{\boldsymbol{\mu}}) \right| \int_0^1 \delta\left(u - \frac{d}{Ng}\right) du \right\rangle \quad (9.4)$$

from which we immediately obtain the important scaling relation

$$\boxed{P_{1,N}(g) = NP_{1,1}(Ng)}, \quad (9.5)$$

relating the distribution observed in a sphere that would hold  $N$  dipoles to the distribution observed in a sphere of radius  $r_0$ .

To proceed beyond the scaling relation, we consider the geometrical factor appearing as the last term of (9.4):

$$D(g) = \left\langle \left| d(\hat{\mathbf{r}}, \hat{\boldsymbol{\mu}}) \right| \int_0^1 \delta\left(u - \frac{d(\hat{\mathbf{r}}, \hat{\boldsymbol{\mu}})}{g}\right) du \right\rangle, \quad (9.6)$$

which depend only on the distribution of  $d(\hat{\mathbf{r}}, \hat{\boldsymbol{\mu}})$ . Noting that the integral is in effect an indicator on the condition  $0 < d/g < 1$ , we can evaluate  $D$  directly in this form, which is how the results of this chapter were initially established.

**One dipole in a shell.** A less cumbersome approach to calculating  $D(g)$  for a given distribution of  $d(\hat{\mathbf{r}}, \hat{\boldsymbol{\mu}})$  goes via calculating the distribution of the field contribution from a single dipole placed at random in a shell centered at the probe.

Parameterizing the radius  $r$  of the shell by  $x = (r/r_0)^3$ , i.e. by the mean number of atoms populating the sphere with radius  $r$ , we have by Bayes rule and the additivity of probabilities of disjoint events that

$$\begin{aligned} P(x_1 < x < x_2) P(g|x_1 < x < x_2) \\ = P(x < x_2) P(g|x < x_2) - P(x < x_1) P(g|x < x_1), \end{aligned} \quad (9.7)$$

where the first factors are simply the probability that a single particle is found in the specified regions of space, so that  $P(x < x_2)/P(x < x_1) = x_2/x_1$ , etc. Since, according to the scaling relation (9.5),  $P(g|x < x_i) = x_i P_{1,1}(x_i g)$ , this implies that

$$P(g|x_1 < x < x_2) = \frac{1}{x_2 - x_1} (x_2^2 P_{1,1}(x_2 g) - x_1^2 P_{1,1}(x_1 g)), \quad (9.8)$$

a result that will prove surprisingly useful.

**Calculating  $D(g)$ .** For the current problem of calculating  $D(g)$ , we apply (9.8) to an infinitesimal shell of radius  $r_0$ , to find that

$$P(d(\hat{\mathbf{r}}, \hat{\boldsymbol{\mu}}) = g) = \lim_{h \rightarrow 0^+} P(g|1 < x < 1 + h) = g P'_{1,1}(g) + 2P_{1,1}(g). \quad (9.9)$$

Expressing  $P_{1,1}(g)$  as  $g^{-2}D(g)$ , and using that  $D(0) = 0$ , this implies that

$$D(g) = \int_0^g u P(d(\hat{\mathbf{r}}, \hat{\boldsymbol{\mu}}) = u) du, \quad (9.10)$$

which is in most cases more tractable than the definition (9.6).

Since  $d(\hat{\mathbf{r}}, \hat{\boldsymbol{\mu}})$  is bounded by 2, (9.10) implies that  $D(g)$  will assume constant asymptotic values for  $|g| > 2$ . If  $P(d = g)$  has vanishing mean, as it will have in the examples considered here, we see that the asymptotic values  $D(\infty)$  and  $D(-\infty)$  will be equal.

Since the single ion field contribution is distributed according to

$$P_{1,1}(g) = g^{-2}D(g), \quad (9.11)$$

the constant asymptotic values of  $D(g)$  imply that  $P_{1,1}$ , and consequently  $P_{1,N}$ , have *algebraic tails* proportional to  $g^{-2}$ . While a  $g^{-2}$  algebraic tail is no problem with respect to normalization, we see already now that  $P_{1,1}$  cannot have a well-defined first moment.

### 9.1.2 Two Important Examples

Before proceeding to put multiple dipoles in the same sphere, we will consider the explicit form of  $D$  for two different distributions of dipole orientations: that of  $\hat{\boldsymbol{\mu}}$  being parallel to  $\hat{\mathbf{z}}$ , and that of  $\hat{\boldsymbol{\mu}}$  being randomly oriented.

**Parallel dipoles.** For dipoles parallel to the  $z$ -axis, the value and corresponding probability density for  $d(\hat{\mathbf{r}}, \hat{\boldsymbol{\mu}})$  is seen to be

$$d^{(p)}(\theta) = 1 - 3 \cos^2 \theta, \quad P(\theta) = \frac{\sin(\theta)}{2} \quad (9.12)$$

from which we readily find  $P(d^{(p)} = g) = 1/\sqrt{12(1-g)}$  for  $g \in [-2, 1]$ , which by (9.10) implies that

$$D^{(p)}(g) = \frac{1}{3\sqrt{3}} \begin{cases} 2 - (2+g)\sqrt{1-g} & \text{if } -2 < g < 1, \\ 2 & \text{otherwise.} \end{cases} \quad (9.13)$$

We note that  $D^{(p)}(g)$  assumes a constant value of  $D_{\infty}^{(p)} = 2/3\sqrt{3} \approx 0.3849$  for  $|g| > 2$ .

**Randomly oriented dipoles.** In the case of randomly oriented dipoles, the distribution in  $d$  is given by

$$d_r = \sin \theta_1 \sin \theta_2 \sin \phi - 2 \cos \theta_1 \cos \theta_2, \quad P(\theta_1, \theta_2, \phi) = \frac{\sin \theta_1}{2} \frac{\sin \theta_2}{2} \frac{1}{2\pi}, \quad (9.14)$$

and we find (after quite a bit of manipulations):

$$D^{(r)}(g) = \frac{1}{\pi} \operatorname{Re} \int \left( \sqrt{s_1^2 s_2^2 - a^2} + 2c_1 c_2 \sin^{-1} \left( \frac{a}{s_1 s_2} \right) \right) \Big|_{a=2c_1 c_2 + g}^{2c_1 c_2} \frac{dc_1}{2} \frac{dc_2}{2}, \quad (9.15)$$

where  $s_i = \sqrt{1 - c_i^2}$  and the integration is over all  $(c_1, c_2)$  for which  $|c_i| < 1$ . Although we have not been able to derive a closed expression for  $D^{(r)}(g)$ , the limiting value of  $D_r$ , can be calculated analytically, and we find

$$D_r(\infty) = \frac{1}{4} + \frac{\sqrt{3}}{24} \sinh^{-1}(\sqrt{3}) \approx 0.3450. \quad (9.16)$$

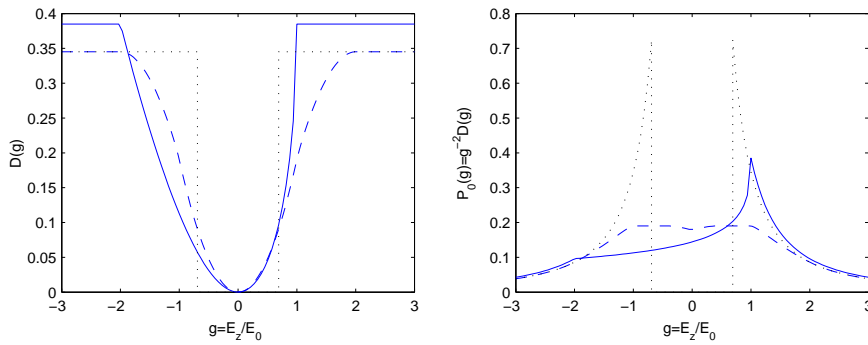


**Figure 9.1:** The geometrical factor  $D(g)$  and corresponding probability distribution  $P_{1,1}(g) = g^{-2}D(g)$  calculated for dipoles parallel to  $\hat{z}$  ( $D^{(p)}$ , solid curve) randomly oriented dipoles ( $D^{(r)}$ , dashed curve), and a step-approximation ( $D^{(\theta)}$ , dotted curve) chosen to have the same limiting value as  $D^{(r)}$ .  $D_r$  was calculated by numerically evaluating the integral (9.15).

Figure 9.1 shows  $D(g)$  and  $P_{1,1}(g)$  for the two examples considered here, compared with a step approximation  $D^{(\theta)}$  chosen to have the same limiting value as  $D^{(r)}$ :

$$D^{(\theta)}(g) = \begin{cases} D_\infty & \text{for } |g| > 2D_\infty \\ 0 & \text{otherwise,} \end{cases} \quad (9.17)$$

where the position of the edge is determined by the normalization of  $P_{1,1}(g)$ .

### 9.1.3 Multiple Dipoles in a Sphere

Having determined the distribution  $P_{1,N}(g)$  of the field contribution from a single dipole in a sphere, we will now proceed to calculate the distribution of the total field due to  $N$  dipoles within the same sphere. Since the field due to  $N$

dipoles is the sum of the individual contributions, the combined field is distributed according to the  $N$ -th order convolution product

$$P_N(g) = \int \delta\left(\sum_{i=1}^N g_i - g\right) \prod_{j=1}^N P_{1,N}(g_j) dg_j. \quad (9.18)$$

The folding integral (9.18) is most easily calculated in Fourier space, where we find that

$$P_N(g) = \int e^{ikg} \left(\tilde{P}_{1,1}\left(\frac{k}{N}\right)\right)^N \frac{dk}{2\pi}, \quad (9.19)$$

with  $\tilde{\cdot}$  denoting the Fourier transform:  $\tilde{f}(k) = \int e^{-ikg} f(g) dg$ . To arrive at (9.19), we have used that the scaling relation (9.5), implies that  $\tilde{P}_{1,N}(k) = \tilde{P}_{1,1}(k/N)$ .

**Series expansion for  $\tilde{P}_{1,1}$ .** Eq. (9.19) implies that to determine  $P_N$  in the limit of  $N \rightarrow \infty$  we must know the dependence of  $\tilde{P}_{1,1}(k)$  for small  $k$ . To find this, we first rewrite  $\tilde{P}_{1,1}(k)$  as

$$\begin{aligned} \tilde{P}_{1,1}(k) &= \int e^{-ikg} g^{-2} D^{(\theta)}(g) dg \\ &\quad + \int e^{-ikg} g^{-2} \left(D(g) - D^{(\theta)}(g)\right) dg, \end{aligned} \quad (9.20)$$

where the first term is conveniently rewritten as

$$1 - 2|k|D_\infty \left(\frac{\pi}{2} - \int_0^{2|k|D_\infty} \frac{1 - \cos(t)}{t^2} dt\right). \quad (9.21)$$

To evaluate the second integral of (9.20), we note that the 0-th order term must vanish since  $g^{-2}D(g)$  and  $g^{-2}D^{(\theta)}(g)$  are both normalized.  $D$  and  $D^{(\theta)}$  are equal for all  $|g| > 2$  and since  $D^{(\theta)}$  is even, the integral is equal to  $-ikg_c + \mathcal{O}(k^2)$  with  $g_c$  defined as

$$g_c = \int_{-g_0}^{g_0} g P_{1,1}(g) dg, \quad (9.22)$$

for any  $g_0 > 2$ . Collecting the two parts we find that

$$\tilde{P}_{1,1}(k) = 1 - \pi D_\infty |k| - ikg_c + \mathcal{O}(k^2). \quad (9.23)$$

#### 9.1.4 The Limit of $N \rightarrow \infty$

We are now very close to our goal of determining the distribution of  $g$  in the limit of an infinitely large sphere. To determine the limit of  $P_N$  for  $N \rightarrow \infty$ , we rewrite (9.19) as  $\log(\tilde{P}_N(k)) = N \log \tilde{P}_{1,1}(k/N)$ . Since  $\tilde{P}_{1,1}(0) = 1$  and  $\log(1 + u) =$

$u + \mathcal{O}(u^2)$ , the leading terms of the series expansion of  $(\tilde{P}_{1,1}(k) - 1)$  will dominate in the limit of  $N \rightarrow \infty$ , so that

$$\log(\tilde{P}_\infty(k)) = -\pi D_\infty |k| - i g_c k, \quad (9.24)$$

from which the limiting distribution follows directly:

$$P_\infty(g) = \frac{1}{\pi} \frac{\Gamma}{\Gamma^2 + (g - g_c)^2}, \quad (9.25)$$

where we have introduced  $\Gamma = \pi D_\infty$ .  $P_\infty(g)$  is a Lorentzian with a half width at half maximum of  $\Gamma$  and a displacement of  $g_c$ .

While  $g_c$  is seen to vanish for the case of randomly oriented dipoles, we find by inserting the explicit expression for  $D^{(p)}$  that in the case of parallel dipoles,  $g_c^{(p)}$  has a non-vanishing value:

$$g_c^{(p)} = \frac{2}{9} \left( 3 + \sqrt{3} \log \frac{\sqrt{3} - 1}{\sqrt{3} + 1} \right) \approx 0.1598. \quad (9.26)$$

This is a quite unexpected result: It shows that the field from a uniform distribution of parallel dipoles is described by a stochastic variable with a Lorentzian distribution with a non-vanishing center value. The shift of the most probable value with respect to zero is surprising when one considers the vanishing mean contribution from any spherical shell around the origin, but it is less surprising when one observes the probability distribution for the single dipole contribution, shown in 9.1. This distribution is indeed suggestive of a shift, but its mean is ill-defined, and (9.22) provides the proper procedure to obtain  $g_c$  from  $P_{1,1}(g)$ . As illustrated by Fig. 9.2, the result is in excellent agreement with numerical simulations.

We note that in terms of absolute field values, the half-width of the Lorentzian is  $\pi D_\infty^{(p)} E_0 \approx 5.065 C \rho$ , and the central value is  $g_c^{(p)} E_0 \approx 0.6692 C \rho$ , where  $C = \mu/4\pi\epsilon_0$ . As both are proportional to the dipole density  $\rho$ , their ratio is independent of  $\rho$ .

The Lorentzian broadening is in agreement with work by Stoneham [105], who considered a variety of line broadening mechanisms in solids, and identified a Lorentzian line as the result of interaction of a single molecule with dislocation dipoles, and more recently [106] Lorentzian line shapes were measured for molecules embedded in low temperature glass with a low-density distribution of dynamical defects. These results were interpreted in terms of Levy stable distributions.

The result (9.25) could also have been obtained by the *generalized central limit theorem*, see e.g. chapter 17 of [107], but the previous calculation has been included to render the result more transparent and to simplify later calculations. For an introduction to generalized (Levy) statistics see [108] for a rigorous introduction or, for instance, [109] for a quick, hands-on approach.

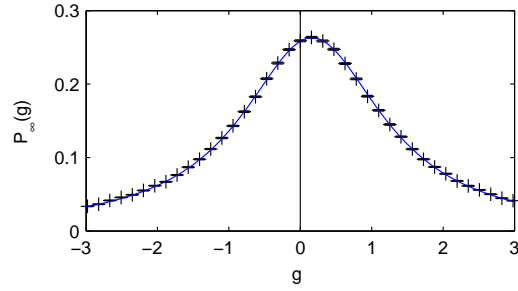


**Figure 9.2:** The probability distribution for  $g = E_z/E_0$ , the scaled  $z$ -component of the combined dipole field inside a random distribution of dipoles aligned along the  $z$ -axis. The symbols show the result of a numerical simulation (based on  $10^6$  realizations of a system with 50.000 individual dipoles, the uncertainty is represented by the line thickness), the solid curve is the theoretical form of the probability distribution, as predicted by (9.25).

## 9.2 Local Field Theory

The fact that the distribution in  $E_z$  converges as we consider larger and larger spheres with a given density of dipoles is deceptive: it is tempting to conclude that the limiting distribution describes the actual field distribution in bulk matter.

If, however, the distribution in  $d$  lead to a non-vanishing macroscopic polarization:  $\mathbf{P} = \rho \langle \boldsymbol{\mu} \rangle$ , this will not be true in general, as is perhaps most easily seen from the argument outlined in Fig. 9.3:



**Figure 9.3:** According to Eq. (9.28), the microscopic (local) field experienced by probe (at the center of the spheres) can be calculated as the sum of the macroscopic field due to dipoles (and external sources) outside a large sphere centered at the probe, and the microscopic field due to the dipoles inside the same sphere, which is distributed according to (9.25).

We can split up the microscopic (local) field at the probe in contributions from a near and a far region:

$$\mathbf{E}^{\text{micro}} = \mathbf{E}_{\text{near}}^{\text{micro}} + \mathbf{E}_{\text{far}}^{\text{micro}}, \quad (9.27)$$

the two being separated by a sphere of radius  $R$ .

The macroscopic field  $\mathbf{E}^{\text{macro}}$  is the microscopic field  $\mathbf{E}^{\text{micro}}$  averaged over sufficiently large volumes that we may replace the dipole distribution with a

polarization density. If we choose  $R$  so that the near region is much larger than this averaging volume, the macro- and microscopic fields contributions from the far region will be identical:  $\mathbf{E}_{\text{far}}^{\text{macro}} = \mathbf{E}_{\text{far}}^{\text{micro}}$ . Since  $\mathbf{E}_{\text{far}}^{\text{macro}}$  is equal to  $\mathbf{E}^{\text{macro}} - \mathbf{E}_{\text{near}}^{\text{macro}}$ , this implies that [110, Chap. 27]:

$$\mathbf{E}^{\text{micro}} = \mathbf{E}_{\text{near}}^{\text{micro}} + \mathbf{E}_{\text{far}}^{\text{macro}} - \mathbf{E}_{\text{near}}^{\text{macro}}. \quad (9.28)$$

What we have calculated in the previous sections is seen to be the distribution in the contributions from the near region to the microscopic field:  $\mathbf{E}_{\text{near}}^{\text{micro}}$ .

Since the field inside a uniformly polarized sphere with polarization density  $\mathbf{P}$  is uniformly  $\mathbf{P}/3\epsilon_0$ , we see as expected that in the case of a spherical sample  $\mathbf{E}^{\text{micro}} = \mathbf{E}_{\text{near}}^{\text{micro}}$ .

### 9.3 An Excluded Volume

The fact that the host lattice introduces spatial correlations between the dipoles is not taken into account in the model analyzed above. Intuitively it seems that when the crystal unit cell is much smaller than a typical volume, say  $1/\rho$ , of the distribution, such spatial correlations should be unimportant. In this section we try to argue this point more quantitatively, by computing the field distribution in the case where no dipoles are allowed inside an *excluded volume* in the form of a sphere of volume  $\epsilon/\rho$  centered at the origin.

The marks in Fig. 9.4 show the results of simulations performed with dipoles put uniformly at random around the origin but outside such excluded volumes, and as we reduce the excluded volume we observe that the probability distributions converge towards the shifted Lorentzian. The generalized central limit theorem, which applies for  $\epsilon = 0$  and  $\epsilon \rightarrow \infty$ , deals with the convergence of the distribution function for a sum of more and more random variables which all have the *same* individual distribution after a suitable rescaling. Such rescaling is not possible for intermediate values of  $\epsilon$ , which thus require a direct calculation of  $P_\infty(\epsilon, g)$ .

To calculate the field contribution from a single dipole when an excluded volume is taken into account, we consider the field contribution from a single dipole placed at random in a spherical shell with outer radius  $(N + \epsilon)^{1/3}r_0$  and inner radius  $\epsilon^{1/3}r_0$ . According to Eq. (9.8) we obtain the following relation between the Fourier transformed probabilities

$$N \tilde{P}(k|\epsilon < x < N + \epsilon) = (N + \epsilon) \tilde{P}_{1,1}\left(\frac{k}{N + \epsilon}\right) - \epsilon \tilde{P}_{1,1}\left(\frac{k}{\epsilon}\right),$$

since  $\tilde{P}(k|x < x_i) = \tilde{P}_{1,1}(k/x_i)$ .

We are interested in the probability  $P_N(\epsilon, g)$  that the contributions from  $N$  dipoles, all having  $\epsilon < x < N + \epsilon$ , add up to the value  $g$ . Performing the convolution in Fourier space we find that  $\log \tilde{P}_N(\epsilon, k) = N \log \tilde{P}(k|\epsilon < x < N + \epsilon)$ , and taking the limit of  $N \rightarrow \infty$  we find

$$\log \tilde{P}_\infty(\epsilon, k) = \log \tilde{P}_\infty(k) - \epsilon \left[ \tilde{P}_{1,1}\left(\frac{k}{\epsilon}\right) - 1 \right]. \quad (9.29)$$

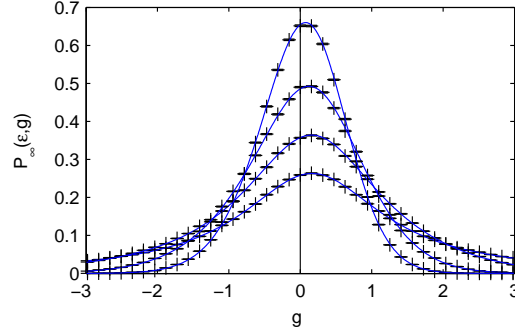


**Figure 9.4:** Distribution of  $g$  for the case of dipoles parallel to the  $z$ -axis when an excluded volume of size  $\epsilon/\rho$  is introduced. Solid lines show the distribution  $P_\infty(\epsilon, g)$  given by (9.29), for  $\epsilon = 0, 0.4, 1,$  and  $2$  in order of increasing maximum densities. Data markers are the result of numerical simulations. The distributions have vanishing mean for all values of  $\epsilon > 0$ , yet they approach the shifted Lorentzian, corresponding to  $\epsilon = 0$ .

Since  $|\tilde{P}_{1,1}| < 1$  and  $\log(\tilde{P}_\infty(k))$  is first order in  $k$ , we find that the term  $\log \tilde{P}_\infty(k)$  will dominate Eq. (9.29) for  $k > \epsilon$ , in agreement with our expectations that  $P_\infty(\epsilon, g)$  should approach  $P_\infty(g)$  for  $\epsilon \rightarrow 0$ .

**Evaluating  $P_\infty(\epsilon, g)$  numerically.** At first it might seem difficult to determine  $\log \tilde{P}_\infty(\epsilon, k)$  numerically for  $\epsilon \rightarrow 0$  through (9.29) based on our knowledge of only the lowest order coefficients in a series expansion of  $\log \tilde{P}_{1,1}(k)$ , as determined in the previous section (9.23). Introducing the notation  $\tilde{P}_{1,1}(k) = 1 + c^*|k| + \sum_{n=1} c_n k^n$ , we find (not worrying about convergence)

$$\log \tilde{P}_\infty(\epsilon, k) = -\epsilon \sum_{n=2} c_n \left(\frac{k}{\epsilon}\right)^n, \quad (9.30)$$

implying that for  $\epsilon \rightarrow 0$  we will have to include more and more terms in the series expansion. To get around this, we use the series expansion at low values of  $k/\epsilon$  and  $\tilde{P}_\infty(k)$  at higher values of  $k$ , with a correction ensuring continuity:

$$\log \tilde{P}_\infty(\epsilon, k) \approx \begin{cases} -\epsilon \sum_{n=2}^{n_c} c_n \left(\frac{k}{\epsilon}\right)^n & \text{for } 0 < k < u_c \epsilon \\ -\epsilon \sum_{n=2}^{n_c} c_n \left(\frac{k_c}{\epsilon}\right)^n + \log \tilde{P}_\infty(k) / \tilde{P}_\infty(k_c) & \text{for } k > u_c \epsilon, \end{cases} \quad (9.31)$$

where  $u_c$  is a cut-off value determined by the order  $n_c$  of the series expansion. For negative  $k$  values, we make use of the fact that  $P_\infty(g)$  is a probability density to conclude that the real and imaginary parts of  $\log \tilde{P}_\infty$  must be even and odd respectively. The accuracy of this approximation is illustrated by Fig. 9.5, where we plot the resulting value of  $\log \tilde{P}_\infty^{(p)}(\epsilon, k)$  for the case of parallel dipoles. As

shown by Fig. 9.4 the resulting values of  $P_\infty(\epsilon, g)$  are in excellent agreement with numerical simulations.

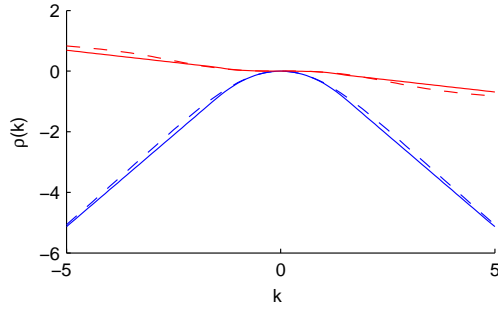


**Figure 9.5:** Assessing the accuracy of the approximation (9.31): the real and imaginary parts of  $\log \tilde{P}_\infty^{(p)}(\epsilon, k)$  for  $n_c = 3$  (solid lines) and 41 (dashed lines).  $\epsilon = 1$  in both cases.

**A large excluded volume.** In the limit of  $\epsilon \rightarrow \infty$  the series expansion (9.30) will be dominated by the leading term, so that  $\log \tilde{P}_\infty(\epsilon, k)$  will approach  $c_2 k^2 / \epsilon$  asymptotically, corresponding to  $P_\infty(\epsilon, k)$  approaching

$$\frac{1}{\sqrt{4\pi c_2 / \epsilon}} e^{-\frac{k^2}{4c_2 / \epsilon}}, \quad (9.32)$$

a Gaussian with variance  $2c_2 / \epsilon$ . The Gaussian is a Levy stable distribution, and this limiting form could have been obtained by the classical central limit theorem by a suitable rescaling. For dipoles parallel to the  $z$ -axis we find

$$\tilde{P}_{1,1}^{(p)}(k) = 1 - \frac{2\pi}{\sqrt{27}}|k| - i\frac{2}{9} \left( 3 + \sqrt{3} \frac{\sqrt{3}-1}{\sqrt{3}+1} \right) k + \frac{2}{5}k^2 + i\frac{4}{105}k^3 + \mathcal{O}(k^4) \quad (9.33)$$

allowing us to conclude that  $P_\infty^{(p)}(\epsilon, g)$  asymptotically approaches a Gaussian distribution with variance  $\text{Var}(g) = 4/5 \epsilon^{-1}$ . As illustrated by Fig. 9.6, this is in good agreement with numerical simulations.

### 9.3.1 An Alternative Derivation of $P_\infty(\epsilon, g)$

It is instructive to note that  $P_\infty(\epsilon, g)$  can also be obtained by an entirely different approach, starting from the outside of the sphere.

Consider  $P_\infty(g|x > x_0)$ : the probability of observing a field component  $g$  from a random collection of dipoles, all with  $x > x_0$ , so that,  $P_\infty(\epsilon, g) = P_\infty(g|x > \epsilon)$ . The central idea of this derivation is that we can calculate  $P_\infty(g|x > x_0 - h)$  by combining  $P_\infty(g|x > x_0)$  with the contributions from dipoles in an

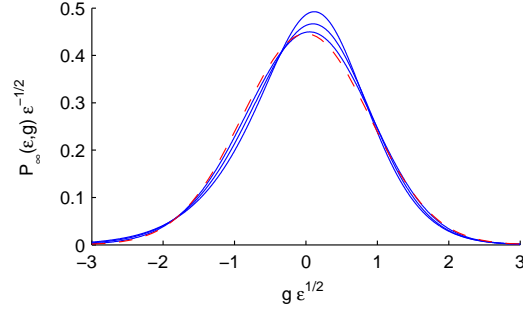


**Figure 9.6:** Rescaled versions of  $P_\infty(\epsilon, g)$  plotted for  $\epsilon = 1, 2, 10$ , ordered by decreasing maximum value (solid lines), compared with the limiting Gaussian distribution as given by (9.32) and (9.33) (dashed line).

infinitesimal shell with  $x \in [x_0 - h, x_0]$ :

$$P_\infty(g|x > x_0 - h) = (1 - p) P_\infty(g|x > x_0) + p \int P_\infty(g - g'|x > x_0) P(g'|x = x_0) dg', \quad (9.34)$$

where  $p$  is the probability of finding a dipole in the shell: if we do find a dipole in the shell we obtain  $P_\infty(g|x > x_0 - h)$  by folding with the single dipole contribution  $P(g|x = x_0)$ , and otherwise the distribution is unchanged<sup>3</sup>. The probability of finding a dipole in the shell is to first order  $\rho 4\pi r^2 dr = dx$ , so that  $p = h$ . Introducing the probability density  $P_d(g) = P(d = g)$ , we note that  $P(g|x = x_0) = x_0 P_d(x_0 g)$ , so that Fourier transforming (9.34) and taking the limit of  $h \rightarrow 0^+$ , we obtain a simple differential equation in  $x_0$

$$\frac{\partial}{\partial x_0} \log \tilde{P}_\infty(k|x > x_0) = 1 - \tilde{P}_d\left(\frac{k}{x_0}\right). \quad (9.35)$$

Changing variables to  $x_0^{-1}$ , we can use the boundary condition that  $P_\infty(g|x > x_0)$  must approach  $\delta(g)$  for  $x_0 \rightarrow \infty$  to obtain the following expression at  $x_0 = \epsilon$ :

$$\log \tilde{P}_\infty(\epsilon, k) = -k \int_0^{k/\epsilon} \frac{1 - \tilde{P}_d(t)}{t^2} dt, \quad (9.36)$$

which can be brought into the form (9.29) using (9.10).

## 9.4 Summary and Discussion

In summary, we have identified a shifted Lorentzian distribution as the probability distribution for the total field inside a random spherical distribution of

<sup>3</sup> This approach seems to be related to *continuous time random walks* [111].

dipoles:

$$P_\infty(g) = \frac{1}{\pi} \frac{\Gamma}{\Gamma^2 + (g - g_c)^2}, \quad (9.25)$$

where  $g = E_z/E_0$  is the field component relative to the typical field. The width and center-value of the Lorentzian are determined from (9.10) and (9.22). The parameters have been analytically calculated for the case of parallel dipoles (9.12) and randomly oriented dipoles (9.14):

$$\begin{aligned} \Gamma^{(p)} &= \frac{2\pi}{\sqrt{27}} && \approx 1.209 \\ g_c^{(p)} &= \frac{2}{9} \left( 3 + \sqrt{3} \log \frac{\sqrt{3}-1}{\sqrt{3}+1} \right) && \approx 0.1598 \\ \Gamma^{(r)} &= \frac{\pi}{4} + \frac{\pi\sqrt{3}}{24} \sinh^{-1}(\sqrt{3}) && \approx 1.084 \\ g_c^{(r)} &= 0 \end{aligned} \quad (9.37)$$

where we in particular note that the distribution center value  $g_c^{(p)}$  does not vanish in the case of parallel dipoles. In addition we have identified a family (9.30) of distributions for the case where dipoles are not permitted inside an excluded volume around the origin in order to model spatial correlations. These distributions all have well-defined and vanishing mean, and they converge to Gaussian distributions in the limit of large excluded volumes and towards the Lorentzian in the case of small excluded volumes.

It is not an inconsistency of our results that the shifted Lorentzian is approached by distributions with vanishing mean: a Lorentzian can be ascribed any mean value depending on how the upper and lower limits are taken in the integral over the distribution. There is in fact reason to emphasize that the common procedure of fitting a spectrum to a Lorentzian may be quite misleading if one tries to interpret an frequency shift as the mean value of a possible perturbation of the energy of the system.

While the fact that  $P_\infty(g)$  is a Lorentzian is well known [112] and have been observed experimentally, we have not found any reports of the shift of the center value predicted here for parallel dipoles. The experimental verification of the shift is made difficult by the macroscopic field effects discussed in section 9.2, and it is not obvious what experimental setup would allow sufficient control of the macroscopic field to directly measure the shift. One system where parallel dipoles can be obtained is the rare-earth-ion doped crystals: Although we will most often excite anti-parallel groups of dipoles simultaneously [113, 114], in which case  $g_c$  is seen to vanish, it is possible to selectively excite one orientation by Stark shifting the two anti-parallel dipole orientations away from each other [113]. In order to determine the macroscopic field in this configuration, we need to know the polarization density of the entire crystal. This is experimentally challenging, as it appears to require laser fields of homogeneous intensity over the full extend of the crystal. In addition to establishing a known polarization density within the crystal, we need to know the electrostatic boundary conditions. Since the dipole field of the crystal could induce almost unpredictable

fields, this would probably most easily be achieved by “shorting” the external field by means of electrodes.

### 9.4.1 Implications for REQC

When manipulating rare-earth-ion doped crystals with optical fields, we address all ions in a given channel simultaneously. Since the dipole interaction is long-range, each ion in one channel will feel the field of all ions from a second channel. As this combined field will vary between dipoles, the resulting shift will also vary, leading to an *instant diffusion* of the spectral structure (Fig. 9.7).

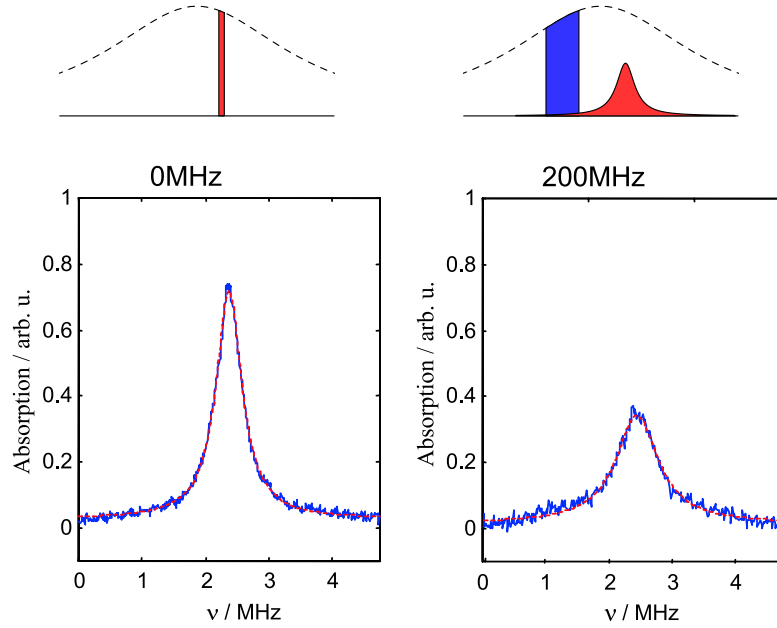


**Figure 9.7:** Instant diffusion. The two leftmost figures show a spectral structure before the perturbing dipoles are introduced. In the right column, the ions in a range of frequencies, indicated by a slice of the inhomogeneous profile in the top figure, have been excited causing an instant diffusion of the initial spectral structures. The two lower figures are an example of an experimental observation of the phenomena [29].

Since the shift of the individual ions can be considered to be independent, the observed broadening should be described by the distribution

$$P(\nu) = \frac{1}{\pi} \frac{\Gamma_\nu}{\Gamma_\nu^2 + \nu^2}, \quad (9.38)$$

where  $\Gamma_\nu = \pi D_\infty \nu_0$ , and  $\nu_0$  is a typical shift given by  $h \nu_0 = \mu E_0$ , corresponding to the shift caused by the interaction between the shifted ion and an ion from

the excited channel at a distance  $r_0$  corresponding to the density of the excited channel. The exact width of the Lorentzian depends through  $D_\infty$  on the distribution of dipole orientations as described by (9.6). We have not calculated  $D_\infty$  for any relevant distributions.

The important point remains however that the width  $\Gamma_\nu$  of the Lorentzian is on the order of and strictly proportional to  $\nu_0$ . Since  $\nu_0$  is proportional to  $r_0^{-3}$ , this implies that we should expect the width to be proportional to  $\rho$ , as has indeed been observed [29]. In this article Nilsson *et al.* measures a broadening proportional to the density of excited ions and reaching  $\Gamma_\nu = 600$  kHz at  $r_0 = 7$  nm, corresponding to dipole moments on the order of  $10^{-31}$  C m. Although this experiment was performed for Tm:YAG, it is reassuring that the result is of the same magnitude as the dipole moments used for Eu in chapter 3.



# CHAPTER 10

## Meeting the DiVincenzo Criteria

In this chapter, we will take a step back to get if not a birds eye view, then at least a broader view of the REQC proposal as we understand it at this point. To this end, we return to DiVincenzo's list of quantum computer requirements presented in section 2.4.2, and examine to what degree these requirements are met. Rather than just accept, in the manner of a conclusion, the shortcomings that are revealed by this analysis, we will attempt to find ways of removing them.

### 10.1 Scalability

There are two distinct factors limiting the size of quantum computers that can be implemented in the REQC system: The number of available channels and whether enough valid instances are available with the requested number of qubits.

#### 10.1.1 Available Channels

Using 0.5% doped  $\text{Eu}^{3+}:\text{YAlO}_3$  as an example, the inhomogeneous width  $\Delta^{(\text{inhom})}$  of the  ${}^7F_0$ - ${}^5D_0$  transition is larger than 10 GHz [35]. If the channels are not interleaved but constructed by putting structures as Fig. 4.1(b) sequentially after each other, each channel requires on the order of 100 MHz [40] of the inhomogeneous profile, allowing for up to 100 channels. Should this become a limiting factor, there are several theoretical possibilities for increasing the number of channels.

One way could be to introduce a systematic shift, e.g. by an electric field gradient, in addition to the inhomogeneous shift.

Alternatively, the channels could be interleaved, in the sense that the frequency used to address the transition  $|e\rangle_j-|1\rangle_j$  could be between the frequencies used to address  $|e\rangle_i-|1\rangle_i$  and  $|e\rangle_i-|0\rangle_i$ . This approach would require highly fre-

quency selective gate operations, but the number of channels would be limited only by the homogeneous linewidth of the transition. In the case of our example the homogeneous linewidth is on the order of 1 kHz [35], allowing for as much as  $10^7$  channels [40].

### 10.1.2 Available Instances

We will consider the number of available instances only for the bus architecture introduced in section 4.2.1. In the bus architecture, we only require each “outer ion” to be coupled to a central ion acting as a *bus*. As a consequence, there will be slightly more valid bus instances than fully interconnected instances available in a given crystal.

For the  $\text{Eu}^{3+}:\text{YAlO}_3$  example system, the typical Eu ion separation  $r_0 = (3/4\pi\rho)^{1/3}$  at 0.5% doping is approximately 1.3 nm. Assuming the inhomogeneous broadening to be described by a 10 GHz wide Lorentzian, the corresponding distance for a channel with  $\Delta^{(\text{chan})} = 100$  kHz is seen to be on the order of 100 nm. Comparing with the dipole strengths mentioned in section 3.3.1, we see that this corresponds to a typical coupling strength  $g_0$  of 1 kHz.

According to the results of section 8.3, it is an absolute requirement that the dipole coupling is stronger than  $\Gamma_e/P_{\text{dec}}$  in order to be able to achieve a worst case error probability below  $P_{\text{dec}}$ . To get above the threshold for successful error correction, we need  $P_{\text{dec}}$  to be no larger than  $10^{-4}$ , which for the example system with  $\Gamma_e \approx 1$  kHz leads to the absolute requirement that  $g_{\text{min}}$  must be larger than 10 MHz.

When we excite the members of a channel, the probability  $P(g)$  that a given ion experiences a shift  $g$  is according to chapter 9 described by a Lorentzian distribution with a width on the order of the the interaction strength  $g(r_0)$  at the typical distance  $r_0$ , in agreement with Ref. [29]. In our case we are interested in the probability  $\eta = P(|g| > g_{\text{min}})$  that an ion is shifted more than  $g_{\text{min}}$  which we find to be on the order of  $g_0/g_{\text{min}}$ , corresponding to  $10^{-4}$  for the example parameters.

The implications of this low probability for the scaling properties of the REQC system are rather grim: if we consider a particular ion from the bus channel,  $\eta$  represents the probability that it will be within interaction distance of a representative of a given channel. Assuming the spatial distribution of the channels to be independent, this implies that the probability that an ion from the bus channel is coupled to  $n$  different channels is  $\eta^n$ , which for  $\eta = 10^{-4}$  imply a very poor scaling of the number of available instances as a function of  $n$ .

### 10.1.3 Asymmetrical Bus

One architecture modification that could completely change the scaling properties of REQC is the *asymmetrical bus* [115]. In its most radical form, the asymmetrical bus architecture ensures that all bus ions are members of a valid instance, making the system scale free up to the maximal number of supported qubits.

For all bus ions to be part of a valid instance, a representative of each channel must be within coupling range of a given bus ion. This is seen to require an asymmetry between the qubit and bus channels, as we would otherwise have a high level of internal coupling within each qubit channel, voiding the independent instance model.

Two ways of establishing the bus qubit asymmetry have been suggested, but neither has been studied in detail: One approach would be to use multiple frequency channels for each qubit, ensuring that at least one channel is represented at each bus ion. Alternatively, a different dopant species with a high dipole moment could be introduced, as the typical interaction strength  $g_0$  scales linearly with the dipole moment of the bus ion. For the example system, we require  $10^4$  channels per qubit or a species of bus qubits with  $10^4$  times larger dipole moment than the Eu ions. The two methods can be combined if needed.

**Removing extra channel representatives.** In an asymmetrical bus system, the actual number of channel representatives within interaction distance of the bus ion is given by a Poisson distribution. To ensure that 99% of the bus ions are members of a valid instance with  $n = 10$  qubits, we find that we must require each bus ion to interact with an average of 7 representatives of each channel. The scaling in this setting is graceful, as we find that the number of invalid bus ions is proportional to  $n$ : If we raised  $n$  to 20 qubits with 7 representatives per channel, we should still expect 98% of the bus ions to be part of a valid instance.

In an operating instance, we will most likely want to know the number of representatives of each channel [116], to which end we could deactivate superfluous qubit ions by the following procedure. We start out with the bus in the state  $(|0\rangle + |1\rangle)/\sqrt{2}$  and assume it to be coupled to  $N$  outer qubits in the  $|0\rangle$  state. For an integer  $m$ , a phase shift of  $\pi/(m-1)$  on the  $|0\rangle$  states of the outer qubits conditioned on the bus state would yield the state

$$\frac{1}{\sqrt{2}} \left( |0\rangle + \exp(i\frac{N}{m-1}\pi) |1\rangle \right) \otimes |0\rangle^N. \quad (10.1)$$

If we now map the two orthogonal states  $\frac{1}{\sqrt{2}}(|0\rangle + \exp(i\frac{1}{m-1}\pi)|1\rangle)$  and  $\frac{1}{\sqrt{2}}(|0\rangle + \exp(i\frac{m}{m-1}\pi)|1\rangle)$  of the bus, to  $|0\rangle$  and  $|1\rangle$  respectively, the bus will be in state  $|1\rangle$  if  $N = m \bmod 2(m-1)$ . By performing this operation for  $m = N_{\max}, N_{\max} - 1, \dots$ , and using the result to perform conditioned burns, it should be possible to obtain a large fraction of instances with exactly one representative from each channel.

### 10.1.4 Structured Doping

Another way of improving the scalability properties of REQC is to construct the crystals specifically to ensure a high number of available instances in a crystal. No suggestions have been made for how to extend this approach to more than a few qubits.

## 10.2 Initialization

The DiVincenzo list requires that the qubits can be prepared in a simple initial state. For the REQC system we must extend the initialization to include the preparation of channels and selection of instances, compared to which preparing the qubits in a given state is a small detail.

By the method of hole burning, we need to apply on the order of 14 repetitions to reduce the population of unwanted ions by a factor of  $10^4$ . Although this should not be critical in an operational implementation, it is worth noting that *unitary initialization* is theoretically possible, since the initialization process takes the combined state of the ions from one pure state (all ions in their  $|0\rangle$  state) to another (deactivated ions in their  $|\text{aux}\rangle$  state), so that there is no need for the phase space compression associated with the decay in the proposed initialization procedure. In spite of the fact that unitary initialization is clearly possible, it is only recently that we have discovered the following method for achieving it.

**Unitary Initialization.** A step towards unitary initialization can be made by noting that since the  $|\text{aux}\rangle$ -states are unpopulated at the beginning of the initialization, the first conditioned burn on each channel can be replaced with a unitary population transfer from  $|0\rangle$  to  $|\text{aux}\rangle$  [117].

In the asymmetrical bus architecture, where all bus ions are parts of a valid instance, the above procedure can replace the full initialization procedure if sufficient transfer efficiency is achieved. We will now show that the method can also be extended to the symmetric bus architecture, where a bus ion is not necessarily member of a valid instance. In this case we must, after applying the unitary removal of uncoupled ions to all channels, examine whether a bus qubit is coupled to representatives of all channels. This can be achieved by applying the gate sequence

$$(10.2)$$

between the bus and all outer qubits, starting with the bus in  $|1\rangle_{\text{bus}}$  and the outer qubits in  $|0\rangle_i$ . The quantum circuit notation has been stretched somewhat in the above diagram, as the target ion might not be present: both the CNOT and CPHASE gates should be implemented so that they do nothing if no population is present in the target qubit. In this case we see that each application of the circuit performs the following state mapping:

Initial bus state:	$ 0\rangle$	$ 0\rangle$	$ 1\rangle$	$ 1\rangle$
Target qubit present:	no	yes	no	yes
Final bus state:	$ 0\rangle$	$ 0\rangle$	$ 0\rangle$	$ 1\rangle$

so that after applying the sequence to all outer qubits, the bus will be in the  $|1\rangle$ -state iff all outer qubits were present. By transferring bus ions in  $|0\rangle_{\text{bus}}$  to  $|\text{aux}\rangle_{\text{bus}}$  the system has consequently been unitarily initialized<sup>1</sup>. With respect to implementability, it should be noted that the two controlled operations are both type B. The CNOT-gate could be implemented as a conditioned  $\hat{x}_\pi$  rotation, while the controlled phase could be implemented by two consecutive conditioned  $\hat{x}_\pi$  rotations.

### 10.3 Long Qubit Decoherence Time

Provided that a sufficiently high threshold coupling strength  $g_{\text{min}}$  is used so that the REQC system is within the independent instance regime, as described in section 8.4.1, the qubit decoherence time is the ground state hyperfine decoherence time of the individual ions. As mentioned in section 3.2.2, such decoherence times of up to 82 ms have been observed for rare-earth-ion doped crystals. Compared to an optical field Rabi frequency  $\Omega_0$ , and more importantly the maximal channel hole width  $\Delta^{(\text{hole})}$  of approximately 5 MHz, this corresponds to 5 orders of magnitude between the qubit decoherence time and the typical gate time.

**Inhomogeneous broadening of ground state hyperfine levels.** If no compensating field is applied the hyperfine levels will experience inhomogeneous broadening, typically on the order of tens of kHz. The ill effects of this are easily countered by regularly swapping the qubit levels. An example of how such a swap can conveniently be integrated in gate operations is provided by the seven pulse gate sequence (8.11), which swaps the population of the qubit levels of the controlling ion.

**Loss of ions.** The reason for requiring the qubit decoherence time to be much larger than the gate time is to ensure that error correction can be used to recover all errors. This does not, however, take into account the fact that REQC qubits can decay to their  $|\text{aux}\rangle$  state, thus becoming inaccessible to error correction. The loss of qubits will impose a limit on the length of algorithms that can be implemented.

This problem can partly be addressed in the asymmetric bus architecture by using the bus qubit for decay-prone operations: since all members of the bus channel are part of a valid instance, they can safely be “recycled”.

### 10.4 Universal Gates

**One qubit gates.** As we have seen in chapter 5, implementing a universal set of one qubit gates seems entirely feasible. Also, coherent manipulation of spec-

<sup>1</sup> This result is very recent and has not yet been published.

tral structures similar to channels have been demonstrated experimentally [42]. Nevertheless, it is clear that implementing coherent modulation of optical fields with arbitrary waveforms is not trivial, and it has been discussed if the nonlinearities of the modulator system should be included directly in the model used by the optimization software. From a larger perspective, it seems entirely reasonable to assume that techniques for coherently manipulating optical fields will not be a limiting factor, given the advances in such techniques over recent years.

**Two-qubit gates.** With respect to two-qubit gates, we must as already noted require interaction strengths above 10 MHz in order to obtain gate error rates below  $10^{-4}$  for the example system. While the dipole blockade gates are able to operate for all coupling values above this threshold, the comb-gate in its present form would, as shown in section 8.2, only be able to use on the order of 1% of these at a fidelity of  $1 - 10^{-4}$ , making the choice of dipole blockade gates obvious.

In the case of the example system, it is critical that the minimal threshold coupling strength of  $g_{\min} = 10$  MHz, coincides with the maximal hole width  $\Delta^{(\text{hole})}$  achievable, even before any room for imperfection is included. Since it does not make sense to extend  $g_{\min}$  above  $\Delta^{(\text{hole})}$ , it seems that we must conclude that the limiting factor with respect to high fidelity two-qubit gates in the  $\text{Eu}^{3+}:\text{YAlO}_3$  system is the ratio  $\Gamma_e/\Delta^{(\text{hole})}$ , which we must require to be somewhat lower than the desired gate error rate.

With respect to the performance of the two-gates described in chapter 8, it should be noted that the bound (8.28) on entangling power was not derived until very recently and has consequently not been available as a guideline for choice of optimization parameters: The fact that we have not quite reached the theoretical performance limits does not imply that this is infeasible.

It should also be noted that the asymmetrical form of the dipole blockade gates could potentially be a strength with respect to an implementation using a bus architecture. As an example, the prolonged excitation of the control ion might not be critical if the control ion was always the bus, and could be recycled in case of a decay.

## 10.5 Read Out

Qubit specific read out is available in the REQC system as an ensemble average of  $\langle \sigma_z \rangle$ , obtained e.g. through absorption spectroscopy or by addressing a cycling transition [45].

The accuracy with which the expectation value can be measured affects the performance of most quantum algorithms as discussed in section 4.4. Ultimately, the read-out accuracy is determined by the number of instances present, so that the question of read out is closely related to that of scaling.

# CHAPTER 11

## Summary and Outlook

In summary, we have established that the REQC proposal, which was in its original form not suited for error-corrected quantum computing, can be adapted to meet most of the requirements for scalable quantum computing as described by DiVincenzo [22]: The system can be effectively initialized, qubits with long coherence time have been demonstrated, robust gate implementations are available for the system, and qubit readout has been demonstrated. In particular, there does no longer appear to be any fundamental obstacles to implementing small scale quantum computing in the system.

The initialization process, which as shown in chapter 10 can be performed unitarily for a bus-based REQC system, allows us to establish channels which in effect implement massively parallel quantum registers. By means of optical fields, the channels can be manipulated on time scales 4 orders of magnitude faster than the decoherence time of the channels, as has been experimentally demonstrated. We establish in chapter 5, that phase compensating pulses allow any one-qubit gate operation to be implemented robustly by means of population swapping operations applied in parallel to two optical transitions.

In chapters 6 and 7 we describe a numerical method for optimizing gate implementations by means of a sample-based estimate of the gate performance. This method has performed remarkably well, in particular with respect to reducing the duration of phase shift operations, thus reducing the associated exposure to decay. There are, however, several shortcomings which it would be interesting to address. Firstly, our results indicate that the sample-based estimate of gate performance is not well suited for ensuring that spectator ions are not disturbed. A prerequisite for addressing this problem seem to be a perturbational description of the evolution of spectator ions, which we propose to establish through the Magnus expansion. Based on this, we could either extend the optimization to include “area samples” describing the worst case performance for a range of parameter values, or alternatively adapt the parametrization to only allow fields that would not disturb spectator ions. Another aspect that could be worth considering in more detail is the optimization algorithm: the convergence goes through a transition from quadratic to linear at gate fidelities

that are barely good enough for scalable quantum computing. An understanding of the reason for this transition might allow us to push the transition to an acceptable fidelity, thus considerably reducing the numerical demands of the method. Finally, a better understanding of the evolution of spectator ions might make it possible to make do without an explicit field strength limit, which could potentially allow us to use direct optimization methods which have guaranteed quadratic convergence.

The method of phase compensating pulses can also be extended to two-qubit gates, and we establish in chapter 8 that this allows us to implement a powerful two-qubit gate robustly in terms of population swapping operations. As the naive phase-compensated dipole-blockade gate implementations require prolonged excitation of the control ion, we have applied the optimization method described above to obtain optimized replacements of short duration for the operations on the control ions. Although this has been successful, the results could most likely be improved by applying the optimization method directly to the full two-qubit problem. The challenge in performing such an optimization would be to obtain results which could be experimentally implemented, and perhaps even understood intuitively, allowing them to serve as inspiration for analytical gate design.

In relation to the construction of two-qubit gates, we have established a bound on the entangling power of any Hamiltonian. In the case of the REQC system, this results in a lower limit on the total population of the excited state during the gate operation. It would be interesting to consider the implications of the established bound for other proposed quantum information processing systems.

The scaling properties are the Achilles heel of the REQC proposal: due to the bound on the entangling power described above, we must require the multi-qubit gate operations to involve pairs of strongly coupled ions which are very rare. This problem could be remedied by the asymmetric bus architecture described in chapter 10, but no potential physical implementations of this have been proposed. We have loosely considered the differences between the independent instance model used exclusively in this thesis, and models involving some degree of entanglement within channels. It would be worthwhile to examine the properties of the later model, in order to establish if the coherence properties are as bleak as asserted here.

During our study of the statistics of the dipole coupling strength in chapter 9, we have predicted the Lorentzian probability distribution of the field at a center of a spherical distribution of parallel to be offset by on the order of 7% of the FWHM. We are currently working on extending this result to describe imperfect alignment of the dipoles. It would also be interesting to establish experimental conditions under which the shift could be explicitly observed.

# Bibliography

- [1] P. Benioff, *J. Stat. Phys.* **29**, 515 (1982).
- [2] R. P. Feynman, *Optics News* **11**, 11 (1985).
- [3] A. Peres, *Phys. Rev. A* **32**, 3266 (1985).
- [4] D. Deutsch, *Proc. R. Soc. Lond. A* **400**, 97 (1985).
- [5] P. W. Shor, in *Proceedings of the 35th Annual Symposium on Foundations of Computer Science* (IEEE Computer Society Press, 1994), p. 124.
- [6] L. K. Grover, *Phys. Rev. Lett.* **79** (1997).
- [7] A. M. Steane, *Phys. Rev. Lett.* **77**, 793 (1996).
- [8] A. R. Calderbank and P. W. Shor, *Phys. Rev. A* **54**, 1098 (1996).
- [9] Y. S. Weinstein, M. A. Pravia, E. M. Fortunato, S. Lloyd, and D. G. Cory, *Phys. Rev. Lett.* **86**, 1889 (2001).
- [10] L. M. K. Vandersypen, M. Steffen, G. Breyta, C. S. Yannoni, M. H. Sherwood, and I. L. Chuang, *Nature* **414**, 883 (2001).
- [11] Y. S. Weinstein, S. Lloyd, J. Emerson, and D. G. Cory, *Phys. Rev. Lett.* **89**, 157902 (2002).
- [12] M. A. Nielsen and I. L. Chuang, *Quantum Computation and Quantum Information* (Cambridge University Press, 2000).
- [13] J. Preskill, *Lecture notes on quantum information and computation* (1998), URL [www.theory.caltech.edu/~preskill](http://www.theory.caltech.edu/~preskill).
- [14] D. Deutsch, A. Barenco, and A. Ekert, *Proc. R. Soc. Lond. A* **449**, 669 (1995).
- [15] S. Lloyd, *Phys. Rev. Lett.* **75**, 346 (1995).
- [16] P. W. Shor, *SIAM J. Comput.* **26**, 1484 (1997).
- [17] R. Jozsa, *Quantum algorithms and the Fourier transform* (1997), [quant-ph/9707033](http://quant-ph/9707033).

- [18] P. W. Shor, Phys. Rev. A **52**, 2493 (1995).
- [19] W. H. Zurek, Physics Today **44**, 36 (1991).
- [20] W. H. Zurek, *Decoherence and the transition from quantum to classical – revisited* (2003), quant-ph/0306072.
- [21] R. Hughes, G. Doolen, et al., Tech. Rep. 2, Advanced Research and Development Activity (ARDA) (2004), URL <http://qist.lanl.gov/>.
- [22] D. P. DiVincenzo, Fortschritte der Physik **48**, 771 (2000).
- [23] L. F. Johnson, G. D. Boyd, and K. Nassau, Proc. IRE **50**, 86 (1962).
- [24] T. Kitagawa, K. Hattori, K. Shuto, M. Yasu, M. Kobayashi, and M. Horiguchi, Electron. Lett. **28**, 1818 (1992).
- [25] R. J. F. S. Lin and A. R. Mickelson, J. Appl. Phys **79**, 2868 (1996).
- [26] A. A. Kaplyanskii and R. M. MacFarlane, eds., *Spectroscopy of Solids Containing Rare Earth Ions* (North Holland, Amsterdam, 1987), chap. 3.
- [27] B. H. Bransden and C. J. Joachain, *Physics of atoms and molecules* (Addison Wesley Longman Limited, 1983), ISBN 0-582-44401-2.
- [28] A. J. Freeman and R. E. Watson, Phys. Rev. **127**, 2058 (1962).
- [29] M. Nilsson, L. Rippe, N. Ohlsson, T. Christiansson, and S. Kröll, Physica Scripta **T102**, 178 (2002).
- [30] G. H. Dieke and H. M. Crosswhite, Appl. Opt. **2**, 675 (1963).
- [31] J. J. Longdell, Ph.D. thesis, Australian National University (2003), URL <http://eprints.anu.edu.au/archive/00002321>.
- [32] E. Fraval, M. J. Sellars, and J. J. Longdell, *Method of extending hyperfine coherence times in  $Pr^{3+}:Y_2SiO_5$*  (2003), quant-ph/0306169.
- [33] B. S. Ham, M. S. Shahriar, M. K. Kim, and P. R. Hemmer, Phys. Rev. B **58**, R11825 (1998).
- [34] R. W. Equall, Y. Sun, R. L. Cone, and R. M. Macfarlane, Phys. Rev. Lett. **72**, 2179 (1998).
- [35] R. Yano, M. Mitsunaga, and N. Uesugi, Opt. Lett. **16**, 1884 (1991).
- [36] A. J. Meixner, C. M. Jefferson, and R. M. Macfarlane, Phys. Rev. B **46**, 5912 (1992).
- [37] Y. P. Wang and R. S. Meltzer, Phys. Rev. B **45**, 10119 (1992).

- [38] M. Boström, J. Longdell, D. Mitchell, and B. Ninham, *Eur. Phys. J. D* **22**, 47 (2003).
- [39] M. D. Lukin, M. Fleischhauer, R. Cote, L. M. Duan, D. Jaksch, J. I. Cirac, and P. Zoller, *Phys. Rev. Lett.* **87**, 037901 (2001).
- [40] N. Ohlsson, R. K. Mohan, and S. Kröll, *Opt. Comm.* **201**, 71 (2002).
- [41] G. J. Pryde, M. J. Sellars, and N. B. Manson, *Phys. Rev. Lett.* **84**, 1152 (2000).
- [42] J. J. Longdell and M. J. Sellars, *Phys. Rev. A* **69**, 032307 (2004).
- [43] J. Wesenberg and K. Mølmer, *Phys. Rev. A* **68**, 012320 (2003).
- [44] M. D. Lukin and P. R. Hemmer, *Phys. Rev. Lett.* **84**, 2818 (2000).
- [45] J. J. Longdell and M. J. Sellars, *Selecting ensembles for rare earth quantum computation* (2003), [quant-ph/0310105](https://arxiv.org/abs/quant-ph/0310105).
- [46] C. A. Sackett, D. Kielpinski, B. E. King, C. Langer, V. Meyer, C. J. Myatt, M. Rowe, Q. A. Turchette, W. M. Itano, D. J. Wineland, et al., *Nature* **404**, 256 (2000).
- [47] V. Meyer, M. A. Rowe, D. Kielpinski, C. A. Sackett, W. M. Itano, C. Monroe, and D. J. Wineland, *Phys. Rev. Lett.* **86**, 5870 (2001).
- [48] G. Brassard, P. Høyer, M. Mosca, and A. Tapp, in *Quantum Computation and Quantum Information: A Millennium Volume* (AMS, 2002), vol. 305 of *AMS Contemporary Mathematics Series*.
- [49] G. Brassard, P. Høyer, and A. Tapp, *Lecture Notes in Computer Science* **1443**, 820 (1998).
- [50] M. Boyer, G. Brassard, P. Høyer, and A. Tapp, *Fortschritte Der Physik* **46**, 493 (1998).
- [51] D. Collins, *Phys. Rev. A* **65**, 052321 (2002).
- [52] J. A. Jones and M. Mosca, *Phys. Rev. Lett.* **83**, 1050 (1999).
- [53] W. Dür, G. Vidal, and J. I. Cirac, *Phys. Rev. A* **62**, 062314 (2000).
- [54] J. J. Longdell, M. J. Sellars, and N. B. Manson, *Quantum phase gate between ions in a solid* (2004), [quant-ph/0404083](https://arxiv.org/abs/quant-ph/0404083).
- [55] J. J. Longdell, M. J. Sellars, and N. B. Manson, *Demonstration of conditional quantum phase shift between ions in a solid* (2004), [quant-ph/0404083](https://arxiv.org/abs/quant-ph/0404083).
- [56] R. P. Feynman, F. L. Vernon, and R. W. Hellwarth, *J. Appl. Phys.* **28**, 49 (1957).

- [57] H. K. Cummins, G. Llewellyn, and J. A. Jones, *Phys. Rev. A* **67**, 042308 (2003).
- [58] K. Brown, A. Harrow, and I. Chuang, *Arbitrarily accurate composite pulses* (2004), [quant-ph/0407022](https://arxiv.org/abs/quant-ph/0407022).
- [59] M. H. Levitt, *Prog. Nucl. Magn. Reson. Spectrosc.* **18**, 61 (1986).
- [60] R. Tycko and A. Pines, *Chem. Phys. Lett.* **111**, 462 (1984).
- [61] W. S. Warren, *Jour. Chem. Phys.* **81**, 5437 (1984).
- [62] M. S. Silver and R. I. Joseph, *Phys. Rev. A* **31**, 3753 (1985).
- [63] I. Roos and K. Mølmer, *Phys. Rev. A* **69**, 022321 (2004).
- [64] T. Blasberg and D. Suter, *Optics Commun.* **109**, 133 (1994).
- [65] M. V. Berry, *Proc. R. Soc. Lond. A* **392**, 45 (1984).
- [66] F. Wilczek and A. Zee, *Phys. Rev. Lett.* **52**, 2111 (1984).
- [67] Y. Aharonov and J. Anandan, *Phys. Rev. Lett.* **58**, 1593 (1987).
- [68] A. Shapere and F. Wilczek, *Geometric Phases in Physics* (World Scientific, Singapore, 1989).
- [69] J. A. Jones, V. Vedral, A. Ekert, and G. Castagnoli, *Nature* **403**, 869 (2000).
- [70] A. Nazir, T. P. Spiller, and W. J. Munro, *Phys. Rev. A* **65**, 042303 (2002).
- [71] F. Gaitan, *Noisy control, the adiabatic geometric phase, and destruction of the efficiency of geometric quantum computation* (2003), [quant-ph/0312008](https://arxiv.org/abs/quant-ph/0312008).
- [72] L. Rippe (2004), private communication.
- [73] A. P. Peirce, M. A. Dahleh, and H. Rabitz, *Phys. Rev. A* **37**, 4950 (1988).
- [74] H. Rabitz, R. de Vivie-Riedle, M. Motzkus, and K. Kompa, *Science* **288**, 824 (2000).
- [75] A. O. Niskanen, J. J. Vartiainen, and M. M. Salomaa, *Optimal multiqubit operations for Josephson charge qubits* (2003), [quant-ph/0302052](https://arxiv.org/abs/quant-ph/0302052).
- [76] A. L. Schwartz, Ph.D. thesis, University of California at Berkeley (1996), URL <http://www.accesscom.com/~adam/RIOTS/thesis.pdf>.
- [77] L. Cesari, *Optimization – theory and applications* (Springer Verlag, New York, 1983).
- [78] J. T. Betts, *Practical Methods for Optimal Control Using Nonlinear Programming* (Society for Industrial and Applied Mathematics (SIAM), 2001).

- [79] L. S. Jennings, M. E. Fisher, K. L. Teo, and C. J. Goh, *MISER3 Optimal Control Software* (2002), URL <http://www.cado.uwa.edu.au/miser/>.
- [80] K. L. Teo, C. J. Goh, and K. H. Wong, *A unified computational approach to optimal control problems* (Longman Scientific & Technical, 1991).
- [81] Y. Ohtsuki, W. Zhu, and H. Rabitz, *J. Chem. Phys.* **110**, 9825 (1999).
- [82] W. Zhu and H. Rabitz, *Jour. Chem. Phys.* **109**, 385 (1998).
- [83] W. Zhu and H. Rabitz, *Phys. Rev. A* **58**, 4741 (1998).
- [84] J. P. Palao and R. Kosloff, *Phys. Rev. Lett.* **89**, 188301 (2002).
- [85] D. J. Tannor, V. A. Kazakov, and V. Orlov, in *Time-Dependent Quantum Molecular Dynamics*, edited by J. Broeckhove and L. Lathouwers, NATO Advanced Study Institute (Plenum, New York, 1992), vol. 299 of *Series B: Physics*, pp. 347–360.
- [86] J. P. Palao and R. Kosloff, *Phys. Rev. A* **68**, 062308 (2003).
- [87] Y. Maday and G. Turinici, *Jour. Chem. Phys.* **118**, 8191 (2003).
- [88] L. S. Pontryagin, V. G. Boltyanskii, R. V. Gamkrelidze, and E. F. Mishchenko, *The Mathematical Theory of Optimal Processes* (Interscience Publishers, New York, 1962).
- [89] L. C. Young, *Calculus of variations and optimal control theory* (W. B. Saunders Company, Philadelphia, 1969).
- [90] J. H. Wesenberg, *Phys. Rev. A* **69**, 042323 (2004).
- [91] A. E. Bryson and Y.-C. Ho, *Applied Optimal Control* (Blaisdell Publishing Company, 1969).
- [92] D. G. Luenberger, *Introduction to Dynamic Systems* (John Wiley & Sons, 1979), ISBN 0-471-02594-1.
- [93] R. Kosloff, *Annu. Rev. Phys. Chem.* **45**, 145 (1994).
- [94] C. Leforestier, R. H. Bisseling, C. Cerjan, M. D. Feit, R. Friesner, A. Guldberg, A. Hammerich, G. Jolicard, W. Karrlein, H. D. Meyer, et al., *J. Comp. Phys.* **94**, 59 (1991).
- [95] U. Peskin and N. Moiseyev, *J. Chem. Phys.* **99**, 4590 (1993).
- [96] R. Fletcher, *Practical Methods of Optimization* (John Wiley & Sons, 1987), 2nd ed.
- [97] P. E. Gill, W. Murray, and M. H. Wright, *Practical Optimization* (Academic Press, 1981).

- [98] D. G. Luenberger, *Linear and Nonlinear Programming* (Addison-Wesley Publishing Company, 1984), 2nd ed.
- [99] Optimization Technology Center Homepage, *Optimization technology center homepage*, URL <http://www.ece.northwestern.edu/OTC/>.
- [100] C.-J. Lin and J. J. Moré, *SIAM Journal on Optimization* **9**, 1100 (1999).
- [101] *Optimization Toolbox User's Guide*, The MathWorks, version 2.2 ed. (2002), URL [www.mathworks.com](http://www.mathworks.com).
- [102] C. Cohen-Tannoudji, J. Dupont-Roc, and G. Grynberg, *Atom-Photon Interactions* (John Wiley and Sons, 1992).
- [103] L. M. K. Vandersypen and I. L. Chuang, *NMR techniques for quantum control and computation* (2004), [quant-ph/0404064](http://arxiv.org/abs/quant-ph/0404064).
- [104] J. H. Wesenberg and K. Mølmer, *Phys. Rev. Lett.* **93**, 143903 (2004).
- [105] A. M. Stoneham, *Rev. Mod. Phys.* **41**, 82 (1969).
- [106] E. Barkai, R. Silbey, and G. Zumofen, *Phys. Rev. Lett.* **84**, 5339 (2000).
- [107] B. Fristedt and L. Gray, *A Modern Approach to Probability Theory* (Springer Verlag, 1996), ISBN 0817638075.
- [108] W. Feller, *An Introduction to Probability Theory and Its Applications*, vol. 2 (John Wiley and Sons, Inc., New York, 1966), 3rd ed.
- [109] H. C. Fogedby, *Levy flights in quenched random force fields* (1998), [cond-mat/9801211](http://arxiv.org/abs/cond-mat/9801211).
- [110] N. W. Ashcroft and N. D. Mermin, *Solid state physics* (Saunders College Publishing, 1976).
- [111] W. Paul and J. Baschnagel, *Stochastic processes: from physics to finance* (Springer-Verlag, Berlin, 1999).
- [112] C. Kittel and E. Abrahams, *Phys. Rev.* **90**, 238 (1953).
- [113] M. Persson, Master's thesis, Lunds Tekniska Högskola (2001).
- [114] Y. Sun, G. M. Wang, R. L. Cone, R. W. Equall, and M. J. M. Leask, *Phys. Rev. B* **62**, 15443 (2000).
- [115] M. Nilsson, L. Rippe, J. Wesenberg, K. Mølmer, and S. Kröll, work in progress.
- [116] J. J. Garcia-Ripoll and J. I. Cirac, *Phys. Rev. Lett.* **90**, 127902 (2003), [quant-ph/0208143](http://arxiv.org/abs/quant-ph/0208143).
- [117] L. Rippe et al. (2004), Presentation at ESQUIRE meeting.